

Galactic transient sources with the Cherenkov Telescope Array

- K. Abe¹ S. Abe² J. Abhir³ A. Abhishek⁴ F. Acero^{5,6} A. Acharyya⁷ R. Adam^{8,9} A. Aguasca-Cabot¹⁰ I. Agudo¹¹ A. Aguirre-Santaella¹² J. Alfaro¹³ R. Alfaro¹⁴
N. Alvarez-Crespo¹⁵ R. Alves Batista¹⁶ J.-P. Amans¹⁷ E. Amato¹⁸ G. Ambrosi¹⁹ F. Ambrosino²⁰ E. O. Angüner²¹ L. A. Antonelli²⁰ C. Aramo²² C. Arcaro²³
T. T. H. Arnesen²⁴ K. Asano² Y. Ascasibar¹⁶ J. Aschersleben²⁵ H. Ashkar⁹ L. Augusto Stuaní²⁶ D. Baack²⁷ M. Backes^{28,29} C. Balazs³⁰ M. Balbo³¹
A. Baquero Larriva^{15,32} V. Barbosa Martins³³ U. Barres de Almeida^{34,35} J. A. Barrio¹⁵ L. Barrios-Jiménez²⁴ I. Batković³⁶ R. Batzofin³⁷ J. Baxter²
J. Becerra González²⁴ J. Becker Tjus³⁸ R. Belmont³⁹ W. Benbow⁴⁰ J. Bernete⁴¹ K. Bernlöhr⁴² A. Berti⁴³ B. Bertucci¹⁹ V. Beshley⁴⁴ P. Bhattacharjee⁴⁵
S. Bhattacharyya⁴⁶ C. Bigongiari²⁰ E. Bissaldi^{47,48} O. Blanch⁴⁹ J. Blazek⁵⁰ F. Bocchino⁵¹ C. Boisson¹⁷ J. Bolmont⁵² G. Bonnoli^{53,54} A. Bonollo^{55,56}
P. Bordas¹⁰ Z. Bosnjak⁵⁷ E. Bottacini³⁶ M. Böttcher²⁹ F. Bradascio⁵⁸ E. Bronzini⁵⁹ A. M. Brown⁶⁰ G. Brunelli⁵⁹ A. Bulgarelli⁵⁹ I. Burelli⁶¹
C. Burger-Scheidlin⁶² L. Burmistrov³¹ M. Burton^{63,64} M. Buscemi⁶⁵ J. Cailleux¹⁷ A. Campoy-Ordaz⁶⁶ B. K. Cantlay^{67,68} G. Capasso⁶⁹ A. Caproni⁷⁰
R. Capuzzo-Dolcetta^{20,71} P. Caraveo⁷² S. Caroff⁴⁵ A. Carosi²⁰ R. Carosi⁵⁴ E. Carquin⁷³ M.-S. Carrasco⁷⁴ E. Cascone⁶⁹ F. Cassol⁷⁴ L. Castaldini⁵⁹
N. Castrejon⁷⁵ A. J. Castro-Tirado¹¹ D. Cerasole⁷⁶ G. Ceribella⁴³ M. Cerruti⁷⁷ P. M. Chadwick⁶⁰ S. Chaty⁷⁷ A. W. Chen⁷⁸ M. Chernyakova⁷⁹
A. Chiavassa^{80,81} J. Chudoba⁵⁰ L. Chytka⁵⁰ G. M. Ciccari⁸⁰ A. Cifuentes⁴¹ C. H. Coimbra Araujo⁸³ M. Colapietro⁶⁹ V. Conforti⁵⁹ J. L. Contreras¹⁵
J. Cortina⁴¹ A. Costa⁸⁴ H. Costantini⁷⁴ G. Cotter⁸⁵ P. Cristofari¹⁷ O. Cuevas⁸⁶ Z. Curtis-Ginsberg⁸⁷ A. D'Ai⁸⁸ G. D'Amico⁸⁹ F. D'Ammando⁹⁰ S. Dai⁹¹
F. Dazzi⁹² M. de Bony de Lavergne⁵ V. De Caprio⁶⁹ G. De Cesare⁵⁹ F. De Frondat Laadim¹⁷ E. M. de Gouveia Dal Pino³⁵ B. De Lotto⁶¹ M. De Lucia²²
D. de Martino⁶⁹ R. de Menezes^{80,81} M. de Naurois⁹ E. de Ona Wilhelmi³³ V. de Souza²⁶ L. del Peral⁷⁵ M. V. del Valle³⁵ C. Delgado⁴¹ M. Dell'aiera⁴⁵
M. Della Valle^{69,22} D. della Volpe³¹ D. Depaoli⁴² J. Devin⁹³ T. Di Girolamo^{94,22} A. Di Piano^{59,95} F. Di Pierro⁸⁰ R. Di Tria⁷⁶ L. Di Venere⁴⁸ S. Diebold⁹⁶
R. Dima³⁶ A. Dinesh¹⁵ J. Djuvsland⁸⁹ R. M. Dominik²⁷ D. Dominis Prester⁹⁷ A. Donini²⁰ D. Dorner^{98,3} J. Dörner³⁸ M. Doro³⁶ C. Dubos⁹⁹ L. Ducci⁹⁶
V. V. Dwarkadas¹⁰⁰ J. Ebr⁵⁰ C. Eckner^{46,101} K. Egberts³⁷ S. Einecke¹⁰² D. Elsässer²⁷ G. Emery⁷⁴ M. Errando¹⁰³ C. Escanuela⁴² P. Escarate¹⁰⁴
M. Escobar Godoy¹⁰⁵ J. Escudero Pedrosa¹¹ P. Esposito^{35,72} D. Falceta-Goncalves¹⁰⁶ S. Fegan⁹ Q. Feng¹⁰⁷ G. Ferrand^{108,109} F. Ferrarotto¹¹⁰ E. Fiandrini¹⁹
A. Fiasson⁴⁵ M. Filipovic⁹¹ V. Fioretti⁵⁹ M. Fiori¹¹¹ H. Flores¹⁷ L. Foffano¹¹² L. Font Guiteras⁶⁶ G. Fontaine⁹ A. Franckowiak¹¹³ S. Fröse²⁷ Y. Fukazawa¹¹⁴
Y. Fukui¹¹⁵ S. Funk¹¹⁶ A. Furniss¹⁰⁵ G. Galanti⁷² G. Galaz¹³ C. Galelli¹⁷ Y. A. Gallant⁹³ S. Gallozzi²⁰ V. Gammaldi^{117,16} M. Garczarczyk³³ C. Gasbarra¹¹⁸
D. Gasparri¹¹⁸ M. Gaug⁶⁶ A. Ghalumyan¹¹⁹ F. Gianotti⁵⁹ M. Giarrusso⁶⁵ J. G. Giesbrecht Formiga Paiva³⁴ N. Giglietto^{47,48} F. Giordano⁷⁶ M. Giroletti⁹⁰
R. Giuffrida⁵¹ A. Giuliani⁷² J.-F. Glicenstein⁵⁸ J. Glombitza¹¹⁶ P. Goldoni¹²⁰ J. M. González¹²¹ M. M. González¹⁴ J. Goulart Coelho¹²² T. Gradetzke²⁷
J. Granot^{123,124} R. Grau¹⁴ L. Gréaux⁹⁹ D. Green⁴³ J. G. Green⁴³ T. Greenshaw¹²⁵ I. Grenier³⁹ G. Grolleron⁵² J. Grube¹²⁶ O. Gueta¹²⁷ J. Hackfeld^{38,27}
D. Hadasch² P. Hamal⁵⁰ W. Hanlon⁴⁰ S. Hara¹²⁸ V. M. Harvey¹⁰² T. Hassan⁴¹ K. Hayashi^{129,2} B. Heß⁹⁶ L. Heckmann^{43,130} M. Heller³¹ J. Hinton⁴²
N. Hiroshima^{2,131} B. Hnatyk¹³² R. Hnatyk¹³² W. Hofmann⁴² D. Horan⁹ P. Horvath¹³³ T. Hovatta^{134,135} M. Hrabovsky¹³³ D. Hrupec¹³⁶ M. Iarlori¹³⁷
T. Inada² F. Incardona⁸⁴ S. Inoue^{138,2} Y. Inoue^{139,109} F. Iocco^{94,22} A. Iuliano²² M. Jamroz¹⁴⁰ P. Janecek⁵⁰ F. Jankowsky¹⁴¹ P. Jean¹⁴² I. Jiménez Martínez⁴³
J. Jimenez Quiles⁴⁹ W. Jin¹⁴³ C. Juramy-Gilles⁵² J. Jurysk⁵⁰ O. Kalekin¹¹⁶ D. Kantzas¹⁰¹ V. Karas¹⁴⁴ H. Katagiri¹⁴⁵ J. Kataoka¹⁴⁶ S. Kaufmann⁶⁰
D. Kerszberg⁴⁹ B. Khélifi⁷⁷ D. B. Kieda¹⁰⁷ R. Kissmann¹³⁰ T. Kleiner³³ G. Kluge¹⁴⁷ W. Kluźniak¹⁴⁸ Y. Kobayashi^{138,2} K. Kohri^{149,150} N. Komin⁷⁸ A. Kong²
P. Korneic¹⁷ K. Kosack⁵ D. Kostunin³³ G. Kowal¹⁰⁶ H. Kubo² J. Kushida¹ A. La Barbera⁸⁸ N. La Palombara⁷² M. Láinez¹⁵ A. Lamastra²⁰ J. Lapington¹⁵¹
S. Lazarević⁹¹ J. Lazentic-Galloway³⁰ M. Lemoine-Goumard¹⁵² J.-P. Lenain⁵² F. Leone¹⁵³ E. Leonora⁶⁵ G. Leto⁸⁴ E. Lindfors¹⁵⁴ I. Liodakis¹³⁴ S. Lloyd⁶⁰
S. Lombardi^{20,155} F. Longo¹⁵⁶ R. López-Coto¹¹ M. López-Moya¹⁵ A. López-Oramas^{24*} S. Loporchio^{47,48} J. Lozano Bahilo⁷⁵ F. Lucarelli²⁰
P. L. Luque-Escamilla¹⁵⁷ E. Lyard¹⁵⁸ O. Macias¹⁵⁹ J. Mackey⁶² G. Maier³³ P. Majumdar¹⁶⁰ M. Makariev¹⁶¹ M. Mallamaci^{82,65} D. Mandat⁵⁰
M. Manganaro⁹⁷ G. Manicò^{65,153} P. Marinos¹⁶² M. Mariotti³⁶ S. Markoff¹⁵⁹ I. Márquez¹¹ P. Marquez⁴⁹ G. Marsella^{82,65} G. A. Martínez⁴¹ M. Martínez⁴⁹
O. Martínez^{163,164} C. Marty¹⁴² A. Mas-Aguilar¹⁵ M. Mastropietro²⁰ G. Maurin⁴⁵ D. Mazin^{2,43} S. McKeague⁷⁹ D. Melkumyan³³ S. Menchiari^{11,18}
S. Mereghetti⁷² E. Mestre¹⁶⁵ J.-L. Meunier⁵² D. M.-A. Meyer¹⁶⁵ D. Miceli²³ M. Miceli^{82,51} M. Michailidis⁹⁶ J. Michalowski¹⁶⁶ T. Miener³¹
J. M. Miranda^{163,167} A. Mitchell¹¹⁶ M. Mizote¹⁶⁸ T. Mizuno¹⁶⁹ R. Moderski¹⁴⁸ L. Mohrmann⁴² M. Molero²⁴ C. Molfese⁹² E. Molina²⁴ T. Montaruli³¹
A. Moralejo⁴⁹ D. Morcuende¹¹ K. Morik^{27,170} A. Morselli¹¹⁸ E. Moulins⁵⁸ V. Moya Zamanillo¹⁵ K. Munari⁸⁴ T. Murach³³ A. Muraczewski¹⁴⁸ H. Muraiishi¹⁷¹
S. Nagataki¹⁰⁹ T. Nakamori¹⁷² L. Nava⁵³ A. Nayak⁶⁰ R. Nemmen^{35,162} J. P. Neto^{173,174} L. Nickel²⁷ J. Niemiec¹⁶⁶ D. Nieto¹⁵ M. Nieves Rosillo²⁴
M. Nikolajuk¹⁷⁵ L. Nikolić⁴ K. Nishijima¹ K. Noda^{138,2} D. Nosek¹⁷⁶ V. Novotny¹⁷⁶ S. Nozak⁴³ M. Ohishi² Y. Ohtani² A. Okumura^{177,178} J.-F. Olive¹⁴²
R. A. Ong¹⁴³ R. Orito¹⁷⁹ M. Orlandini⁵⁹ E. Orlando¹⁵⁶ S. Orlando⁵¹ M. Ostrowski¹⁴⁰ J. Otero-Santos¹¹ I. Oya¹⁸⁰ I. Pagano⁸⁴ A. Pagliaro⁸⁸ M. Palatiello²⁰
G. Panebianco⁵⁹ D. Paneque⁴³ F. R. Pantaleo^{48,47} A. Papitto²⁰ J. M. Paredes¹⁰ N. Parmiggiani⁵⁹ B. Patricelli^{20,181} A. Pe'er⁴³ M. Pech⁵⁰ M. Pecimotika¹⁸⁵ M. Pihet²³
U. Pensac^{52,17} M. Peresano⁴³ J. Pérez-Romero⁴⁶ M. Persic^{111,183} P.-O. Petrucci¹⁸⁴ O. Petruk^{44,51} G. Piano¹¹² E. Pierre⁵² E. Pietropaolo¹⁸⁵ M. Pihet²³
F. Pintore⁸⁸ G. Pirola⁴³ C. Pittori²⁰ C. Plard⁴⁵ F. Podobnik⁴ M. Pohl^{37,33} V. Pollet⁴⁵ G. Ponti⁵³ E. Prandini³⁶ G. Principe¹⁵⁶ C. Priyadarshi⁴⁹ N. Produit¹⁵⁸
M. Prouza⁵⁰ G. Pühlhofer⁹⁶ M. L. Pumo^{153,65} M. Punch⁷⁷ A. Quirrenbach¹⁴¹ S. Rainò⁷⁶ R. Rando³⁶ S. Razaque^{186,124} S. Recchia⁵³ M. Regeard⁷⁷
P. Reichherzer^{85,38} A. Reimer¹³⁰ O. Reimer¹³⁰ I. Reis^{26,58} A. Reisenegger^{13,187} T. Reposeur¹⁵² W. Rhode²⁷ D. Ribeiro¹⁸⁸ M. Ribó¹⁰ C. Ricci¹⁸⁹
T. Richtler¹⁹⁰ J. Rico⁴⁹ F. Rieger⁴² M. Rigoselli⁷² L. Riitano⁸⁷ V. Rizzi¹⁸⁵ E. Roache⁴⁰ L. S. Rocha¹⁹¹ G. Rodríguez Fernández¹¹⁸ M. D. Rodríguez Frías⁷⁵
J. Rodríguez⁵ J. J. Rodríguez-Vázquez⁴¹ P. Romano⁵³ G. Romeo⁸⁴ J. Rosado¹⁵ A. Rosales de Leon⁵² G. Rowell¹⁰² B. Rudak¹⁴⁸ A. J. Ruiter¹⁹² C. B. Rulten⁶⁰
I. Sadeh³³ L. Saha⁴⁰ T. Saito² H. Salzmann⁹⁶ M. Sánchez-Conde¹⁶ P. Sangiorgi⁸⁸ H. Sano^{193,2} R. Santos-Lima³⁵ V. Sapienza^{51,82} T. Šarić¹⁹⁴ A. Sarkar³³
S. Sarkar⁸⁵ F. G. Saturni²⁰ S. Savarese⁹² A. Scherer¹⁹⁵ F. Schiavone⁷⁶ P. Schipani⁶⁹ B. Schleicher^{98,3} P. Schovaneck⁵⁰ J. L. Schubert²⁷ F. Schussler⁵⁸
M. Seglar Arroyo⁴⁹ I. R. Seitzzahl¹⁹² O. Sergijenko^{132,196,197} M. Servillat¹⁷ V. Sguera⁵⁹ L. Sidoli⁷² H. Siejkowski¹⁹⁸ V. Sliusar¹⁵⁸ A. Slowikowska¹⁹⁹
H. Sol¹⁷ S. T. Spencer^{116,85} D. Spiga⁵³ A. Spolon¹¹¹ A. Stamerra^{20,127} S. Stanić⁴⁶ T. Starecki²⁰⁰ R. Starling¹⁵¹ Ł. Stawarz¹⁴⁰ S. Steinmassl⁴² C. Steppa³⁷
T. Stolarczyk⁵ J. Striško¹³⁶ Y. Suda¹¹⁴ T. Suomijärvi⁹⁹ D. Tak³³ M. Takahashi¹⁷⁷ R. Takeishi² S. J. Tanaka²⁰¹ F. Tavecchio⁵³ T. Tavernier⁵⁰ A. Taylor³³
L. A. Tejedor¹⁵ K. Terauchi²⁰² R. Terrier⁷⁷ M. Teshima⁴³ V. Testa²⁰ W. W. Tian² L. Tibaldo¹⁴² O. Tibolla⁶⁰ F. Tombesi^{118,20} D. Tonev¹⁶¹ D. F. Torres¹⁶⁵
G. Tosti^{53,19} N. Tothill⁹¹ F. Toussenel⁵² G. Tovmassian^{14,53} A. Tramacere¹⁵⁸ P. Travnicek⁵⁰ A. Trois²⁰³ S. Truzzi⁴ A. Tutone⁸⁸ L. Vaclavek^{133,50}
M. Vacula^{133,50} P. Vallania^{80,204} C. van Eldik¹¹⁶ J. van Scherpenberg⁴³ J. Vandenbroucke⁸⁷ V. Vassiliev¹⁴³ M. Vázquez Acosta²⁴ M. Vecchi²⁵ S. Ventura⁵⁴
S. Vercellone⁵³ G. Verma⁴ I. Viale³⁶ A. Viana²⁶ N. Viaux²⁰⁵ A. Vigliano⁶¹ J. Vignatti²⁰⁵ C. F. Vigorito^{80,81} J. Villanueva⁸⁶ E. Visentin^{80,81} S. Vitale¹¹⁸
V. Voisin⁵² V. Voitsekховskiy³¹ S. Vorobiov⁴⁶ G. Voutsinas³¹ I. Vovk² T. Vuillaume⁴⁵ S. J. Wagner¹⁴¹ R. Walter¹⁵⁸ M. Wechakama^{67,68} M. White¹⁰²
A. Wiercholska¹⁶⁶ M. Will⁴³ F. Wohlleben⁴² T. Yamamoto¹⁶⁸ R. Yamazaki²⁰¹ L. Yang^{186,206} T. Yoshikoshi² M. Zacharias^{141,29} G. Zaharijas⁴⁶
L. Zampieri¹¹¹ D. Zavrtanik⁴⁶ M. Zavrtanik⁴⁶ A. A. Zdziarski¹⁴⁸ W. Zhang¹⁶⁵ V. I. Zhdanov¹³² K. Zięta¹⁴⁰ M. Živec⁴⁶ J. Zuriaga-Puig¹⁶

Affiliations can be found at the end of the article

ABSTRACT

A wide variety of Galactic sources show transient emission at soft and hard X-ray energies: low-mass and high-mass X-ray binaries containing compact objects (e.g., novae, microquasars, transitional millisecond pulsars, supergiant fast X-ray transients), isolated neutron stars exhibiting extreme variability as magnetars as well as pulsar wind nebulae. Although most of them can show emission up to MeV and/or GeV energies, many have not yet been detected in the TeV domain by Imaging Atmospheric Cherenkov Telescopes. In this paper, we explore the feasibility of detecting new Galactic transients with the Cherenkov Telescope Array (CTA) and the prospects for studying them with Target of Opportunity observations. We show that CTA will likely detect new sources in the TeV regime, such as the massive microquasars in the Cygnus region, low-mass X-ray binaries with low-viewing angle, flaring emission from the Crab pulsar-wind nebula or other novae explosions, among others. We also discuss the multi-wavelength synergies with other instruments and large astronomical facilities.

Key words: gamma-rays:general – transients – binaries: general – pulsars:general – stars:novae – stars:magnetars

1 INTRODUCTION

Timing astronomy and variability studies have proven to be a powerful tool to study extreme astrophysical processes at very high energies (VHE, $E > 100$ GeV). The improvement of the Imaging Atmospheric Cherenkov Technique (IACT) over the past decade has revealed new transient phenomena with variability timescales from seconds to several weeks. The last generation of IACTs have discovered several classes of transient TeV sources such as gamma-ray bursts (GRBs) (MAGIC Collaboration et al. 2019; Abdalla et al. 2019), flaring blazars associated with high-energy neutrino sources (IceCube Collaboration et al. 2018) or Galactic novae (H. E. S. S. Collaboration et al. 2022; Acciari et al. 2022), among others, unveiling new types of VHE emitters with highly variable fluxes.

The Cherenkov Telescope Array (CTA) will be the next generation ground-based observatory for VHE astronomy. It will allow the detection of gamma rays in the 20 GeV–300 TeV domain, with two observatory sites, one in the Northern hemisphere (CTA-N; Observatorio Roque de los Muchachos, La Palma, Spain) and another in the Southern one (CTA-S; Paranal, Chile). It will provide an improved sensitivity with respect to the current generation of IACTs of about an order of magnitude (Cherenkov Telescope Array Consortium et al. 2019). Of special importance will be the sensitivity of CTA to short-timescale phenomena¹. CTA will have 10^4 – 10^5 better sensitivity than the LAT instrument onboard the *Fermi* satellite for the detection of short-duration transient events (Funk et al. 2013).

The low energy threshold of ~ 20 GeV of the largest telescopes of the array, the Large-Sized Telescopes (LSTs; CTA-LST Project et al. 2023) is key for the detection of new transient sources at the lower end of the VHE regime. This capability, together with the fast slewing response of the LSTs, which can be re-pointed in about 20 seconds, will allow a swift reaction to transient events. The Medium and Small Sized telescopes (MSTs and SSTs) will also be key to understand the emission of this sources at higher energies. Finally, since the CTA observatory will consist of two arrays located in two hemispheres, it will provide a better and more continuous coverage of many transient events accessible from both sites.

The core program of CTA will consist of different *Key Science Projects* (KSPs) which were considered to address the science questions of CTA (see Cherenkov Telescope Array Consortium et al. 2019 for more details). The *Transients* KSP is proposed to encompass the

follow-up observations of several classes of targets such as GRBs, gravitational waves (GWs), high-energy neutrinos, core-collapse supernovae (CCSNe) and Galactic transients.

In this paper, we focus on Galactic sources hosting compact objects whose emission is not periodic and/or that display unexpected flaring events, outflows or jets as described in Cherenkov Telescope Array Consortium et al. (2019). Extragalactic transient events such as GRBs, core-collapse SNe or GWs will be addressed in separate publications. We discuss the capabilities of CTA to detect new transient phenomena at VHE from sources of Galactic origin, ranging from microquasars, to pulsar-wind nebulae (PWNe) flares, to novae, transitional millisecond pulsars or magnetars among others. For our simulations, we have used the software packages `ctools`² (Knödlseder et al. 2016) and `Gammapy`³ (Donath et al. 2023; Aguasca-Cabot et al. 2023) with the official CTA observatory instrument response functions (IRFs).⁴ For a full description of CTA observatory IRFs and configurations see Maier et al. (2023).

The sources of our interest are described in the following Subsections 1.1–1.6. We present the sensitivity of CTA to Galactic transient detection in Section 2 and population studies in Section 3. The simulations, analysis results and discussion for each type of transient are collected in Section 4. Section 5 describes the synergies with multi-wavelength and multi-messenger astronomical facilities. The summary and final conclusions are listed in Section 6.

1.1 Microquasars

Microquasars are binary systems with a compact object (NS or a BH) orbiting around and accreting material from a companion star. The matter lost from the star can lead to formation of an accretion disk around the compact object and a relativistic collimated jet (Mirabel & Rodríguez 1998).

At the moment more than 20 microquasars are known in the Galaxy (see i.e. Corral-Santana et al. 2016). Observations demonstrated correlations between the mass of the compact object, radio (5 GHz) and

² `ctools` is a software specifically developed for the scientific analysis of gamma-ray data, see <http://cta.irap.omp.eu/ctools/index.html>

³ `Gammapy` is an open-source Python package developed for gamma-ray astronomy, see <https://gammapy.org/>

⁴ The IRF version `prod3b-v2` is the one used throughout the manuscript, unless otherwise specified. The newest `prod5` version corresponding to the *Alpha Configuration*, which corresponds to the first stage of CTA observatory construction has also been tested in some science cases and are specified in the text.

* aloramas@iac.es

¹ For CTA performance, see: <https://www.cta-observatory.org/science/ctao-performance/>

X-ray (2–10 keV) luminosities (e.g. [Falcke et al. 2004](#)), strengthening the link between active galactic nuclei (AGNs) and microquasars. In AGNs, jets are known to be places of efficient particle acceleration and produce broad band non-thermal emission. The resulting radiation can extend from radio up to the VHE band. According to TeVCat⁵ more than 65 AGNs have been already detected by current IACTs. If similar jet production and particle acceleration mechanisms operate in microquasars and AGNs, this might imply that microquasars should be sources of VHE γ -ray emission as well.

Up to now, only three microquasars have been detected in the high-energy (HE, $E > 100$ MeV) domain: Cygnus X-1 ([Bulgarelli et al. 2010](#); [Sabatini et al. 2010, 2013](#); [Malyshev et al. 2013](#); [Zanin et al. 2016](#); [Zdziarski et al. 2017](#)), Cygnus X-3 ([Tavani et al. 2009](#); [Fermi LAT Collaboration et al. 2009](#); [Zdziarski et al. 2018](#)), and SS 433 ([Bordas et al. 2015](#); [Sun et al. 2019](#); [Rasul et al. 2019](#); [King et al. 2019](#); [Li et al. 2020](#)). Steady VHE emission was detected from the interaction regions between the jet and the surrounding nebula in SS 433 ([Abeysekara et al. 2018a](#); [H. E. S. S. Collaboration et al. 2024](#)). Furthermore, HAWC has announced the TeV detection of the microblazar V4641 Sgr with 7 years of data ([Tibolla 2023](#)). A strong hint of transient emission was found at VHE in Cygnus X-1 ([Albert et al. 2007](#)). Strong hints of HE emission were also found in the low-mass X-ray binary V404 Cyg during its 2015 outburst ([Loh et al. 2016](#); [Piano et al. 2017](#)). The expectations for the detection of both massive microquasars and low-mass X-ray binaries (LMXBs) with CTA are presented in Sections 4.1–4.2.

The relevance for studying gamma-ray binaries and microquasars has already been addressed by [Paredes et al. \(2013\)](#). In this paper, we do not focus on gamma-ray binaries displaying periodic orbital variability, but only on microquasars, to better investigate the potential VHE emission of this class of binaries for which only SS 433 has been confirmed as a VHE emitter. We discuss high-mass microquasars (Section 4.1) separately to low-mass X-ray binaries (Section 4.2).

1.2 Transitional millisecond pulsars

Transitional millisecond pulsars (tMSPs) are a class of neutron star binaries that has emerged in the last decade with the discoveries of three confirmed systems: PSR J1023+0038 ([Archibald et al. 2009a](#); [Patruno et al. 2014a](#)), XSS J1227-4853 ([de Martino et al. 2010](#); [Bassa et al. 2014](#)) and IGR J1824-2452 in the globular cluster M28 ([Papitto et al. 2013](#)). Additionally, a handful of candidate tMSPs have been recently discovered in the X-ray and GeV ranges (see review by [Papitto & de Martino 2022](#)). tMSPs alternate between a radio-loud MSP state (RMSP, showing radio pulsations and no sign of an accretion disk) and a sub-luminous LMXB state (forming an accretion disk and showing X-ray pulsations). These sources are the direct link between the LMXB and the radio MSP phases in which neutron stars are spun up to ms periods during the LMXB-phase. Sudden transitions between the two states occur on a timescale of a few days to weeks, and are accompanied by drastic changes across the electromagnetic spectrum. The transition from the RMSP to LMXB state is accompanied by brightening of optical, UV ([Patruno et al. 2014b](#); [Takata et al. 2014](#)), X-ray and gamma-ray ([Stappers et al. 2013](#)) emission with the disappearance of radio pulsations. The origin of these transitions is still debated and, for this, intense multi-wavelength campaigns are on-going to understand the phenomenology in both the RMSP and LMXB states. tMSPs were so far not detected in the VHE regime.

The upper limits (ULs) in the VHE regime from tMSPs are discussed in Section 4.3.

1.3 Pulsar wind nebulae

Pulsar wind nebulae (PWNe) are bubbles or diffuse structures of relativistic plasma powered by a central highly-magnetized rotating neutron star (pulsar). PWNe show three different evolution stages (see e.g. [Olmi 2023](#) and references therein): a free-free expansion stage, in which there is no interaction with the surrounding supernova remnant (SNR); a reverberation phase in which the supernova reverse shock interacts with the PWN and a post-reverberation or bow shock stage, in which the pulsar leaves the SNR onto the external medium, creating a cometary-like structure. Some PWNe have been found to display TeV halos ([Abeysekara et al. 2017](#); [Cao et al. 2023a](#)), which are suggested to be the result of particle escape in evolved pulsar. Recently, several PWNe have been suggested to be PeV particle (leptons) accelerators, with the detection of gamma rays at $E > 100$ TeV ([Cao et al. 2021, 2023a](#)). The Crab nebula is the standard candle at VHE and both the nebula and the pulsar have been intensively studied. Pulsations have been measured up to TeV energies ([Ansoldi et al. 2016](#)) and the nebula spectrum has been detected up to 100 TeV by IACTs ([MAGIC Collaboration et al. 2020](#)) and recently extended to PeV ([Lhaaso Collaboration et al. 2021](#)). Unexpectedly, the Crab nebula displays rapid flaring emission over daily timescales at HE as reported by AGILE and *Fermi*-LAT ([Tavani et al. 2011](#); [Abdo et al. 2011](#)). The enhanced fluxes measured over different flaring episodes were a factor three-to-six times larger than the standard flux. So far, no signs of variability have been reported at VHE ([Mariotti 2010](#); [Ong 2010](#); [H. E. S. S. Collaboration et al. 2014](#); [van Scherpenberg et al. 2019](#)). The characterization of the expected VHE emission to be putatively detected by CTA is shown in Section 4.4.

1.4 Novae

Novae are thermonuclear runaway explosions on the surface of a white dwarf star in binary systems involving a white dwarf accreting matter, often through an accretion disc, usually from a late-type star ([Gallagher & Starrfield 1978](#)). They are detected as transient events exhibiting huge and sudden increase of brightness. Though novae have been studied both observationally and theoretically for many decades, a comprehensive understanding of nova physics is still lacking ([Iben 1982](#); [Yaron et al. 2005](#)). Particle acceleration in novae was predicted before the launch of the *Fermi* Gamma-ray space telescope (see [Tatischeff & Hernanz 2007](#)). Shortly after, GeV emission from the outburst of the symbiotic binary system V407 Cygni, comprised of a white dwarf and an evolved red giant companion, was first detected. Subsequently, classical novae with main sequence donor stars were also detected ([Abdo et al. 2010a](#); [Ackermann et al. 2014](#)).⁶ More recently, VHE emission in novae has been predicted and searched for in a handful of sources (see e.g. [Aliu et al. 2012](#); [Ahnén et al. 2015](#)), with the first detection at VHE gamma rays occurring in 2021 in the recurrent nova RS Ophiuchi (RS Oph, [Acciari et al. 2022](#); [H. E. S. S. Collaboration et al. 2022](#); [Abe et al. 2023](#)).

Since the first detection at HE gamma rays from nova Cygni 2010,

⁵ <http://tevcat2.uchicago.edu/>

⁶ [Gomez-Gomar et al. \(1998\)](#) (and references therein) predicted gamma-ray emission from novae but of nuclear origin, in the keV–MeV domain.

19 novae⁷ have been detected in this energy band (only RS Oph at VHE) with a rate of about one outburst detection per year. All novae so far detected at HE have been bright in the visible band (≤ 10 mag), and the vast majority are nearby sources with distances within 5 kpc (Franckowiak et al. 2018). Non-thermal emission is expected to arise from leptonic and hadronic interactions by particles accelerated in radiative expanding shocks (Abdo et al. 2010a; Hernanz & Tatischeff 2012), which can originate from the interaction of the ejecta during the initial stage of the outburst and the circumbinary material, or with the fast wind produced by nuclear burning in later stages of the outburst (Abdo et al. 2010a; Ackermann et al. 2014; Martin et al. 2018).

Based on observations of novae in the nearby M31 Galaxy, as well as binary population synthesis models for the Milky Way, a rate of approximately 30 nova events per year is expected (see Section 4.5). However, a significant proportion of these will be obscured by intervening dust in the Galactic plane. The number of nova events that will be detectable at HE and VHE gamma rays will be further constrained by properties of the system, such as the shock velocity and the target material density. This dependence on the parameter space and prospects for detection of novae at VHE will be characterised for CTA in Section 4.5.

1.5 Magnetars

Magnetars are isolated neutron stars in which the main energy source is the magnetic field (e.g. Mereghetti et al. 2015; Kaspi & Beloborodov 2017, for reviews). They are observed as pulsed X-ray sources, with typical spin periods of a few seconds and strong spin-down rates, and/or through the detection of short bursts and flares in the hard X-ray/soft gamma-ray range. This led to their historical subdivision in the Anomalous X-ray Pulsars and Soft Gamma-ray Repeater classes (Mereghetti 2008), but it is now clear that these are just two different manifestations of the same underlying object: a strongly magnetized neutron star powered by magnetic energy, as proposed by Paczynski (1992) and Duncan & Thompson (1992).

About 30 magnetars are known so far. With the exception of two sources in the Magellanic Clouds, all of them lie in the Galactic Plane. The majority of the magnetars are transient X-ray sources that have been discovered when they became active, with an increase of their X-ray luminosity (from a quiescent level of $\sim 10^{33}$ erg s⁻¹ up to $\sim 10^{36-37}$ erg s⁻¹), accompanied by the emission of luminous and rapid bursts. This means that the total Galactic population of magnetars is larger than the currently observed sample, and more sources of this class will be known at the time of CTA observations. Furthermore, magnetar-like behavior has recently been observed in some sources originally presumed to be of a different kind, such as rotation-powered (radio) pulsars (Gavriil et al. 2008; Göğüş et al. 2016), and even in the gamma-ray binary LS I +61 303 (Torres et al. 2012; Weng et al. 2022).

For what concerns the persistent emission, magnetars have not been detected above few hundred keV (Abdo et al. 2010b; Aleksić et al. 2013). Their X-ray emission typically comprises a soft thermal component that dominates in the 1-10 keV range and a hard power-law component that is believed to originate from multiple resonant scattering in the magnetosphere. The ULs in the MeV range (Li et al. 2017) indicate a turn-off of this component implying that their detectability is below the CTA capabilities, unless a different spectral

component is present at higher energies. On the other hand, magnetar bursts and flares (in particular the so called Giant Flares) are potentially very interesting targets for CTA, with the only disadvantage of their unpredictable time of occurrence. Giant flares are extremely energetic and bright events, reaching isotropic peak luminosities as high as a few 10^{47} erg s⁻¹ for a fraction of a second. However, they occur very rarely: only three have been seen from local magnetars in 40 years. The high luminosity of their short (< 1 s) initial peaks implies that they can be detected, with properties resembling those of short GRBs, up to distances of tens of Mpc by current hard X-ray instruments. Indeed, a few candidate extragalactic giant flares have been identified (Mazets et al. 2008; Frederiks et al. 2007; Svinin et al. 2021; Roberts et al. 2021). Of particular interest regarding CTA's perspective to detect giant flares is the case of the flare located in the Sculptor galaxy (NGC 253, at 3.5 Mpc) for which *Fermi*-LAT observation led to the detection of two high-energy photons with energies of 1.3 GeV and 1.7 GeV, likely produced via synchrotron mechanism (Fermi-LAT Collaboration et al. 2021). However, no emission from a magnetar has been yet detected at TeV energies (Abdalla et al. 2021; López-Oramas et al. 2021). For further discussion, see Section 4.6.

1.6 Other expected variable gamma-ray sources at TeV energies

In addition to the systems quoted above, it can be foreseen that CTA detects other variable gamma-ray sources that nowadays are a mere theoretical prediction. These include, for instance, runaway massive stars expelled from their formation site (del Valle & Romero 2014). The bow shocks created by their powerful stellar winds have been proposed as sites of particle acceleration responsible for non-thermal phenomena, so far mostly observed at radio wavelengths. Significant gamma-ray variability is predicted on times scales of ~ 1 year as the stars move across density inhomogeneities of their surrounding medium affecting the bow shock properties.

Another kind of variable gamma-ray source based on theoretical expectations are low-mass young stellar objects such as T-Tauri stars (del Valle et al. 2011). Here, particle acceleration would be related to fast reconnection events in the stellar magnetosphere. Similarly, massive young stellar objects (MYSOs) could also produce gamma-ray emission associated with fast outflows from accretion or supersonic ejecta (see e.g. Araudo et al. 2021 and references therein). Recently, the MYSO S255 NIRS 3 has been suggested as the counterpart of a HE source (de Oña Wilhelmi et al. 2023). Perspectives for detection would be maximized at least for the closest star forming regions (see discussion by the dedicated KSP on star-forming regions, Cherenkov Telescope Array Consortium et al. 2019).

Supergiant Fast X-ray Transients (SFXTs; see Sidoli 2017 for a recent review) are high-mass X-ray binaries (HMXBs) composed of an O or B type supergiant star and a compact object; normally a neutron star (NS) is assumed, since some of them are X-ray pulsars, although formally a black hole cannot be ruled out. Their X-ray outbursts are rare (the duty cycle is less than 5%, see Sidoli & Paizis 2018). A large dynamic range of 2 to 6 orders of magnitude (Romano et al. 2015) can be reached between quiescence and the outburst peak. Their outbursts, that can last up to a few days, are made of short (~ 2 ks), bright X-ray flares, typically reaching 10^{36-37} erg s⁻¹. The possibility that SFXTs are MeV/TeV emitters was discussed by Walter (2007) and Sguera et al. (2009). In particular, the latter noted the spatial proximity (positional association within the error circles at gamma-ray energies, typically $\leq 1^\circ$) of some SFXTs with AGILE and EGRET transient unidentified sources. To date, there are four unidentified gamma-ray transient sources (3EG J1122–5946, AGL J1734–3310, 3EG J1837–0423,

⁷ According to <https://asd.gsfc.nasa.gov/Koji.Mukai/novae/latnovae.html> (as of February 2024).

AGL J2022+3622/VER J2019+368) which are spatially correlated with members (or candidates) of the SFXT class: IGR J11215–5952 (Sguera 2009), IGR J17354–3255 (Sguera 2013), AX J1841.0–0536 (Sguera et al. 2009), and IGR J20188+3647 (Sguera 2009). However, it is worth mentioning that no SFXT flare has ever been simultaneously caught at both X-rays and MeV/TeV energies, implying that, besides the spatial overlap with known SFXTs, there is no other evidence supporting a physical association, to date.

Once CTA is operational some of these objects, and other unexpected ones, will likely enrich the list of known Galactic transient emitters.

2 SENSITIVITY OF CTA TO TRANSIENT DETECTION IN THE GALACTIC PLANE

CTA will have unprecedented sensitivity over a broad energy range and will devote a large amount of time to sources in the Galactic plane, both with a dedicated Galactic Plane Survey (GPS) (for details on the pointing strategy and expected results see CTA Consortium 2023) and with pointed observations on specific targets. These are ideal capabilities for the discovery of new Galactic transients at TeV energies.

It is then important to characterize the sensitivity of CTA in the Galactic plane. The differential sensitivity of CTA for detecting a new source is defined as the minimal flux of a source, multiplied by the mean energy squared within the given energy interval, such that the source is detectable at the 5σ significance level. It is defined within a given energy range, and for a given observation interval or exposure. We assume a test point source power-law spectral model,

$$F(E) = P_f \left(\frac{E}{E_0} \right)^{-\gamma} \quad (1)$$

where we set the pivot energy, $E_0 = 1$ TeV, and the spectral index, $\gamma = 2.5$, using typical values for Galactic VHE sources. The prefactor, P_f is varied as part of the sensitivity calculation, in order to find the minimal flux value for a 5σ detection. In order to be compatible with previous analyses (e.g. Fioretti et al. 2019), we also require that the source emits at least 10 gamma-ray photons. In addition, we validate that this number of events is larger than 5% of the corresponding contribution from backgrounds and foregrounds (cosmic rays; electrons; and other gamma-ray sources that can be coincident).

We explore the performance of CTA in the Galactic plane region for various short observation intervals. For illustration, the sensitivity of the Southern array is shown in Fig. 1, considering different putative source locations. In this example, we estimated the performance for short observation intervals of 10 minutes within the energy range 100–200 GeV, exploring the detection potential of new sources in the low-energy range of CTA. We use a publicly-available Galactic sky model, based on observations of known gamma-ray sources and interstellar emission from cosmic-ray interactions in the Milky Way (CTA Consortium 2023).⁸ We simulate our putative transients on top of the emission derived from this sky model, such that the latter constitutes an additional background to the search.

As may be inferred from Fig. 1, upward fluctuations of the sensitivity (requiring brighter transient emission for detection), are correlated with the steady emission from Galactic sources. In the selected energy range, the flux of the simulated Galactic foreground is mostly

below the level of a few 10^{-11} erg cm⁻² s⁻¹. This is of the same order as the nominal sensitivity of the observatory in the absence of foregrounds. Correspondingly, the overall degradation in sensitivity to transients is not expected to be significant.

In order to verify this, we calculated δS , the relative variation of the sensitivity (compared to the median value) for different Galactic longitudes. The steady foreground sources are concentrated in the inner Galactic region. We therefore derived δS for two regions in latitude, in order to enhance or suppress their effect. Away from the Galactic plane we find $\delta S \sim 2$ –3% which amounts to the intrinsic statistical uncertainty of the sensitivity calculation. In the more crowded inner region, the variation is of the order of 5–15%. This represents a mild increase in the flux threshold for a new transient source to be discovered, though only when coinciding with strong Galactic emitters.

We show the median sensitivity for various combinations of energy ranges and observation intervals in Fig. 2. Here we consider an area of 4 deg² next to the Galactic centre, where the steady emission is relatively strong. The observed variation in sensitivity is mild, of the order of 1–10%.

The presence of possible source variability is assessed in Section 4.1.1.1. Other topics such as the study of Galactic Centre sources and interstellar emission through observations of the Galactic Centre region and GPS and the prospects for the CTA and its scientific results are covered in other KSPs (see Cherenkov Telescope Array Consortium et al. 2019; CTA Consortium 2023)

We conclude that the performance of CTA is consistent with the corresponding nominal extragalactic sensitivity (in the absence of significant foregrounds).

3 DETECTABILITY OF TRANSIENTS OF UNKNOWN ORIGIN

Apart from the transient sources of clearly identifiable type, others of unknown nature could also be serendipitously observed e.g. during a scan of the GPS. To assess the detection capabilities of CTA for such sources we simulate the populations of 100 generic transients. We consider the relatively short observation time of 1 hour (compatible with the strategy defined in CTA Consortium 2023) during which it would be possible to detect the source and make a decision about further observations.

We simulated the variability of each source using the following lightcurve model:

$$F(t) = \frac{2F_0}{\exp\left(\frac{t_0-t}{T_r}\right) + \exp\left(\frac{t-t_0}{T_d}\right)}$$

where T_r and T_d stand for time rise and time decrease and t_0 is the time at which $F = F_0$; we normalize the lightcurve to $F = 1$ at its maximum. Such a lightcurve describes the flux of a transient during its growth, at peak and when it falls, allowing the simulation of observations at each of these stages. We assume T_r , T_d and t_0 to be in ranges 1 – 86400 s, 86400 – 604800 s and $T_d - T_r$ respectively.

We used the model of Yusifov & Küçük (2004) for the radial distribution of sources. The resulting spatial distribution is shown in Fig. 3. For simplicity, we did not take into account the visibility constraints, assuming that all sources are visible to either array at the time of observation.

For each population, the parameters defining the spectrum and the lightcurve of each source are assigned randomly for each of them, assuming a log-uniform distribution for the prefactor and a uniform one for other parameters. The pivot energy for all sources is 1 TeV.

⁸ Galactic sky model available at <https://zenodo.org/records/10008527>

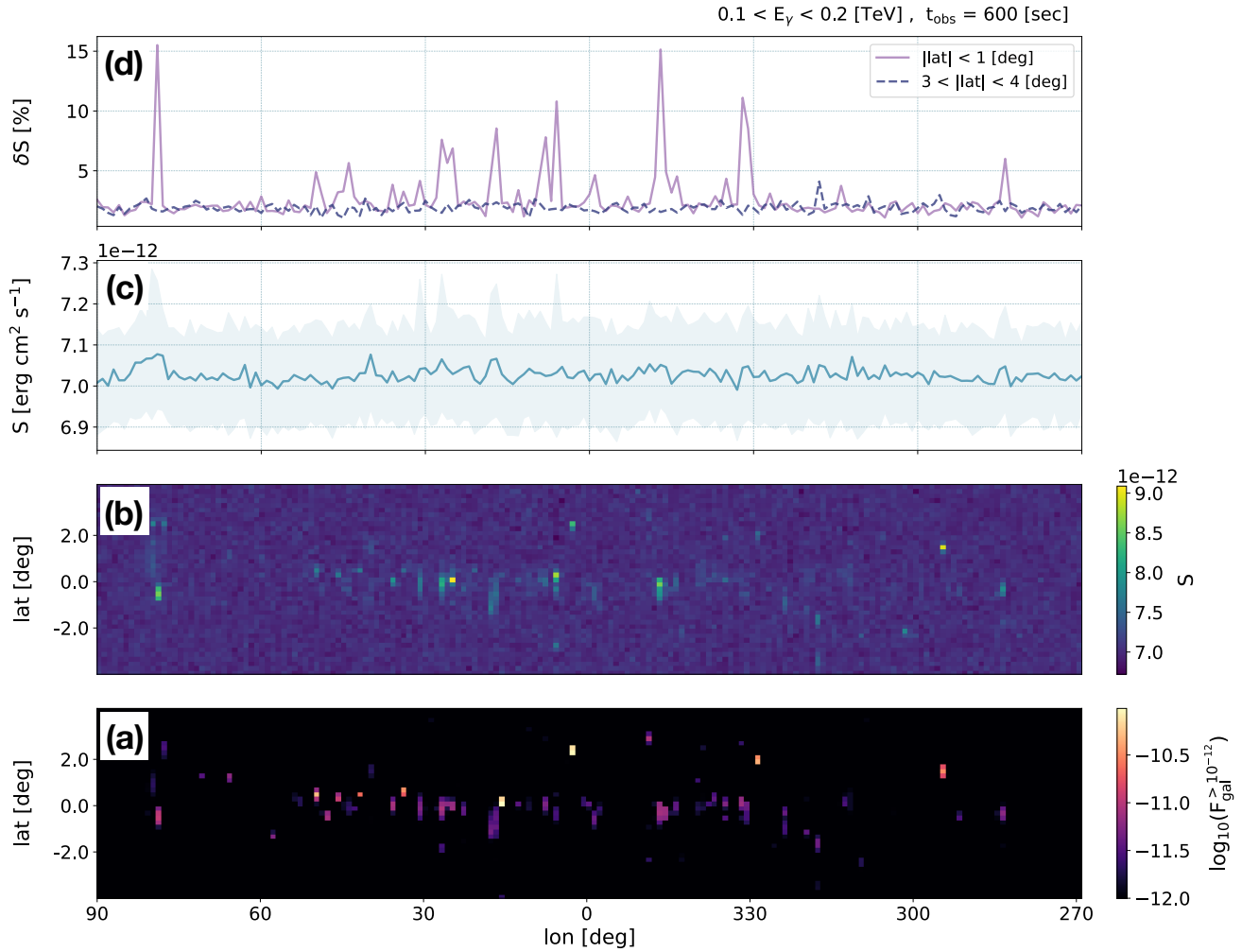


Figure 1. Differential flux sensitivity, S , of the Southern CTA array within 100–200 GeV for 10 min observation intervals, considering different putative source locations along the Galactic plane. *Panel (a)* shows a simulation of $F_{\text{gal}}^{>10^{-12}}$, the Galactic emission (Galactic diffuse emission and a simulated population of Galactic sources) above a threshold of 10^{-12} erg cm 2 s $^{-1}$, which is derived for different Galactic longitudes, lon , and latitudes, lat . *Panel (b)* shows the corresponding CTA sensitivity. *In panel (c)* we present the median of S for different longitudes within the range, $-4 < lat < +4$ deg, where the shaded uncertainty region represents the 1σ variance of S . Finally, *panel (d)* shows the relative 1σ variance, δS , (compared to the median) derived for two ranges in latitude, as indicated. The variance away from the Galactic plane ($3 < |lat| < 4$ deg) represents the intrinsic statistical uncertainty of the sensitivity calculation. The variance in the inner Galactic region ($|lat| < 1$ deg) includes the intrinsic uncertainty, as well as the additional effect of the Galactic foregrounds, which are concentrated in this region.

Table 1. Simulated populations. We consider sources with different spectral shapes and parameters.

Population	Spectrum	Prefactor (ph cm $^{-2}$ s $^{-1}$ TeV $^{-1}$)	Spectral index
1	power-law	$10^{-14} - 10^{-09}$	[-3.50, -1.50]
2	power-law	$10^{-18} - 10^{-13}$	[-3.50, -1.50]
3	log-parabola	$10^{-14} - 10^{-09}$	[-3.50, -1.50]
4	power-law (Alpha)	$10^{-14} - 10^{-09}$	[-3.50, -1.50]

Four simulated populations are summarized in Table 1. They include different spectral shapes and parameters. For each population we employed the 0.5 h IRFs for both CTA-N and CTA-S, and also

tested the Alpha configuration in the case of population 4. Both IRF sets contain three zenith angle observation options at 20° , 40° and 60° ; and they also account for the azimuth dependence coming from the geomagnetic field pointing direction: North, South or an average over the azimuth direction.

For each source, we simulate the photon events list for 1 hour both for the CTA-N and CTA-S sites with a 5.0° ROI centered at a source, without any other sources within it, accounting only for the IRF background as seen in Fig. 1 and Fig. 2. The energy ranges used for both configurations at each site are collected in Table 2. The energy dispersion effect has been also taken into account (according to the IRFs). We then performed an unbinned maximum likelihood fitting.

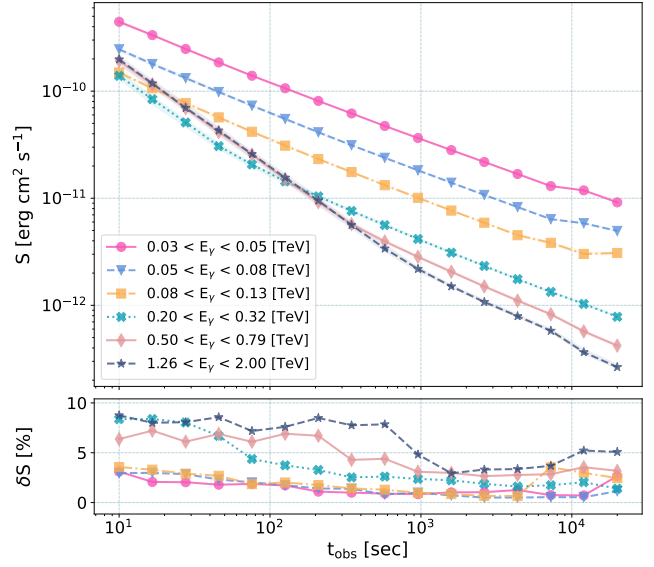
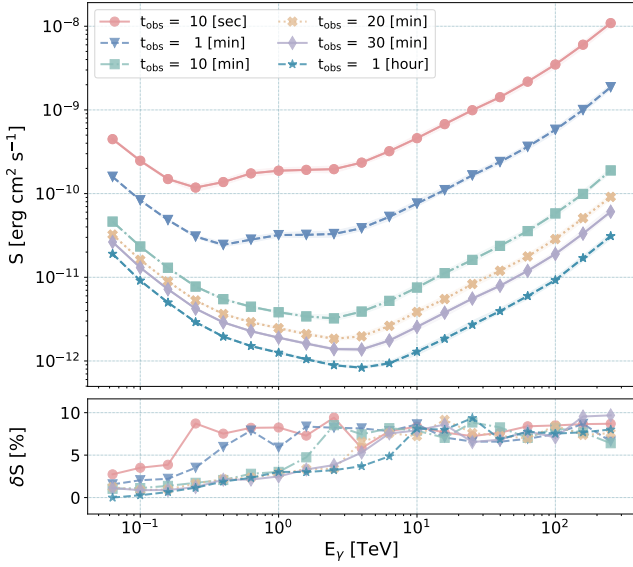


Figure 2. The differential flux sensitivity, S , of the Southern CTA array for different energy ranges, $0.03 < E_\gamma < 200$ TeV, and observation intervals, $10 < t_{\text{obs}} < 2 \cdot 10^4$ sec. The sensitivity is derived as the median value for various putative source positions, considering an area of 4 deg^2 close to the Galactic centre. The bottom panels show the relative 1σ variance of the sensitivity, δS , compared to the median. The variance accounts for both the intrinsic statistical uncertainty of the sensitivity calculation, and the degradation of performance due to the presence of steady sources.

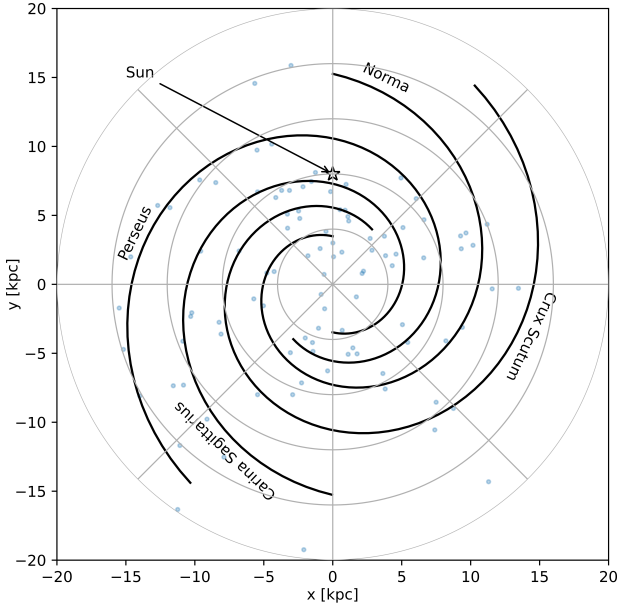


Figure 3. Spatial distribution of sources in the simulated populations.

The test statistic (TS) equal or higher than 25 is used as criterion for a source detection.

The results for all populations and observation configurations are presented in Fig. 4. We found that in the case of having a power-law spectra and fluxes in the range of $10^{-14} - 10^{-09} \text{ ph cm}^{-2} \text{ s}^{-1} \text{ TeV}^{-1}$, 73 – 83% of sources for 20° and 40° zenith angles and 65 – 74% of sources for 60° zenith angle will be detected, while for the population

Table 2. Energies (TeV) assumed in the simulations depending on the array location, configuration and zenith angle. Different energy ranges were assumed depending on the geomagnetic field (average, North, South) for CTA-N Alpha Configuration, as produced in the dedicated IRFs (Observatory & Consortium 2021).

Site	20°	40°	60°
CTA-N	0.03-200	0.04-200	0.11-200
CTA-S	0.03-200	0.04-200	0.11-200
CTA-N (Alpha)	0.03-200	0.04-200	0.06-200 (A) 0.12-200 (N)
CTA-S (Alpha)	0.04-200	0.06-200	0.08-200 (S) 0.18-200

with fluxes $< 10^{-13} \text{ ph cm}^{-2} \text{ s}^{-1} \text{ TeV}^{-1}$, CTA will not detect any source during 1 hour of observation. In most cases CTA-S performs marginally better than CTA-N, with the larger difference for the North magnetic field configuration. Adding a curvature to the spectrum does not affect the detection rate in a statistically significant way. Using the Alpha Configuration (which corresponds to a first construction phase) slightly decreases the detectability, which is expected due to the reduced number of telescopes and the lack of LSTs in the CTA-S Alpha configuration (Maier et al. 2023).

4 SOURCE DETECTION WITH CTA

Galactic transients that exhibit MeV-GeV emission are specially interesting to be studied with CTA, since it is already known that non-thermal mechanisms leading to gamma-ray production are at work. We aim at understanding whether these sources of interest can also emit VHE radiation, which can be produced by the same HE

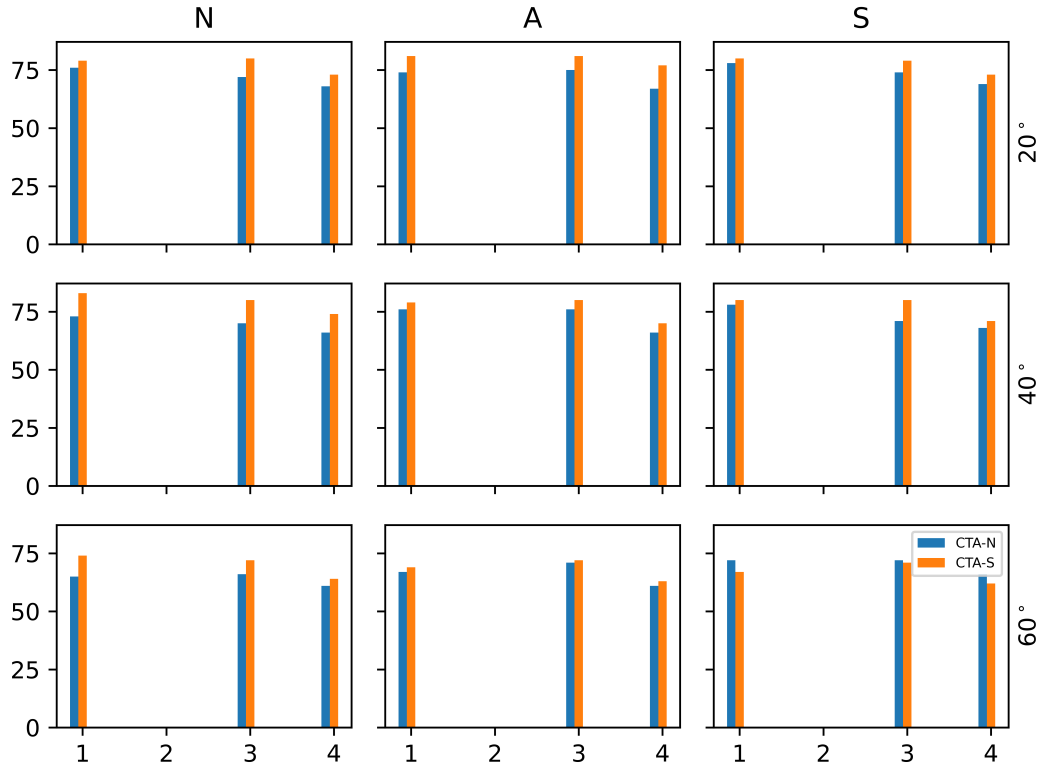


Figure 4. Number of detected sources in populations 1 to 4 for CTA-N (blue) and CTA-S (orange), including the Alpha configuration in population 4. From left to right: different configurations of the geomagnetic field (North, average and South). From top to bottom: different zenith angles (20° , 40° and 60°).

mechanisms and be detected as a spectral extension, or be created by an additional component at TeV energies.

4.1 High-mass microquasars

The microquasars of the Cygnus region, Cyg X-3, Cyg X-1 and the system SS 433 are the only microquasars that have been detected in the HE regime, hence they can be considered as potential targets for the CTA observatory. After the discovery of gamma-ray emission from SS 433 above 20 TeV by HAWC (Abeysekara et al. 2018a), the CTA observations of these microquasars will be crucial to shed light on the physical mechanism responsible for the VHE emission in this type of binary systems, by investigating the limits of extreme particle acceleration in the jet.

The importance of observing this subclass of binary systems with CTA has been previously discussed in Paredes et al. (2013). In particular, a detailed study on a possible detection of a TeV flare from Cyg X-1 was presented in that paper, showing conclusions similar to our findings (see Sect. 4.1.3.1). In this section, we show simulations on the first microquasar detected in the VHE regime, SS 433, and estimate the detectability both of transient and persistent emission from Cyg X-3 and Cyg X-1. Even if the detection of persistent emission is not the scope of this paper, we perform this additional exercise to complement the expectations to detect microquasars with CTA. For the case of the microquasars in the Cygnus region, we carried out several CTA observation simulations by using the latest prod5-v0.1 IRFs to check if these two systems could already be detected in the first years of operation of CTA. Almost all the simulations have been carried out in the lowest range of energies for the CTA observatory,

where the bulk of the emission from these binary systems is expected. For each set of observations, besides the emission from the microquasars, we simulated the main field sources of the Cygnus region: 2HWC J2006+341 (Araya & HAWC Collaboration 2019), VER J2016+371, VER J2019+368 (Aliu et al. 2014b), Gamma Cygni SNR (Ackermann et al. 2017; Abeysekara et al. 2018b), TeV J2032+4130 (emission model as detected by MAGIC before the periastron passage of November 2017, Abeysekara et al. 2018c). This approach also applies to the case of the LMXB V404 Cyg located in the same region (see subsection 4.2.1).

4.1.1 SS 433

SS 433 is a binary system containing a supergiant star that is overflowing its Roche lobe with matter accreting onto a compact object, either a BH or a NS (see e.g. Margon 1984; Fabrika 2004). Two jets of ionised matter, with a bulk velocity of approximately one quarter of the speed of light in vacuum, extend from the binary, perpendicular to the line of sight, and terminate inside the supernova remnant W50 (e.g. Fabrika 2004). The lobes of W50 in which the jets terminate about 40 parsecs from the central source, are accelerating charged particles, as it follows from radio and X-ray observations, consistent with electron synchrotron emission (Geldzahler et al. 1980; Brinkmann et al. 2007).

Abeysekara et al. (2018a) reported the results of the High Altitude Water Cherenkov (HAWC) Observatory of SS 433, collected between November 2014 and December 2017. In 1017 days of measurements with HAWC, an excess of gamma rays with a post-trial significance of 5.4σ has been observed in a joint fit of the eastern and western

interaction regions (namely *e1* and *w1*) of the jets of SS 433. The quality of the data allow us to set only ULs on the angular size of the emission regions, namely 0.25° for the east hotspot and 0.35° for the west hotspot at 90% confidence level. The VHE gamma-ray flux is consistent with a hard E^{-2} spectrum, though current TeV flux data from HAWC are not of sufficient significance to constrain the spectral index. The reported HAWC flux at 20 TeV is $2.4 \times 10^{-16} \text{ TeV}^{-1} \text{ cm}^{-2} \text{ s}^{-1}$ at *e1*, and $2.1 \times 10^{-16} \text{ TeV}^{-1} \text{ cm}^{-2} \text{ s}^{-1}$ at *w1*. HAWC detects VHE emission from the interaction regions up to at least 25 TeV, which is the highest energy measured up to now from microquasars.

The SS 433 region was also observed by H.E.S.S. as part of a Galactic plane survey, and during two further dedicated campaigns, resulting in about 200h of observations (H. E. S. S. Collaboration et al. 2024). These observations confirmed presence of two regions of gamma-ray emission at the positions of the eastern and western jets, with peak statistical significances of 7.8σ and 6.8σ , respectively. The reported fluxes at 1 TeV ($(2.30 \pm 0.58) \times 10^{-13} \text{ TeV}^{-1} \text{ cm}^{-2} \text{ s}^{-1}$ and $(2.83 \pm 0.70) \times 10^{-13} \text{ TeV}^{-1} \text{ cm}^{-2} \text{ s}^{-1}$ for the eastern and western jets correspondingly) are inline with HAWC data taking into account the spectral slopes of $\Gamma_e = 2.19 \pm 0.12$ and $\Gamma_w = 2.40 \pm 0.15$. Quality of the H.E.S.S. data also allow to study the energy dependence of the source morphology, demonstrating that while the gamma-ray emission above 10 TeV appears only at the base of the jets, the lower-energy gamma rays have their peak surface brightnesses at locations further along each jet, reflecting an energy-dependent particle energy loss timescale.

Analysis of the *Fermi*-LAT data led to the discovery of the significant HE gamma-ray emission from the region around SS 433 (see Bordas et al. 2015; Sun et al. 2019; Rasul et al. 2019; Xing et al. 2019; Li et al. 2020). However, the analysis is model dependent and can lead to very different conclusions on the position and extension of the source. In Rasul et al. (2019), authors report evidence at 3σ level for the modulation of the γ -ray emission with the precession period of the jet of 162 days. This result suggests that at least some of the gamma-ray emission originates close to the base of the jet. Li et al. (2020) detected HE emission in the vicinity of SS 433 which shows periodic variation compatible with the precessional period of the jets.

Kimura et al. (2020) investigated both hadronic and leptonic scenarios for the GeV-TeV gamma-ray emission from SS 433. They found that the existing data can be explained by both the hadronic and leptonic models. The hadronic scenarios predict higher-energy photons than the leptonic scenarios, and future observations with CTA and LHAASO are needed to unravel the emission mechanism of GeV-TeV gamma rays. A preliminary association of LHAASO sources with known TeV sources based on their position reported in the first LHAASO catalog of gamma-ray sources (Cao et al. 2023b) indicate the presence of 2 LHAASO sources located at 0.26° and 0.15° from the western and eastern lobes of SS 433 correspondingly, but further observations are needed to confirm these associations.

To test the capability of CTA to study the origin of the VHE emission from the source we simulate the source with both the east and west lobes as extended sources in the energy range 0.1 - 100.0 TeV. We simulate observations with 10, 30 and 50 hours of exposure time. These simulations were repeated on each of the lobes assuming different extensions roughly corresponding to the different characteristic scales of source morphology as observed with H.E.S.S. (H. E. S. S. Collaboration et al. 2024) (see Table 3), to provide the expected detectability in terms of their size. The TS and flux of each lobe was measured for both the Northern and Southern CTA arrays, see Tables 4 and 5.

Table 3. Extension model values applied to the lobes of SS 433 that were simulated with CTA.

Model	σ_w	σ_e
1	0.001	0.001
2	0.0625	0.0875
3	0.175	0.125
4	0.26	0.1875

Table 4. Comparison of the detectability of the western and eastern lobes of SS 433 with varying values of source extension and exposure time for the Northern array.

Model	TS_{10h}^{West}	TS_{10h}^{East}	TS_{30h}^{West}	TS_{30h}^{East}	TS_{50h}^{West}	TS_{50h}^{East}
1	52.0	76.8	229.1	303.7	354.3	477.2
2	38.9	10.9	121.9	105.2	152.0	114.5
3	7.9	9.4	23.7	57.6	57.1	100.2
4	2.4	8.2	6.3	20.1	9.4	37.5

Table 5. Comparison of the detectability of the western and eastern lobes of SS 433 with varying values of source extension and exposure time using for the Southern array.

Model	TS_{10h}^{West}	TS_{10h}^{East}	TS_{30h}^{West}	TS_{30h}^{East}	TS_{50h}^{West}	TS_{50h}^{East}
1	137.4	184.6	738.8	821.9	886.3	1261.4
2	59.2	73.6	178.4	384.2	273.1	401.0
3	11.1	31.3	76.3	104.3	79.5	226.7
4	2.6	7.2	44.4	60.3	34.7	115.9

4.1.1.1 Central source emission and putative variability While we do not expect to detect variability in the VHE emission coming from the lobes, microquasars are known to have flaring emission on various timescales coming from its central source. To test the possibility of CTA to detect a central source and its putative variability we simulate the local region of SS 433 with the diffuse background and the nearby MGRO 1906+06 source, where SS 433 consists of both the aforementioned lobes and a central point source. All simulations were performed when the H.E.S.S. ULs on the central source flux were not published yet and we assumed that the flux of this central source is approximately half that of the western lobe, which is roughly consistent with the ULs reported in (H. E. S. S. Collaboration et al. 2024). The lobes and the central source were both assumed to have an index of -2.0 and a pivot energy of 20 TeV (see Abeysekara et al. 2018a). The lobes were given an extension that matches *Model 2* as described in Table 3. Batches of 100 simulations were run using the North and South site IRFs at multiple different exposure times ranging from 30 minutes to 50 hours. The flux was calculated after every simulation and the total data was compiled into histograms for each exposure time to determine the error range of the detections. As SS 433 could be viewed from both the north and south hemispheres the results of error measurements from both sites were compared to determine which can produce more sensitive detections. Fig. 5 shows the the comparison of this flux error ratio. Obtained results demonstrate that Southern array is better suited to study the source.

As previously mentioned, the region surrounding SS 433 does

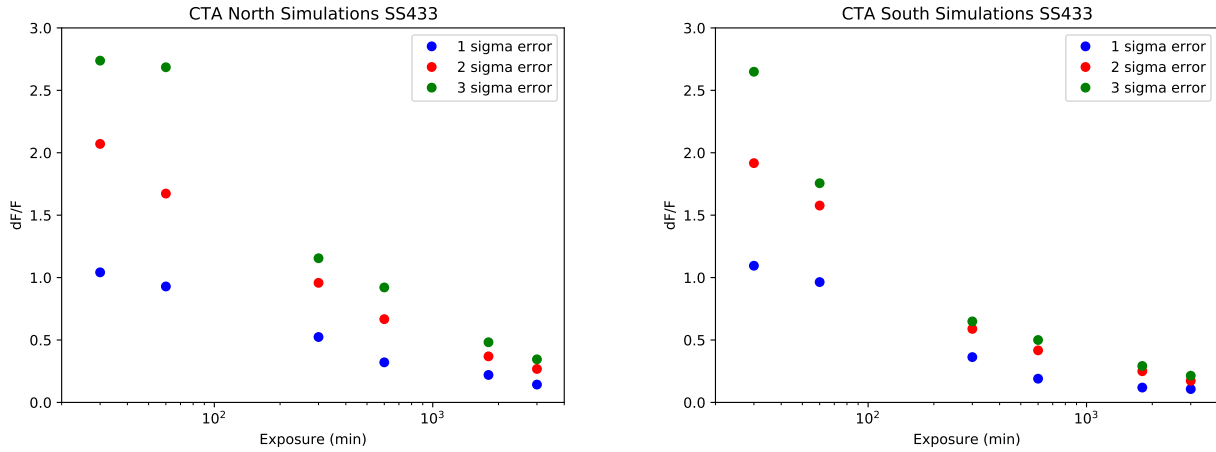


Figure 5. Comparison of the relative flux errors at different exposure times for the Northern and Southern arrays.

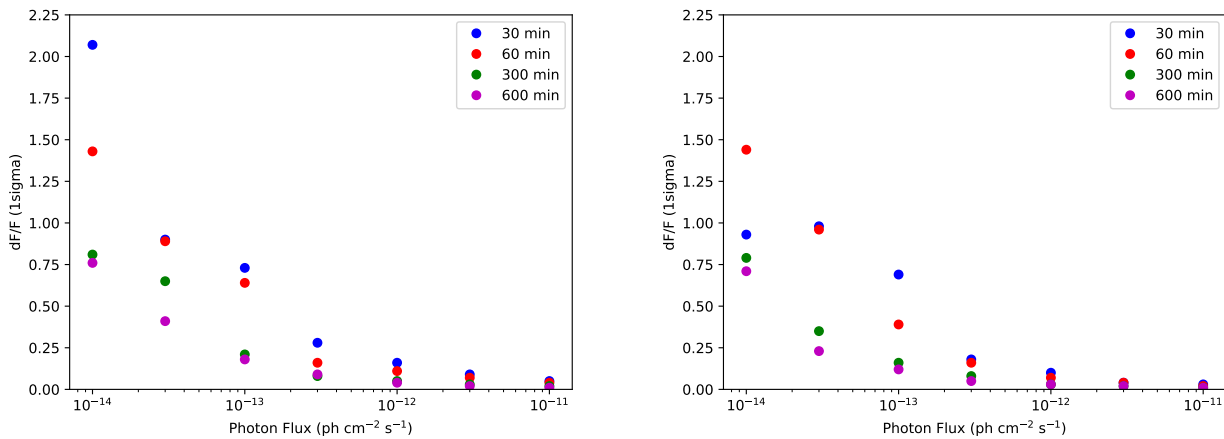


Figure 6. Dependence of the 1 sigma relative flux error ratio on the photon flux for the Northern (left) and Southern (right) arrays. Different exposure times are given by different colours as indicated in the legend.

not contain many other TeV sources and could be described as an uncrowded region. Conversely, sources such as the gamma-ray binary LS 5039 are located in a region with multiple nearby TeV sources (crowded region). Using the previous setup, simulations were run for a source modelled like the central SS 433 source located at the position of LS 5039 to determine if a crowded region would change the results. It was found that the observed flux of the central source and its error were very similar for both cases of a crowded and uncrowded regions.

The procedure used to test the effectiveness of CTA on dim transient sources can also be tested with sources of arbitrary intensity to determine what level of variability can be observed with shorter exposures. The results of observing sources in the same position and region of SS 433 with different fluxes (> 1 TeV) are shown in Fig. 6. Similarly to the simulations of the SS 433 central source at different exposures (Fig 5), the Southern array configuration consistently produce a lower ratio between the 1 sigma error and the input flux of the simulation. Based on the simulations run at different fluxes, sources with a photon flux $< 1 \times 10^{-13}$ $\text{ph cm}^{-2} \text{s}^{-1}$ will require exposure times of more than 10 hours in order to detect any expected variability. However, for sources with a flux $\geq 1 \times 10^{-13}$ $\text{ph cm}^{-2} \text{s}^{-1}$, CTA

may be able to detect variability as low as $\sim 10\%$ observing from 5 to 10 hours. At a photon flux $\geq 3 \times 10^{-12}$ $\text{ph cm}^{-2} \text{s}^{-1}$ the 1 sigma ratio gets as low as $\sim 5\%$ with exposure times of 0.5–1.0 hour long, meaning that even low variability may be detectable from relatively bright sources with very short observations.

4.1.2 Cyg X-3

Cyg X-3 is a HMXB located at a distance of ~ 9 kpc (Reid & Miller-Jones 2023). The companion star is a Wolf-Rayet (WR) with a strong wind mainly composed of helium. The nature of the compact object is still unknown, although a black hole scenario is favored (Zdziarski et al. 2013; Antokhin et al. 2022). The orbital period is very short, ~ 4.8 hours, indicating that the compact object is very close to the WR star, totally enshrouded in its stellar wind (orbital distance $\sim 3 \times 10^{11}$ cm). The binary system is known to produce giant radio flares (flux > 10 Jy), produced by synchrotron processes from a relativistic jet oriented very close to the line of sight. Transient gamma-ray activity above 100 MeV was reported for the first time in 2009 by AGILE (Tavani et al. 2009) and Fermi-LAT (Fermi LAT Collaboration et al. 2009). The flaring activity (typical duration: 1-2 days) was observed

in coincidence with a repetitive pattern of multi-frequency emission (Piano et al. 2012): the gamma-ray flares have been detected (i) during soft X-ray spectral states (around minima of the hard X-ray light curve), (ii) in the proximity of spectral transitions, and (iii) a few days before giant radio flares. In particular, transient gamma-ray emission was found when the system is moving into or out of the quenched state, a spectral state – characterized by a very low (or undetectable) flux at radio and hard X-ray frequencies – that is known to occur a few days before major radio flares.

The quenching activity of Cyg X-3 turns out to be a key condition for the observed activity above 100 MeV. According to theoretical models, a simple leptonic scenario – based on inverse Compton (IC) scattering between electrons/positrons accelerated in the jet and seed photons from the WR companion – can account for the flaring gamma-ray fluxes and the 4.8 h modulation detected by *Fermi*-LAT during the transient activity (Dubus et al. 2010). A simple phenomenological picture, based on dominant leptonic processes in the jet, can account for the non-thermal emission pattern: around the quenching, the jet would consist of plasmoids, ejected with high Lorentz factor. This transient jet would be responsible for the HE flare (for IC processes), produced in the proximity of the binary system ($10^{10} - 10^{12}$ cm), and it would subsequently produce the major radio flares (synchrotron processes), by moving out from the central engine (distances $> 10^{14}$ cm). MAGIC repeatedly observed Cyg X-3, both during hard and soft spectral states, but never detected any significant VHE activity from the microquasar (Aleksić et al. 2010).

4.1.2.1 Cyg X-3: transient emission We carried out simulations by assuming two different theoretical models based on IC processes in the jet (Piano et al. 2012; Zdziarski et al. 2018), in order to test the possibility of a CTA detection of transient VHE gamma-rays from Cyg X-3.

We performed a binned analysis in the energy range 100 GeV – 1 TeV with *ctools*, by simulating observations with the Alpha Configuration of the Northern array of the CTA observatory (IRF: *North_z20*), taking into account the energy dispersion. A multi-source input model with the main background TeV sources (see Section 4.1) and the CTA instrumental background (CTA_{IRF}Background) has been considered.

In the first case, we adopted a simple power-law spectrum (see Eq. 1) inferred from the leptonic *Model A* from Piano et al. (2012), where prefactor $P_f = 1.34 \times 10^{-21}$ ph cm⁻² s⁻¹ MeV⁻¹, index $\gamma = 4.5$ and pivot energy $E_0 = 1$ TeV. The leptonic model is based on IC scatterings between accelerated electrons in the jet and soft seed photons from the accretion disk (X-rays) and from the companion star (UV). We simulated 5 hour and 50 hour observations, and we investigated the resulting simulated data, by performing a binned analysis. The resulting spectra are shown in Fig. 7, together with the X-ray “hypersoft” spectrum (Koljonen et al. 2010), the AGILE flaring spectrum (Piano et al. 2012) and the MAGIC flux ULs observed during the soft states (Aleksić et al. 2010). All the spectra (not simultaneous observations) are referred to the same spectral state of Cyg X-3 when the transient gamma-ray activity is detected at MeV-GeV energies (quenched state). We show the reference theoretical model and the input simulated power-law, together with the CTA simulated spectra. By assuming this input spectrum we found no detection with CTA-N with 5-h observation and a weak hint of signal ($\sim 3\sigma$) for 50 hours of observation time.

In the second case, we assumed a different theoretical model, developed by Zdziarski et al. (2018) in order to fit the flaring spectrum from Cyg X-3 as detected by *Fermi*-LAT (cumulative spectrum of 49 1-day flares detected between August 2008 and August 2017).

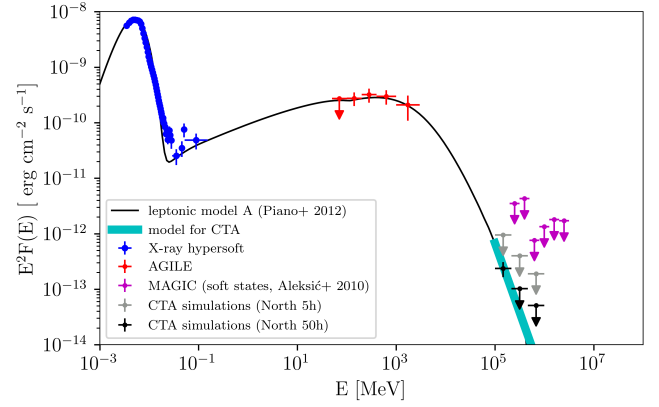


Figure 7. Multi-frequency spectral energy distribution of Cyg X-3. Black solid curve: leptonic model A (Piano et al. 2012). Cyan solid curve: CTA input model for the simulation. Blue points: “hypersoft” X-ray spectrum (Koljonen et al. 2010), RXTE-PCA and RXTE-HEXTE data (~ 3 to ~ 150 keV). Red points: HE gamma-ray cumulative flaring spectrum (Piano et al. 2012), AGILE (50 MeV – 3 GeV). Magenta points: VHE flux ULs (95% C.L.) from Aleksić et al. (2010), MAGIC (199 GeV – 3.16 TeV). Gray points: CTA flux ULs for a simulated observation of 5 h. Black points: CTA spectrum for a simulated observation of 50 h.

The theoretical model presented in their paper is similar to the one presented in Piano et al. (2012), but in Zdziarski et al. (2018), the electrons in the jet scatter blackbody soft photons from the companion star only. The orbital and geometrical parameters are similar. Also in this case, the model is focused on the HE emission from the microquasar ($E \leq 100$ GeV). Thus, we assumed a simple power-law extension of the model up to TeV energies (assuming: prefactor $P_f = 2.15 \times 10^{-19}$ ph cm⁻² s⁻¹ MeV⁻¹, index $\gamma = 2.85$ and pivot energy $E_0 = 1$ TeV). Similarly, we simulated 5 h and 50 h observations. The results of these simulations are shown in Fig. 8. In this case, by assuming a harder and brighter input spectrum, we found clear detections with CTA-N: $\sim 10\sigma$ with 5-h observation, $\sim 30\sigma$ with 50 h observation.

Thus, by assuming two simple power-law input spectra adapted from theoretical leptonic models – both created ad hoc in order to account for the flaring activity observed by AGILE and *Fermi*-LAT – a possible detection with CTA North is plausible even with a few hours observations. We cannot rule out to detect the 4.8 h orbital modulation, in the case of a prolonged TeV flare. A CTA detection of transient VHE gamma-ray activity would represent an unprecedented result for this elusive system, never observed at TeV energies. Nevertheless, a CTA non-detection would give new strong constraints on theoretical models about microquasars. The lack of a transient VHE signal from Cyg X-3, correlated with non-thermal flaring activity, could indicate that: (i) the TeV signal, eventually produced in the jet, is absorbed for pair production by the companion star’s UV photons; (ii) the acceleration efficiency in the jet is intrinsically low, the maximum energies of the jet particles are not sufficient to generate TeV photons.

4.1.3 Cyg X-1

Cyg X-1 is a HMXB, composed of a black hole ($M_X = 21.2 \pm 2.2 M_\odot$) and a O9.7Iab supergiant companion star ($M_{\text{opt}} = 40.6^{+7.7}_{-7.1} M_\odot$, Miller-Jones et al. 2021). The system is located at a distance of $2.22^{+0.82}_{-0.17}$ kpc (Miller-Jones et al. 2021), and the orbital period

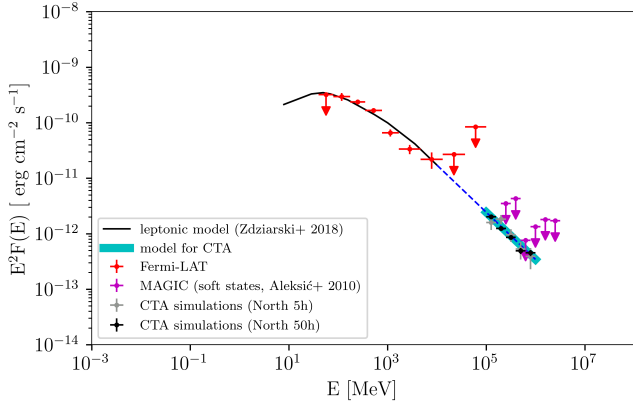


Figure 8. Gamma-ray spectral energy distribution of Cyg X-3. Black solid curve: leptonic model (Zdziarski et al. 2018). Power-law extension of the model up to TeV energies. Cyan solid curve: CTA input model for the simulation. Red points: HE gamma-ray cumulative flaring spectrum (Zdziarski et al. 2018), Fermi-LAT (50 MeV – 100 GeV). Magenta points: VHE gamma-ray flux ULs (95% C.L.) from Aleksić et al. (2010), MAGIC (199 GeV – 3.16 TeV). Gray points: CTA spectrum for a simulated observation of 5 h. Black points: CTA spectrum for a simulated observation of 50 h.

is 5.6 days. The X-ray spectra can be accurately modeled by hybrid Comptonization models (Coppi 1999). The soft state of Cyg X-1 is characterized by a strong disk blackbody component peaking at $kT \sim 1$ keV and a power-law tail extending up to ~ 10 MeV, related to Comptonization processes in the corona. In the hard state, the accretion disk is truncated and the emission from the corona is dominant. In this state, the coronal plasma is composed by a hot quasi-thermal population of electrons ($kT \sim 100$ keV) with a sharp cutoff at ~ 200 keV. At sub-MeV energies, the microquasar exhibits a non-thermal power-law tail with a strong linear polarization (Laurent et al. 2011; Jourdain et al. 2012). This emission could be ascribed either to synchrotron processes in the jet, by assuming a very efficient particle acceleration and strong jet magnetic fields (Zdziarski et al. 2014), or to the corona itself (Romero et al. 2014). Recent studies investigate the physical origin of this power-law tail at sub-MeV energies, detected during both soft and hard spectral states (Cangemi et al. 2021). Above 100 MeV, deep observations with *Fermi*-LAT found evidences of persistent emission from Cyg X-1 only during hard X-ray spectral states (Zanin et al. 2016; Zdziarski et al. 2017). Transient HE emission was observed by AGILE (Bulgarelli et al. 2010; Sabatini et al. 2010, 2013) on 1-2 day timescales, in coincidence with both hard and soft X-ray spectral states. At TeV energies, a hint of detection ($\sim 4\sigma$) was observed by MAGIC on September 24, 2006 (Albert et al. 2007), during a hard X-ray flare of Cyg X-1.

For Cyg X-1, we investigated the possibility that CTA will detect both transient and persistent emission from the microquasar.

4.1.3.1 Cyg X-1: transient emission. In this case, we carried out a simulated short-term observation of Cyg X-1, during a possible VHE gamma-ray flare. We simulated a 30-minute observation with the same setup reported in Section 4.1.2: a multi-source simulation with photon energies between 100 GeV and 1 TeV. We assumed, as input spectrum for the simulation, the same power-law observed by MAGIC in September 24, 2006 (Albert et al. (2007); prefactor $P_f = 2.3 \times 10^{-18}$ ph cm $^{-2}$ s $^{-1}$ MeV $^{-1}$, index $\gamma = 3.2$, pivot energy $E_0 = 1$ TeV). We obtained an overall detection of the source at a significance level of $\sim 38\sigma$. The resulting spectrum is shown

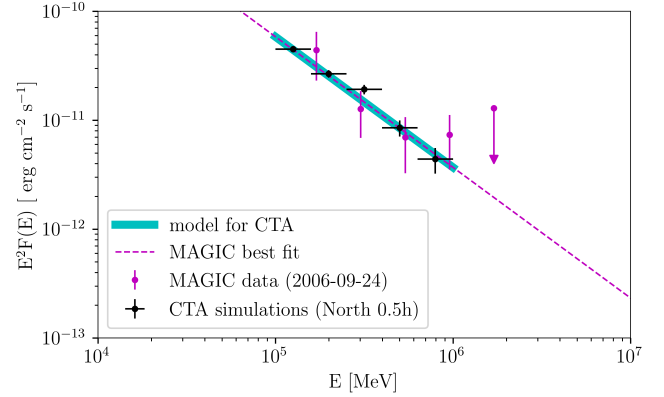


Figure 9. VHE gamma-ray spectral energy distribution of Cyg X-1, related to the 2006-September flaring activity. Magenta points: VHE gamma-ray spectrum from Albert et al. (2007), MAGIC (150 GeV – 1.9 TeV), accounting for 78.9 minutes of observation. Magenta dashed line: MAGIC best fit. Cyan solid curve: CTA input model for the simulation. Black points: CTA spectrum for a simulated observation of 30 minutes.

in Fig. 9, together with the observed flaring spectrum observed by MAGIC. Our results confirm that CTA will be able to detect a flare similar to the one reported by MAGIC in 2006 in a few minute observation, with unprecedented spectral accuracy.

4.1.3.2 CygX-1: persistent emission. Cyg X-1 exhibits persistent HE emission during the hard state, as observed by *Fermi*-LAT (Zanin et al. 2016; Zdziarski et al. 2017). Thus, we investigated the possibility of a CTA detection of VHE persistent emission above 100 GeV. Again, we assumed the same setup as reported in Section 4.1.2. We analyzed three different scenarios. In the first one, we assumed as input spectral model for CTA, a simple extension of the power-law spectral shape reported in the *Fermi*-LAT 4FGL Catalog, without any cut off around 100 GeV (Abdollahi et al. 2020). In the second scenario, we assumed a spectral shape based on a purely leptonic theoretical model, in which gamma-ray emission is produced due to IC scatterings in the persistent jet during the hard state (Zdziarski et al. 2017). According to this model, a sharp cut off – due to the Klein-Nishina effects – is predicted at ~ 100 GeV. In the third scenario, we assumed a spectral shape based on the lepto-hadronic theoretical model presented in Kantzas et al. (2021). In that paper, the authors modeled the GeV persistent spectrum as detected by *Fermi*-LAT during the hard state, by assuming that both electrons and protons are accelerated in the jet. A comprehensive model, based on a superposition of leptonic (IC scatterings) and hadronic processes (gamma rays from the decay of neutral mesons, produced in $p\gamma$ interactions) can properly fit the multi-wavelength spectrum up to the high-energy emission from Cyg X-1.

For the first hypothesis (4FGL-like spectrum), we assumed a simple power-law (assuming: prefactor $P_f = 3.2 \times 10^{-14}$ ph cm $^{-2}$ s $^{-1}$ MeV $^{-1}$, index $\gamma = 2.15$ and pivot energy $E_0 = 4.15$ GeV). A multi-source simulation with photon energies between 100 GeV and 1 TeV has been carried out. With this spectrum, we obtained a detection with a significance of $\sim 17\sigma$ for a 50h simulated observation. The resulting simulated spectrum is shown in Fig. 10, together with the *Fermi*-LAT 4FGL spectrum (Abdollahi et al. 2020), and the MAGIC flux ULs during the hard state (Ahnen et al. 2017b).

For the second hypothesis (spectrum inferred from Zdziarski et al. 2017), we assumed a simple power-law (with prefactor $P_f = 9.5 \times$

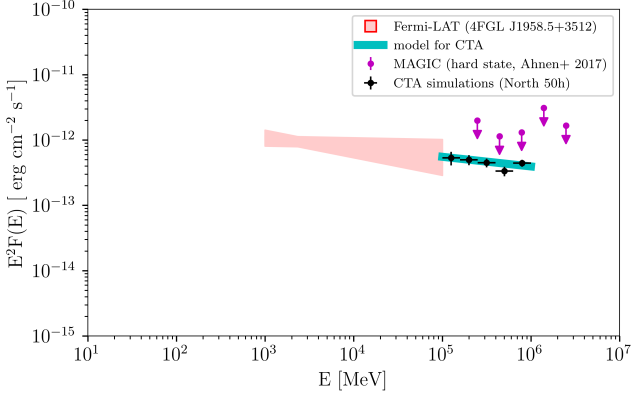


Figure 10. Gamma-ray SED of Cyg X-1, for a possible steady emission up to VHE. Red shaded region: The *Fermi*-LAT 4FGL Catalog HE steady spectrum, (Abdollahi et al. 2020), *Fermi*-LAT (1-100 GeV). Cyan solid curve: CTA input model for the simulation. Magenta points: MAGIC (160 GeV – 3.5 TeV) VHE ULs (95% C.L.) from Ahnen et al. (2017b). Black points: CTA spectrum for a simulated observation of 50 h.

$10^{-21} \text{ ph cm}^{-2} \text{ s}^{-1} \text{ MeV}^{-1}$, index $\gamma = 3.2$ and pivot energy $E_0 = 1$ TeV). A multi-source simulation with photon energies between 100 GeV and 1 TeV has been carried out. In this case, we did not detect any significant emission with CTA with a simulated observation of 50 h (significance $\sim 2\sigma$). The resulting differential spectral ULs are shown in Fig. 11, together with the theoretical model from Zdziarski et al. (2017), the HE gamma-ray spectra as detected by *Fermi*-LAT (Zanin et al. 2016; Zdziarski et al. 2017), and the MAGIC ULs related to the hard state (Ahnen et al. 2017b).

For the third hypothesis (spectrum inferred from Kantzas et al. 2021), we used as input the theoretical model itself, by simulating photon energies between 100 GeV and 100 TeV. We carried out the usual multi-source binned analysis, and we found a clear detection with a significance of $\sim 36\sigma$ for a 50h simulated observation. The resulting simulated spectrum is shown in Fig. 12, together with the theoretical model from Kantzas et al. (2021), the HE gamma-ray spectra as detected by *Fermi*-LAT (Zanin et al. 2016; Zdziarski et al. 2017), and the MAGIC flux ULs during the hard state (Ahnen et al. 2017b).

Thus, according to our simulations, CTA will be able to detect a possible persistent VHE gamma-ray emission from the jet of Cyg X-1, if the spectrum is not characterized by a sharp cut off around 100 GeV. According to purely leptonic models, a sharp cut off is expected below 1 TeV. On the contrary, hadronic processes could be responsible for a bright emission above 1 TeV, which could be detected by the CTA Observatory.

4.2 Low-mass X-ray binaries

LMXBs harbor a low-mass companion star and a black hole (or an accreting neutron star), object tightly connected to jet launching that are responsible for the non-thermal multi-wavelength emission (see review in Chaty 2022). Up to now, no LMXB has been detected at HE (apart from tMSPs) and only strong hints of emission at HE have been reported in V404 Cyg. No LMXB has neither been detected at VHE by any IACT. (see e.g. Aleksić et al. 2011; Ahnen et al. 2017a; H. E. S. S. Collaboration et al. 2018). The most recent X-ray outburst of a black hole LMXB (BH-LMXB) which was followed up by the IACTs MAGIC, H.E.S.S. and VERITAS was that of

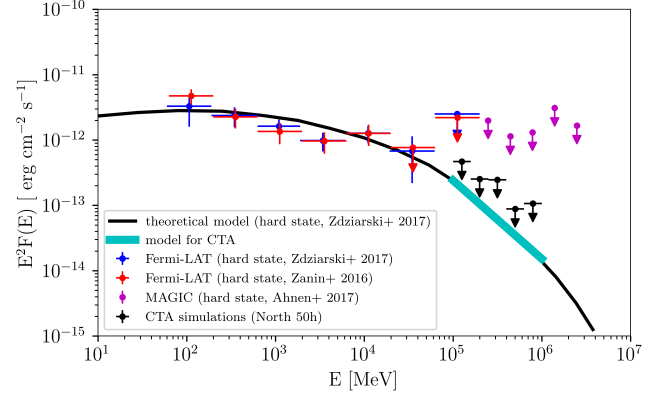


Figure 11. Gamma-ray SED of Cyg X-1, for a possible steady emission up to VHE. Black solid curve: theoretical model from Zdziarski et al. (2017), based on IC processes in the jet during the hard state. Blue points: HE steady spectrum during the hard state (Zdziarski et al. 2017), *Fermi*-LAT (60 MeV – 200 GeV). Red points: HE steady spectrum during the hard state (Zanin et al. 2016), *Fermi*-LAT (60 MeV – 200 GeV). Magenta points: MAGIC (160 GeV – 3.5 TeV) VHE flux ULs (95% C.L.) from Ahnen et al. (2017b). Cyan solid curve: input model used for the simulation. Black points: simulated spectrum for a CTA observation of 50 h.

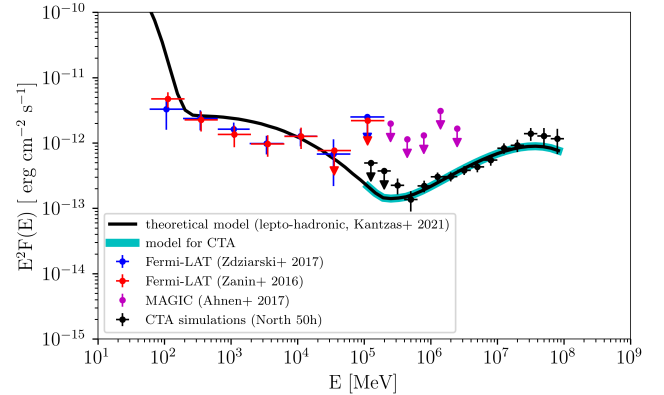


Figure 12. Gamma-ray SED of Cyg X-1, for a possible steady emission up to VHE. Blue, red and magenta points as reported in Fig. 11. Black solid curve: theoretical model from Kantzas et al. (2021), based on lepto-hadronic processes in the jet during the hard state. Cyan solid curve: input model used for the simulation. Black points: simulated spectrum for a CTA observation of 50 h.

MAXI J1820+070, without detecting any VHE emission (Abe et al. 2022). We examine here if CTA will be able to detect such a similar exceptionally bright outburst but for a hypothetical source located within a maximal distance of 4 kpc from Earth. Based on the theoretical lepto-hadronic model of Kantzas et al. (2022), used since the modeled LMXB can be considered a canonical source, we perform a number of simulations where we rescale the predicted VHE emission for a number of different jet inclination angles between 5° and 65° . We perform each simulation for a number of different hypothetical sources at different distances within 2 and 4 kpc.

In Fig. 13, we show the predicted VHE flux for a BH-LMXB with inclination angle of 30° assuming that the emission persists in three different energy bins between 0.1 and 10 TeV, for at least 2 weeks, and compare it to the CTA sensitivity curves (see Fig. 1).

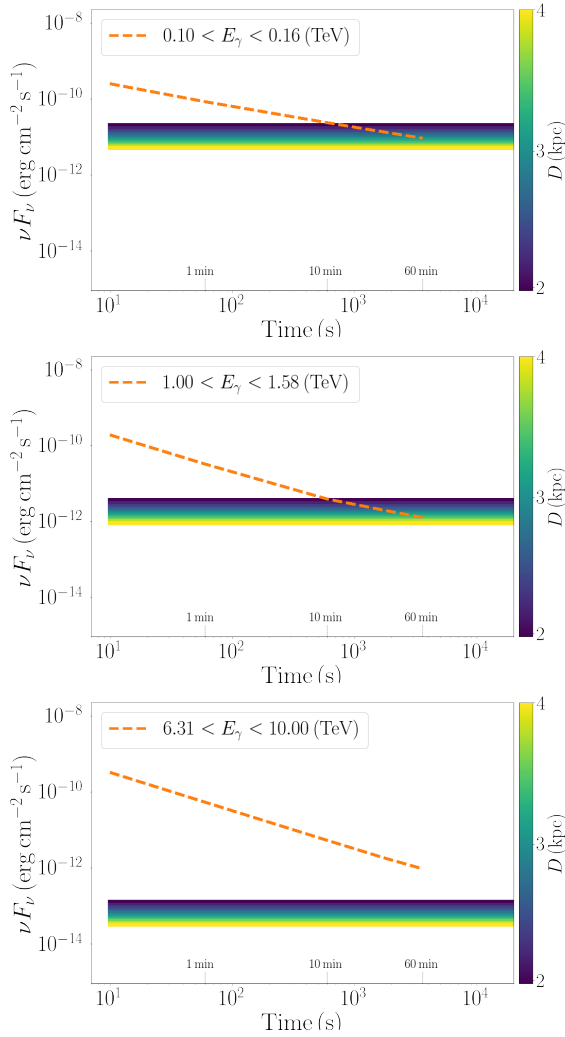


Figure 13. Predicted VHE emission of a hypothetical BH-LMXB for three different energy bins, as shown in the legends. The BH-LMXB follows the recent outburst of MAXI J1820+070, but with an inclination angle of 30° instead, and its distance is given by the colormap (lighter colors correspond to more distant sources). We assume an emission lasting at least two weeks. The CTA sensitivity for each energy bin is represented as a dashed orange line.

We overall see that CTA will be able to detect an outburst similar to MAXI J1820+070 in the sub-TeV regime within a few tens of minutes if the LMXB is located closer than ~ 4 kpc at energies < 1.6 TeV. The inclination angle of the LMXB we assume here is relatively small compared to the average value between 40 and 70° (see, e.g., Tetarenko et al. 2016), but LMXBs with an inclination angle greater than $\sim 30^\circ$ fail to be detected within the first hour of observations (Fig. 14). Sources with an inclination angle less than $\sim 20^\circ$ could be observed within a few minutes, such as the case of MAXI J1836–194 or V4641 Sgr, both microblazar candidates (Russell et al. 2014; Gallo et al. 2014).

4.2.1 The case of V404 Cyg.

The system V404 Cyg is a LMXB located at a distance of 2.39 ± 0.14 kpc, inferred through parallax measurements (Miller-Jones et al.

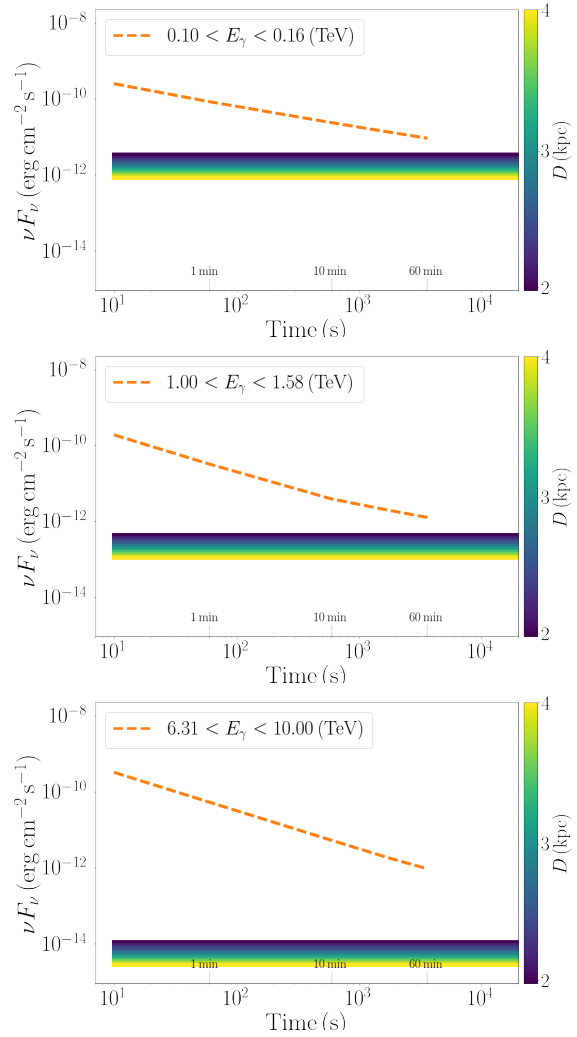


Figure 14. Same as Fig. 13 but for an inclination angle of 40° .

2009). The system is composed of a $9^{+0.2}_{-0.6} M_\odot$ black hole and a $0.7^{+0.3}_{-0.2} M_\odot$ K3 III companion star with an orbital period of 6.4714 ± 0.0001 days (Casares et al. 1992). LMXBs are known to undergo long periods of quiescence (years) and rapid outburst states (weeks). After a ~ 26 year-long quiescent phase, V404 Cyg entered in a bright active phase in the second half of June 2015. The outburst, lasting ~ 2 weeks, was observed in all the bands of the electromagnetic spectrum, from radio to GeV energies. AGILE-GRID and *Fermi*-LAT observed a strong hint of emission in gamma rays ($\approx 4\sigma$), coincident with the brightest peak of luminosity observed in radio, hard X-ray and soft gamma-ray bands (Loh et al. 2016; Piano et al. 2017). The gamma-ray event was observed between June 24 and 26 and it is simultaneous with rapid transitions between the optically thin and the optically thick phases of the radio emission in the jet, and coincident with a bright peak of the 511 keV emission line detected by INTEGRAL (Siebert et al. 2016). As for other microquasars, the HE emission could be related to either leptonic (IC scattering on soft photons) or hadronic processes (decay of π^0 mesons produced in proton-proton collisions) in the jet. Nevertheless, in this case the companion is an old spectral type, cold and small star, and it does not provide a sufficiently high density of seed photons and hadronic material in the

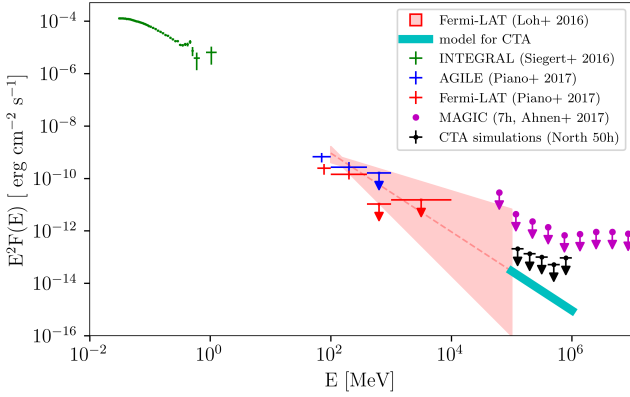


Figure 15. Multi-frequency SED of V404 Cyg, related to the 2015-June flaring activity. Green points: hard X-ray spectrum (Siebert et al. 2016), INTEGRAL data (30 keV – 2 MeV). Blue points: HE flaring spectrum (Piano et al. 2017), AGILE (50 MeV – 1 GeV). Red points: HE flaring spectrum (Piano et al. 2017), *Fermi*-LAT (60 MeV – 10 GeV). Red shaded region: HE flaring spectrum, (Loh et al. 2016), *Fermi*-LAT (100 MeV – 100 GeV). Magenta points: MAGIC (50 GeV – 10 TeV) VHE flux ULs (95% C.L.) from Ahnen et al. (2017a). Cyan solid curve: input model used for the simulation. Black points: simulated spectrum for a CTA observation of 50 h.

stellar wind. Thus, the HE emission is possibly related to interactions between the particles accelerated in the jet and the radiation (and the magnetic field) of the jet itself. MAGIC repetitively pointed at V404 Cyg between June 18 and 27, for more than 10 hours, but the observations did not show any significant emission at TeV energies (Ahnen et al. 2017a).

V404 Cyg: transient emission We carried out a 50-h CTA simulated observation for V404 Cyg with the same setup described in Section 4.1.2: 100 GeV – 1 TeV simulated photons with a multi-source approach. The CTA input spectral model for V404 Cyg is a simple extension of the power-law spectrum observed by *Fermi*-LAT during the 2015-June flaring activity and reported by Loh et al. (2016) (assuming: prefactor = 8×10^{-22} ph cm $^{-2}$ s $^{-1}$ MeV $^{-1}$, index = 3.5 and pivot energy = 1 TeV). The resulting spectrum from our simulation is shown in Fig. 15, together with the non-thermal HE spectra observed during the 2015-June flare. Thus, if we assume the same spectral trend as observed by the HE gamma-ray detectors, we expect no detection with CTA in a 50-h observation. This is in agreement with the simulations on LMXBs described in Subsection 4.2.

4.3 Transitional millisecond pulsars

Out of the three confirmed tMSPs, only PSR J1023+0038 is currently in the LMXB state, whereas XSS J1227–4853 and IGR J18245–2452 are currently in the RMSP state. As previously mentioned, other candidates were found through X-ray peculiar variability and association with *Fermi*-LAT sources (see review by Papitto & de Martino 2022). Particularly interesting are the two confirmed tMSPs PSR J1023+0038 and XSS J1227-485 that when in LMXB state they were found by *Fermi*-LAT with a luminosity of about 10^{34} erg s $^{-1}$ in the energy range 0.1–10 GeV, which is up to ten times brighter than the levels observed during the RMSP state (Papitto & Torres 2015; Torres et al. 2017). This fact makes them particularly interesting for a possible detection with CTA. In this Section, we

estimate the chances of detecting these two tMSPs with CTA given also their relatively close distance of about 1.5 kpc.

4.3.1 PSR J1023+0038

This tMSP was initially detected as a variable source in the radio band (Bond et al. 2002) and showing clear characteristics of an accretion disc around the compact object in the optical band. Later, Thorstensen & Armstrong (2005) suggested PSR J1023+0038 as an NS-LMXB. The observations did not reveal an accretion disc but the existence of a strong irradiation on the optical star from an unseen companion. The compact object was identified as a 1.69 millisecond radio pulsar in a 4.75 hr orbit around a 0.2 M_{\odot} companion star (Archibald et al. 2009b). In June 2013 the source came back to a LMXB state, where it has remained until now, and the radio pulsar signal switched off (Stappers et al. 2013). During the LMXB state, PSR J1023+0038 shows a peculiar behaviour in X-rays: it exhibits frequent modes switching between three different X-ray levels, dubbed high, low and flaring (Bogdanov et al. 2015). The HE gamma-ray emission detected by *Fermi*-LAT has been reported to brighten by a factor of 5 after the transition (Stappers et al. 2013). The average *Fermi*-LAT spectrum is described by a power-law with index 1.8 and a cutoff at an energy of 2.3 GeV according to Takata et al. (2014) and by a power-law with index 2 and an energy cutoff at 3.7 GeV, being the significance of the cutoff is 4.3σ level according to Torres et al. (2017). Neither pulsations nor steady emission were found in the VHE regime (Aliu et al. 2016). To test the capability of CTA to detect emission from this source we first studied the HE gamma-ray emission from *Fermi*-LAT during the LMXB state (2013–2021), in order to obtain the spectral parameters of the source. The two spectral models that have been considered for the CTA simulations are a logparabola and a broken power-law. The power-law with the exponential cutoff is not further considered because the cutoff at a few GeV would prevent a detection at VHE; whereas, a simple power-law extending in the energy range from GeV up to 1 TeV appears physically difficult to achieve. This is compatible by the low significance of the results by Takata et al. (2014) and Torres et al. (2017).

For the broken power-law: prefactor = $(0.06 \pm 0.01) \times 10^{-10}$ photons cm $^{-2}$ s $^{-1}$ MeV $^{-1}$, Index1 = -2.12 ± 0.03 , Index2 = -2.91 ± 0.06 , Energy break = (1.15 ± 0.09) GeV. For the logparabola: prefactor = $(0.34 \pm 0.007) \times 10^{-10}$ photons cm $^{-2}$ s $^{-1}$ MeV $^{-1}$, $\alpha = 2.23 \pm 0.02$, $\beta = 0.16 \pm 0.02$, Energy break = 0.524 GeV. Batches of 100 simulations were run using both CTA-N and CTA-S IRFs for 50, 100 and 200 hours of observations; we binned the simulated data into initial 20 logarithmic energy bins considering an energy range of 0.03–100 TeV. The resulting spectrum of PSR J1023+0038 is shown in Fig. 16 and, for simplicity, only the results with the highest statistic are reported (200 h observations). The full analysis results for the broken power-law model are reported in Table 6. We find that long integration times are needed to detect this tMSP, with at least 100 h for CTA-N and 50 h for CTA-S. The fit with a logparabola model did not converge.

4.3.2 XSS J1227-48538

XSS J1227-48538 was initially detected as a hard X-ray source and was tentatively identified as a cataclysmic variable, similarly to PSR J1023+0038, based on the double-peaked emission lines (typical of an accretion disc) in the optical spectrum (Masetti et al. 2006). While the low X-ray luminosity was not in contrast with a cataclysmic variable interpretation, the peculiar X-ray variability with mode

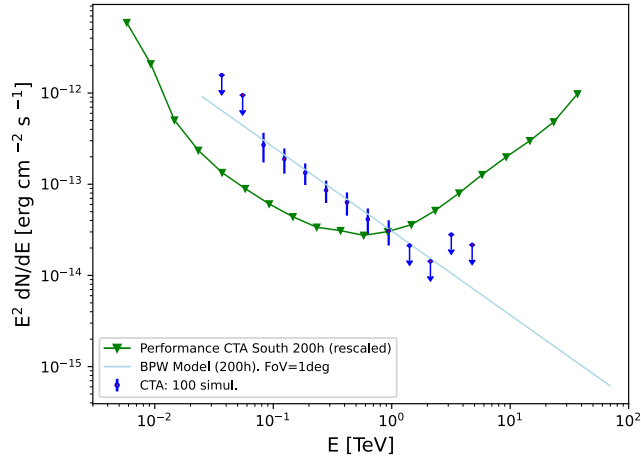


Figure 16. CTA-S simulations for the tMSP PSR J1023+0038 considering the broken power-law model. We consider 200 hours of observations. The CTA performance curve (green) is rescaled for 200 h.

Table 6. Broken power-law model significance's results for North and South IRFs, considering 50, 100 and 200 h of observations of the tMSP PSR J1023+0038.

	Hours	TS	σ
North	50	18.50	4.30
	100	39.86	6.31
	200	77.15	8.78
South	50	29.36	5.42
	100	55.47	7.45
	200	114.77	10.71

switching and the unexpected association with a *Fermi*-LAT source prone to identify XSS J1227-48538 as an unusual LMXB (de Martino et al. 2010). The system transitioned to a radio pulsar state between November 14 and December 21, 2012, characterized by the disappearance of the emission lines in the optical spectrum and the softening observed in the radio, optical, X-ray and gamma-ray bands (Bassa et al. 2014; Torres et al. 2017). Just after the transition, observations with the Giant Metrewave Radio Telescope allowed to detect a radio pulsar with a 1.69 ms spin period in a binary system with an orbital period of 6.9 hr (Roy et al. 2015). Before the transition to the radio state, the gamma-ray emission was a factor of 2 larger (Torres et al. 2017). The *Fermi*-LAT analysis performed for the period in which the source was in the sub-luminous disk state (2008-2012) provides results consistent with those reported by Xing & Wang (2015) and ? : XSS J1227-48538 is best described by a power-law with a cutoff at $E_{cut}=5.3$ GeV (at 3.4σ) and a spectral index of 2.

Similarly to PSR J1023+0038, the two spectral models considered for the CTA simulations are the logparabola and the broken power-law. As input models for the CTA simulations we considered the output from the *Fermi*-LAT study. For the broken power-law: prefactor = $(2.71 \pm 0.71) \times 10^{-12}$ photons $\text{cm}^{-2} \text{s}^{-1} \text{MeV}^{-1}$, Index1 = -2.23 ± 0.04 , Index2 = -2.77 ± 0.10 , Energy break = (1.32 ± 1.44) GeV. For the logparabola: prefactor = $(3.26 \pm 0.91) \times 10^{-11}$ photons $\text{cm}^{-2} \text{s}^{-1} \text{MeV}^{-1}$, $\alpha = 2.28 \pm 0.05$, $\beta = 0.09 \pm 0.02$, Energy break = (4.45 ± 5.42) GeV. We performed batches of 100 simulations using

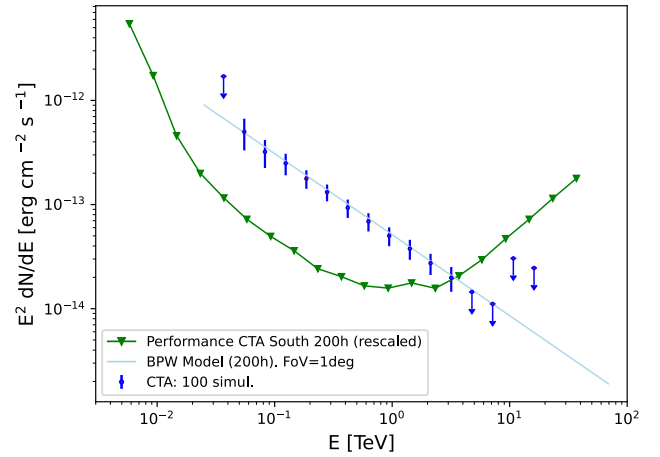


Figure 17. CTA-S simulations for the tMSP XSS J1227-48538 considering the broken power-law model. We consider 200 h of observations. The CTA performance curve (green) is rescaled for 200 h.

Table 7. Broken power-law model significance's results for South IRFs, considering 50, 100 and 200 h of observations of the tMSP XSS J1227-48538.

	Hours	TS	σ
South	50	66.26	8.14
	100	128.04	11.31
	200	253.99	15.94

only the CTA-S site IRFs and 50, 100 and 200 h of observations. The simulated data were binned into 20 logarithmic energy bins in an energy range of 0.03-100 TeV.

The resulting spectrum of XSS J1227-48538 is shown in Figure 17 and, for simplicity, we reported only the results with the highest statistics. The full analysis results are reported in Table 7. The source could be detected with CTA-S at 8.14σ with 50 h of observation. As for PSR J1023+0038, simulations considering the logparabola model failed to calculate the ULs.

Our simulations prove that the detection of the spectral component seen by *Fermi*-LAT from of close-by tMSPs when in a disc state could be possible with long exposures, provided that the emission has no cutoff at few GeVs. While this will likely not allow to catch fully a transition if lasting less than several days, here we demonstrate that once a transition has occurred CTA could be able to detect such type of sources, identifying tMSPs as VHE emitters for the first time. Also, if there are additional components (not considered here, such as magnetic reconnection of pulsar wind) it could be possible to detect changes in the HE flux along transitions.

4.4 Flares in PWNe: the Crab Nebula

The Crab Nebula is the best-studied PWN in the VHE regime. It is located at a distance of ≈ 2.2 kpc with ≈ 3.8 pc of size (Trimble 1973; Davidson & Fesen 1985). Since 2009, several rapid and bright flares have been detected from the nebula at HE with space-borne gamma-ray instruments (Tavani et al. 2011; Abdo et al. 2011; Buehler et al. 2012; Mayer et al. 2013; Striani et al. 2013; Arakawa et al. 2020). The observed flares presented variability timescales of hours.

During these flaring periods, the nebula showed rapid variations of flux and large releases of energy (Tavani et al. 2011; Abdo et al. 2011). Several multi-wavelength campaigns involving *Chandra* X-Ray Observatory, Keck Observatory and Very Large Array (VLA) (Weisskopf et al. 2013) and TeV searches by IACTs (Mariotti 2010; Ong 2010; H. E. S. S. Collaboration et al. 2014; Aliu et al. 2014a; van Scherpenberg et al. 2019) were carried out to follow these flares. However, none of them reported a correlation of the flares with morphological and/or spectral variations in the nebula.

CTA will cover a fundamental energy range to understand the origin of these flares: on the one hand, the low energy threshold will allow the sampling of the *Fermi*-LAT spectral shape at few tens of GeV of synchrotron nature, providing important clues on the acceleration and emission processes; on the other hand, the excellent sensitivity in the TeV regime will serve to explore the IC component that might arise at a detectable level from the electron population behind the MeV flares, off-scattering soft photon fields.

To evaluate the capability of CTA to detect Crab flares, we performed simulations of the SEDs both in flaring and steady (non-flaring) states of the nebula. We simulated flares of different spectral characteristics starting from a parent particle population, varying the physical properties of the environment. In particular, we simulated three types of flares: a very bright flare with similar flux (at hundreds of MeV) to the one observed by *Fermi*-LAT in April 2011 (Buehler et al. 2012; Striani et al. 2013) which is the flare with largest flux to date, and two dimmer flares corresponding to the first one re-scaled by a factor 0.5 and 0.1. Since no spectral variability has been reported at HE, we assume the same spectral model for these dimmer flares. The simulations of the nebula in flaring and steady states are performed for the CTA-N with the methods and tools presented in previous works (Mestre et al. 2020, 2021). The electron population was simulated with a fixed index (Γ_e) of 2.5, to guarantee the detection in the TeV regime (e.g., from 1.25 TeV to 50 TeV) of the brightest model of flare (see Fig. 6 of Mestre et al. 2021) in less than 10 h (see Table 8). The different flare models are computed for a magnetic field (B) in the acceleration region ranging from 100 μ G to 1 mG and compared (see section 2 of Mestre et al. 2021) to the steady nebula SED in both tens of GeV (e.g., from 20 GeV to 200 GeV) and TeV regimes. We obtained the simulations of the Crab nebula SED in steady state from Mestre et al. 2020. To compare the flaring and steady nebula simulations, we computed the mean total expected excess (e.g., counts from the source after background subtraction), both in flaring and steady state, in 21 bins of energy from 12 GeV to 200 TeV with observation times ranging from a few minutes to 500 h. We compared the excess distributions using the Pearson's chi-squared test, corresponding the null hypothesis (H_0) to the steady state. Then, we consider the flare implies a detectable flux level if H_0 is rejected at 95 % confidence level (CL).

The simulations performed show that the different models of flare are best detected in the GeV regime and in particular in less than an hour at energies below 200 GeV, see Fig. 18. In the TeV regime, flares dimmer than April 2011 flare by a factor 0.5 (at hundreds of MeV) would be detected in less than 10 h for $B < 500 \mu$ G (see Table 8). Some of the models considered imply an energy in TeV electrons larger than $\tau_{\text{syn}} \times L_\gamma \approx 5 \times 10^{43}$ erg, being τ_{syn} the synchrotron cooling time, and $L_\gamma \sim 2 \times 10^{35}$ erg s $^{-1}$, the luminosity of the nebula in gamma rays (Rudak & Dyks 1998). However, note that the energy in electrons available in the nebula is not limited to the one computed above if particle re-acceleration takes place, which would introduce additional boosts in the electron population energy reservoir. The simulations performed, together with previous results reported (see Mestre et al. 2021), provide excellent prospects for

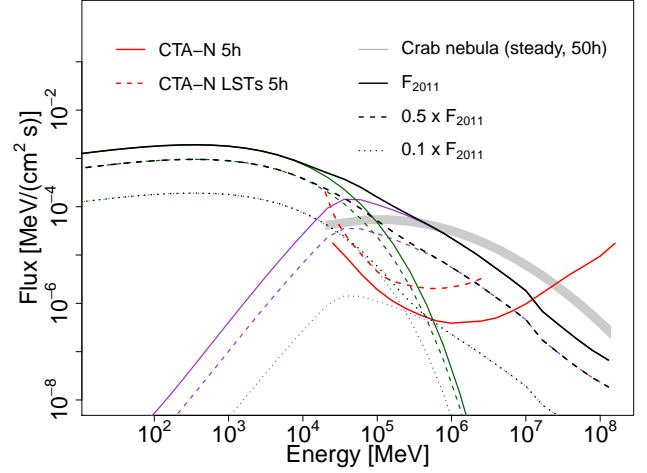


Figure 18. The synchrotron (green lines), IC (purple lines), and total (black lines) emission from the Crab Nebula for different flare models. The solid lines correspond to the model fitted to the *Fermi*-LAT April 2011 flare data at energies above 80 MeV for a particle index of 2.5. The dashed and dotted lines correspond to the same model re-scaled by a factor of 0.5 and 0.1, respectively. All the models are computed for a magnetic field of 500 μ G. The red solid and dashed lines correspond to the sensitivities of the CTA-N and, if considering only its four LSTs for 5 h of integration time, respectively. The Crab Nebula steady spectrum simulations for 50 h of observation time with CTA-N are noted with the gray shaded area (3σ region).

Table 8. In the second, third, and fourth columns, the observation time (in hours) necessary to detect different models of flares from 1.25 TeV to 50 TeV with CTA-N. The first column indicates the magnetic field chosen for the acceleration region. The observation times in the second column are computed for flare models fitted to the *Fermi*-LAT SED (at the moment of maximum flux level) of the April 2011 flare. For the third and fourth columns, the LAT SED (dubbed F_{2011}) was re-scaled prior to the fit by a factor of 0.5 and 0.1, respectively. The models with an asterisk imply an energy in electrons above 1 TeV larger than 5×10^{43} erg. We assume Crab is in flaring state during the entire observation time.

Model B [μ G]	Model SED		
	F_{2011}	$0.5 \times F_{2011}$	$0.1 \times F_{2011}$
1000	8.0	166*	> 500*
500	0.8	6.0*	> 500*
100	0.02	0.07	32*

detecting flares from the Crab Nebula with CTA, especially for the LST subarray, featuring the best sensitivity at energies of a few tens of GeV.

4.5 Novae

The only nova that has been detected at TeV energies so far is the symbiotic system RS Oph (Acciari et al. 2022; H. E. S. S. Collaboration et al. 2022; Abe et al. 2023) which shows recurrent outburst every 15-20 years and harbours a white dwarf accreting from a late-type giant companion star. However, it could be argued that the detection is due to selection-effects based on the fact that RS Oph is relatively nearby (see below). By number, novae that involve a small, low-mass donor such as a main sequence star (these are usually the *classical*

novae, see Chomiuk et al. 2021) are by far the most common type of system. The majority of novae have been observed in outburst only once in a human life timescale, and so far only a handful of novae are known to erupt with a recurrence time of \sim tens of years. It has been predicted from binary population synthesis studies (Kemp et al. 2021, 2022) that most commonly, novae with evolved donors are more likely to contribute to the total current Galactic nova rate, even though by number these systems make up a smaller fraction of nova binaries.

As pointed out recently by De et al. (2021), a large number of novae in optical bands might be being missed due to a number of sources residing behind and in the Galactic bulge. Taking obscuration by dust into account, De et al. (2021) estimated a current Galactic nova rate of $43.7 \pm_{8.7}^{19.5}$ per year. This is notably much larger than the actual Galactic nova detection rate of $\lesssim 10$ per year.

Kemp et al. (2022) estimated the Galactic nova rate to be 33 per year. That study showed that the most common type of nova in our Galaxy today is expected to originate from a binary system involving a giant-like donor (see Fig. 11 in the aforementioned paper as a guide). As mentioned previously, currently the only system to have clearly been detected at VHE (and detected also at HE) is the symbiotic recurrent nova RS Oph. Though some groups have investigated detailed modelling of shock generation in nova systems (Hachisu & Kato 2022; Metzger et al. 2016), which is believed to be mainly hadronic in nature, it is still not clear how many Galactic novae would be detectable by CTA at and beyond the \sim TeV energy range. The majority of novae thus far detected at GeV energies with no clear evidence for a TeV component have been classical novae (not symbiotic systems like RS Oph, see e.g. Zheng et al. 2022). Nonetheless, we anticipate several more novae could be observed with CTA (see Chomiuk et al. 2021), particularly if these novae are detected at other wavelengths early on enabling rapid triggering and follow-up. However, assuming we can expect of the order of ~ 30 Galactic novae per year, even with adequate triggering, it is unlikely that all of these outbursts will be detectable by CTA. If CTA-N would have been operational since August 2008 to April 2023, it would have been able to perform observations of 7 novae detected in HE gamma-ray by *Fermi*-LAT, in the 5 nights after their detection in optical. Assuming a similar rate of novae detected at HE gamma-ray in the future, it means that CTA-N would observe ~ 0.5 novae per year triggered by their HE gamma-ray emission.

CTA observations will be important to put constraints on the maximum energies attainable in nova explosions and the physical mechanisms involved in the production of VHE gamma rays. We estimated the capability of CTA to detect nova outbursts based on both theoretical modelling and empirical results. First, simple theoretical considerations based on the RS Oph detection are adopted to assess the gamma-ray emission at different outburst stages, following the approach in Acciari et al. (2022); H. E. S. S. Collaboration et al. (2022). Second, a parametric study based on phenomenological parameters involved in the emission of gamma rays in nova outbursts is performed to estimate the parameter space we could constrain with CTA observations. Finally, we considered dedicated numerical simulations of RS Oph to assess the expected detectability with CTA.

4.5.1 Modelling approach

We explored the capability of CTA to constrain the physical parameters of nova phenomena of different types, building up from basic arguments. The expected gamma-ray emission is obtained for different properties of a shock expanding with velocity $v_{\text{sh}}(t)$, generated by ejected material of total mass $M_{\text{ej}}(t)$ slamming into the companion

star's wind and producing gamma rays through hadronic interactions. To accelerate protons to high energies via diffuse shock acceleration (DSA), the magnetic field has to be amplified in the shock. The maximum energy particles attain at a shock is limited ultimately by the Hillas condition (Hillas 1984). However a more constraining limit is determined by either the time taken before radiative cooling dominates over acceleration, or by the necessary escape of the particles up-stream of the shock, in order to excite magnetic field fluctuations to a sufficient level ahead of the shock (Bell 2004). The maximum energy E_{max} in the particle spectrum, defined as a power-law function with an exponential cutoff, can be then described as:

$$E_{\text{max}} = 10 \left(\frac{v_{\text{sh}}}{5000 \text{ km/s}} \right) \left(\frac{R_{\text{sh}}}{1 \text{ AU}} \right)^{-1} \left(\frac{B_*}{1 \text{ G}} \right) \text{ TeV}, \quad (2)$$

with R_{sh} the position of the shock with respect to the white dwarf, and B_* the companion surface magnetic field (typically ~ 1 G for a red giant). R_{sh} can be expressed in terms of shock velocity, for which we assumed free expansion during the first few days, followed by radiative expansion when entering the Sedov-Taylor phase (Bode & Kahn 1985). The particle flux per unit of time and energy is computed using the condition that a fixed fraction (50%) of the kinetic energy of the protons ($E_{\text{kin}} = \frac{1}{2} M_{\text{ej}} v_{\text{sh}}^2$) is transferred to non-thermal particles (Acciari et al. 2022; H. E. S. S. Collaboration et al. 2022). Once the particle spectrum is defined as function of these three parameters (v_{sh} , B_* , M_{ej}) at different evolutionary stages of the shock expansion, we derive the gamma-ray emission originated by proton-proton interaction assuming a density of the ejecta which can be approximated following equation 4 in Acciari et al. (2022). The particle spectrum and density was used to compute the non-thermal emission, using the Naima spectral model class (Zabalza 2015) included in Gammapy.

In Fig. 19 we show the expected gamma-ray flux at different times from the nova explosion, considering several physical parameters in the shock. The upper panels show the expected emission for an explosion similar to RS Oph, with B_* , M_{ej} equal to 1 G and $10^{-6} M_{\odot}$, respectively, located at a distance of 2 kpc (left) and of 4 kpc (right). The effect of increasing the star surface magnetic field (10 G) and decreasing the ejecta mass ($10^{-7} M_{\odot}$) is shown in the bottom panels, for a fixed distance of 2 kpc. For reference, the isoflux line at $10^{-13} \text{ TeV cm}^{-2} \text{ s}^{-1}$ is marked when possible with a white line. The region below such line should be easily accessible to CTA.

4.5.2 Parametric space study

We utilised a phenomenological approach to study the parameter space of gamma-ray emission from novae. The emission was assumed to be produced by hadronic processes from π^0 decay (Kafexhiu et al. 2014), as indicated by the gamma-ray emission of RS Oph (see Section 4.5.3). The π^0 decay radiative model was parameterised using the target proton density (n_{h}) and the relativistic proton energy distribution. For the latter, we considered a particle distribution function parameterised as a power-law model with an exponential cutoff. We described the parameter space under study as a 3D space, where we set the parameter space domain in the range of plausible values based on observed novae at gamma rays. A 2D grid was defined with different values for the prefactor (A) and the cutoff energy (E_{cp}) of the proton energy distribution. The former in the range between $A = [10^{28}, 10^{32}]$ protons eV^{-1} at a pivot energy of 100 GeV and the latter between $E_{\text{cp}} = [10, 1000]$ GeV. Two slices for the target proton density were used for the third axis, $n_{\text{h}} = 10^8 \text{ cm}^{-3}$ and $n_{\text{h}} = 10^{11} \text{ cm}^{-3}$, which correspond to typical shock density values in novae (Metzger et al. 2016). The distance to the gamma-ray

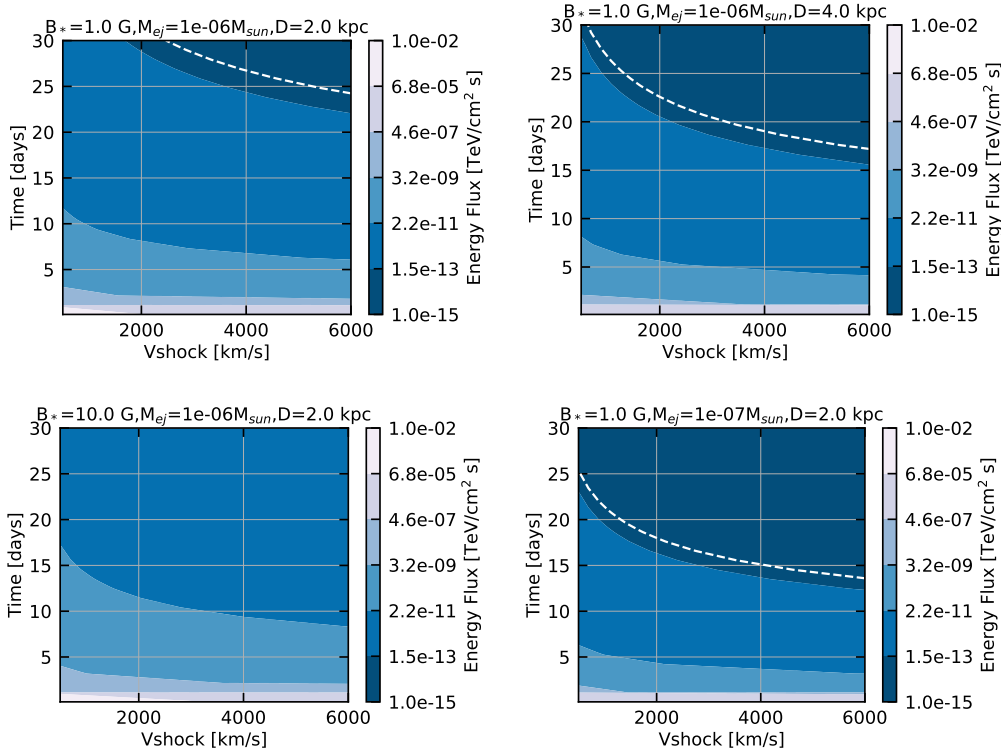


Figure 19. Expected energy flux in gamma rays with time after nova explosion as a function of shock velocity, integrated above 10 GeV. Top left: for an RS Oph-like system at 2 kpc. Top right: for the same physical properties yet at a larger distance of 4 kpc. Bottom left: with increased magnetic field strength. Bottom right: with decreased mass-loss rate. In all plots the white dashed line indicates the CTA isoflux line at 10^{-13} $\text{TeV cm}^{-2} \text{s}^{-1}$. Below this line the region should be easily accessible to CTA.

emitter was fixed to $d = 2$ kpc. The spectral energy distribution for each model was obtained using the software package *Naima* (Zabalza 2015).

The emission detectability was assessed for both arrays of CTA using the official IRFs from `prod5-v0.1` in the Alpha configuration (20deg-AverageAz for 5 h observation time). The results of the simulations for CTA-N and CTA-S are shown in panels *a* and *b* of Fig. 20, respectively. The total proton energy above 100 GeV (W_p) multiplied by $\frac{r_h}{d^2}$, hereafter “effective proton energy reservoir”, was used as a function of E_{cp} to display the ratio between the integral source flux and the CTA sensitivity. This ratio was computed to obtain a qualitative estimation of the detectability of CTA for each model in the parameter space. The higher the integral flux-to-CTA-sensitivity ratio, the more feasible the detection. Moreover, the region where we would detect each model with CTA in at least one energy bin is lower-delimited in Fig. 20 by a dashed orange line to have a more precise boundary of the detection region. Therefore, the region between the dashed orange line and the white region (integral flux-to-CTA-sensitivity close to 0) delimits the border of the parameter space where CTA will likely begin to detect the gamma-ray emission of the models. Qualitatively, RS Oph would be located approximately in the top right corner of Fig. 20, while V959 Mon (the first classical nova discovered by *Fermi*-LAT; Ackermann et al. 2014) would be in the lower left region of the plots.

The integral gamma-ray emission and the integral flux-to-CTA-sensitivity ratio in Fig. 20 increases as the effective proton energy reservoir and E_{cp} increase. Both top regions of plots *a* and *b* in Fig. 20 have positive values of integral flux-to-CTA-sensitivity ratio

(about 30% of the total combinations), while the bottom region do not (about 70% of the total combinations). When comparing the results between CTA-N and CTA-S, the former extends the parameter space region with positive integral flux-to-CTA-sensitivity towards models with $E_{cp} < 250$ GeV. On the other hand, the latter presents a wider detection region towards $E_{cp} > 250$ GeV than CTA-N. CTA-N overperforms CTA-S with about 10% more detections. The better performance of CTA-N at low energies is expected because the parameter space under study was restricted to produce most of the gamma-ray emission below 1 TeV and it is also connected with the presence of four LSTs in the CTA-N Alpha configuration, as it is observed from current novae detected at gamma rays. Therefore, the lack of LSTs, which dominates the CTA sensitivity at these energies (Cherenkov Telescope Array Consortium et al. 2019), in the Southern array (Alpha configuration) will reduce the parameter space of detectability with CTA-S.

Thus, CTA is expected to give strong constraints only to a sub-space of the whole parameter space under study. For about 30% of the area of the parameter space covered in Fig. 20 could be likely detected with CTA, in particular, where the relativistic protons have a high value of prefactor and cutoff energy. Assuming that the target proton number density is the number density of the main ejection of matter in the outburst, the results suggest that for denser ejecta, the detection region with CTA will cover a wide range of parameter values of the relativistic proton energy distribution. CTA-N should outperform CTA-S for novae with $E_{cp} < 250$ GeV, while for $E_{cp} > 250$ GeV, CTA-S should perform better than CTA-N at high energies.

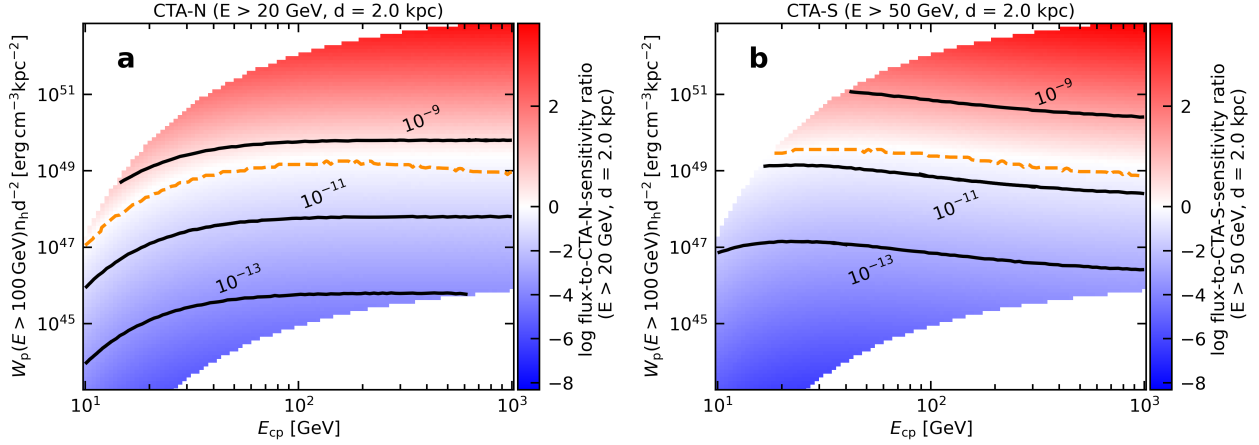


Figure 20. Logarithmic integral flux-to-CTA-sensitivity ratio for CTA-N (*panel a*), integrated above 20 GeV and CTA-S (*panel b*), integrated above 50 GeV for different values in the defined parameter space (see text) of n_h , cutoff energy (E_{cp}) and prefactor (A) of the proton energy distribution function at a fixed distance of $d = 2.0$ kpc. The sensitivity was computed for a total observation time of 5 hours. The orange dashed line indicates the domain in the parameter space with detection in at least one energy bin for different values of n_h , E_{cp} and A . Solid black lines are curves at constant integrated flux (10^{-13} , 10^{-11} and 10^{-9} $\text{cm}^{-2}\text{s}^{-1}$) above 20 GeV and 50 GeV for CTA-N and CTA-S panels, respectively

4.5.3 RS Oph

RS Oph is a symbiotic nova formed by a high-mass white dwarf ($1.2 - 1.4 M_{\odot}$) and a red giant star (M0 III, Anupama & Mikolajewska 1999), which transfers material to the compact object. In the literature, its distance has been estimated ranging from 1 kpc to 5 kpc (Barry et al. 2008, see also the discussion about the distance estimation in Section C.1 of the supplementary material of Acciari et al. 2022), being the most recent value of about 2.68 ± 0.16 kpc from Gaia DR3 catalog (Gaia Collaboration 2020) RS Oph undergoes recurrent nova outbursts with a periodicity of about 15 years. Its last eruption occurred in August 2021. Covered widely at different wavelengths, the 2021 outburst was detected at VHE gamma rays, adding a new object class to the list of VHE emitters. The HE and VHE gamma-ray emission was consistent mainly with a hadronic origin (dominated by π^0 decay), likely originated by the interaction of the ejected material with the dense wind of the red giant (Acciari et al. 2022; H. E. S. S. Collaboration et al. 2022). The gamma-ray spectrum showed hints of hardening with time produced by the migration of gamma rays to higher energies (Acciari et al. 2022). The HE light curve presented a power-law decay after reaching the maximum emission phase. The index of the temporal decay at HE with *Fermi*-LAT and the one obtained at VHE by the H.E.S.S. Collaboration were compatible within errors with values 1.35 ± 0.07 and 1.43 ± 0.18 , respectively (Cheung et al. 2022; H. E. S. S. Collaboration et al. 2022). It is expected that RS Oph will undergo another outburst when CTA will be in operation. Hence, we carried out numerical simulations of RS Oph to estimate its detectability with CTA along the temporal evolution of the outburst.

4.5.4 RS Oph: CTA simulations

We performed the numerical simulations of RS Oph with CTA using the official IRFs from prod5-v0.1 for the CTA northern and southern arrays. In particular, the closest IRFs set to the culmination of RS Oph in the CTA-N and CTA-S site were used (North-40deg-SouthAz, South-20deg-NorthAz) for 0.5 h observation time. A total of 59 daily observations of 1 hour each were simu-

Table 9. Daily parameter values of the log-parabola spectral models used to simulate RS Oph. Adapted from Acciari et al. (2022).

Model day	Prefactor at 130 GeV [$10^{-10} \text{ TeV}^{-1} \text{ cm}^{-2} \text{ s}^{-1}$]	α	β
Day 1	5.40	3.86	0.194
Day 2	4.54	3.73	0.175
Day 3	5.37	3.64	0.173
Day 4 – 59	5.00	3.44	0.147

lated starting one day after the beginning of the nova outburst (batches of 100 simulations per day). We simulated this source based on the gamma-ray spectral and temporal profile reported by the MAGIC and H.E.S.S. Collaborations, respectively. The best daily-fit spectral log-parabola models from Acciari et al. (2022) were considered to model the gamma-ray emission. Spectral variations were only contemplated for the simulations of the first four days, when spectral information in Acciari et al. (2022) was available during the outburst. The spectral parameter values utilised in the different log-parabola models are shown in Table 9. After the fourth day, the spectral profile was fixed to the one from the last day with spectral information (fourth day), and the simulated gamma-ray emission was scaled to follow the power-law temporal decay reported by H.E.S.S. We set the index value of the power-law decay to 1.4.

The statistical detection significance as a function of time is shown in Fig. 21. The results confirm that RS Oph would be clearly detected with CTA-N and CTA-S for the first days, reaching a detection significance of about 60σ and 30σ in an hour with CTA-N and CTA-S, respectively. RS Oph is not only detectable with CTA during the first days after the outburst, but CTA would also daily detect RS Oph up to 20 and 15 days after the outburst with the northern and southern arrays, respectively. If we consider the combined data of 5 and 10 adjacent days with CTA-N, the detection would be possible even up to 36 – 40 and 46 – 55 days, respectively. The 5σ detection would be limited down to 23 – 27 and 38 – 47 days with CTA-S. The resulting

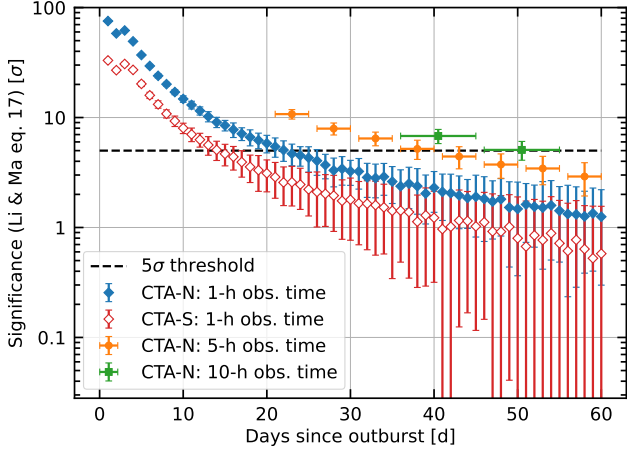


Figure 21. Daily statistical detection significance (equation 17 of Li & Ma 1983) from 1-hour simulated observation with CTA-N and CTA-S (blue filled diamonds and red empty diamonds, respectively) as a function of the number of days since the outburst of RS Oph. The 5-day (i.e. 5-h observation time, filled orange circles) and 10-day (i.e. 10-h observation time, filled green squares) combined significance for CTA-N are computed when the daily and 5-day statistical detection significance reach a 5σ detection (dashed black line), respectively. Error bars correspond to the standard deviation of the statistical detection significance distribution for the 100 simulations per day.

SED for the first simulated observation (day 1 after the outburst) is shown in Fig. 22 together with the observed spectrum obtained with MAGIC for the same observation time. The results suggest that CTA will be able to probe the gamma-ray emission for several weeks after the outburst with a precise spectral coverage at least during the first days. Using 1-h observation, CTA would be able to characterize the curvature of the VHE gamma-ray emission of RS Oph. For example, for the simulated observation of day 1, a log-parabola spectral model is preferred over a power-law model at 3.7σ .

Consequently, if one assumes that the next RS Oph outburst follows the same behaviour as the 2021 eruption, a plausible assumption based on the similarities observed at radio, optical and X-ray for the first weeks between 2006 and 2021 outbursts (Munari et al. 2022; Acciari et al. 2022; Page et al. 2022), CTA observations can provide detailed coverage of the gamma-ray emission during the future RS Oph outburst. Also, we could probe the maximum energy of the accelerated particles and the nova physical conditions across different outburst stages.

4.5.5 Other novae

To date, RS Oph is the only recurrent nova system from which gamma-ray emission at TeV energies has been detected during outburst. Nevertheless, several other recurrent novae, in particular symbiotic binary systems with high mass-transfer rates and dense winds, are also promising potential gamma-ray emitters. T Coronae Borealis (T CrB) in particular is a nearby symbiotic binary system, located closer to Earth than RS Oph, from which two prior outbursts have been observed in optical wavelengths (Schaefer 2023). Models predict that the next outburst will occur in 2024.4 ± 0.3 years (Schaefer et al. 2023) and, if a shock evolution comparable to RS Oph can be assumed, particle acceleration and detectable VHE gamma-ray emission is highly expected.

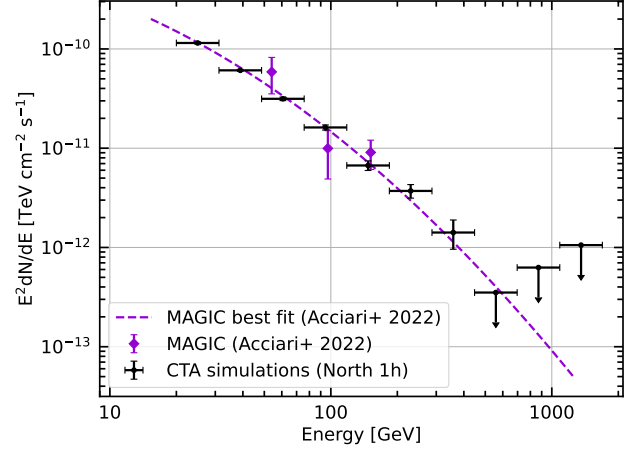


Figure 22. VHE γ -ray SED of RS Oph after 1 day since the outburst. The best-fit model from Acciari et al. (2022) using MAGIC and *Fermi*-LAT for the first night of observation is used (magenta dashed line) to simulate the source with CTA. The CTA-N flux points for a 1-hour observation time are shown as black points. Also, the MAGIC flux points (computed using 1-h observation time of data after cuts) from Acciari et al. (2022) are displayed (magenta points).

Recurrent novae - those from which more than a single outburst has been observed - tend to be associated with symbiotic binary systems due to their high mass transfer rate. This also renders them good candidates for particle acceleration to very high energies. Although MeV to GeV emission has been detected from classical novae by *Fermi*-LAT, the extension of their spectral energy distributions into the energy range detectable by IACTs is not expected a priori. Only continued observations of a range of novae during outburst with different physical properties will provide further insights into particle acceleration occurring in these systems.

4.6 Magnetars: discussion

On April 15, 2020, the *Fermi*-GBM and the *Fermi*-LAT instruments detected MeV and GeV gamma-ray emission from a giant flare event of a magnetar located in the NGC 253 galaxy (Roberts et al. 2021; *Fermi*-LAT Collaboration et al. 2021). The first time detection of GeV emission from a giant magnetar flare is particularly interesting, with the detection of two photons with energies 1.3 GeV and 1.7 GeV. According to *Fermi*-LAT Collaboration et al. (2021), these two GeV photons are produced via synchrotron emission considering the presence of a strong magnetic field which is generated in the shocks. It is proposed that these GeV photons are produced in the dissipation associated with the collision of the giant flare outflow and the external shell generated from swept-up material. This indicates that non-thermal processes accelerating particles at high-energies are at work. IC scattering can also occur in these events, and giant magnetar flares have been proposed as potential GeV-TeV emitters. TeV emission on millisecond timescales could be produced during giant flare events, which might be luminous enough to be detectable by IACTs (Lyubarsky 2014; Murase et al. 2016), including CTA. This TeV emission could be produced via synchrotron maser mechanism, triggered by strong magnetic disturbances from the magnetosphere and propagating outwards, until they dissipate by interacting with the ambient nebula. In the case of dissipation of disturbances within

the magnetar wind, a non-thermal tail can plausibly arise, potentially leading to the production of VHE gamma-ray emission (Metzger et al. 2020).

Magnetars are also relevant for their possible connection with other transient sources, such as, e.g., GRBs, super luminous supernovae, and fast radio bursts (FRB).

The association of a burst from the Galactic magnetar SGR 1935+2153 with an extremely bright FRB-like radio pulse on April 28, 2020 led to the first unequivocal association between FRBs and magnetars (CHIME/FRB Collaboration et al. 2020; Bochenek et al. 2020; Mereghetti et al. 2020; Tavani et al. 2021). The radio flare showed a double-peak structure, pattern also detected at X rays. The X-ray burst was of intermediate energetics, significantly too faint to be classified as a giant flare. However, even if the X-ray emission was not particularly energetic, this burst showed a harder spectra with respect to the typical bursts from SGR 1935+2154 and other magnetars.

Comparing the peak emission of the April 28, 2020 burst (Mereghetti et al. 2020), which reached a value of $50 \text{ ph cm}^{-2} \text{ s}^{-1}$ (in the 15-50 keV band) to other energetic transient events, such as GRB 190114C (MAGIC Collaboration et al. 2019), we see that the X-ray energetics are compatible with those of the second X-ray peak. Current IACTs such as H.E.S.S. (Abdalla et al. 2021) and MAGIC (López-Oramas et al. 2021) have led campaigns to search for a VHE component in SGR 1935+2154. Abdalla et al. (2021) observed the source 2 hours prior the CHIME and STARE2 flare and then simultaneously to different X-ray flares. No VHE emission was detected and an UL at $E > 600 \text{ GeV}$ of $2.4 \times 10^{-12} \text{ erg cm}^{-2} \text{ s}^{-1}$ was established. Similarly, the MAGIC multi-wavelength monitoring campaign (López-Oramas et al. 2021) did not find any significant signal, even though some X-ray flares were present during the monitoring campaign. On October 8, CHIME detected three more millisecond events (Good & CHIME/FRB Collaboration 2020) from SGR 1935+2154 (with no X-ray counterpart reported), which were confirmed by FAST on October 9 (Zhu et al. 2020). The radio fluence of these event was lower than that of April 2020. During simultaneous observations by Swift and MAGIC on October 9, a forest of bursts was detected in the hard X-ray range, but no TeV emission was revealed (López-Oramas et al. 2021). The H.E.S.S. and MAGIC observations set constraints to the persistent emission in SGR1935+2154 and to the bursting emission. However, depending on the emission region in the magnetar and the interaction with the surrounding nebula (existing in the case of SGR 1935+2154), future detection of VHE bursts is still plausible.

The new radio facilities that will operate at the time of CTA will provide the detection of up to hundreds of FRB per day. Many of these will have good localizations and will be inside the CTA field of view, making it possible to search for prompt and/or delayed very high-energy emission. Although no magnetar outburst has been yet detected at TeV, the existence of MeV and GeV emission maintains the expectations of a possible TeV component, making magnetars good source candidates for CTA. The CTA Observatory should aim at observing magnetar flares as soon as possible, triggering on external alerts. Automatic re-pointing of the telescopes can take place whenever certain observational criteria (such as i.e. flare type, brightness, multi-wavelength counterparts or distance) are fulfilled. The high sensitivity of CTA at short timescales while provide new insights onto the physics of magnetars at VHE.

5 SYNERGIES WITH LARGE ASTRONOMICAL FACILITIES

Simultaneous coordinated observations with telescopes and facilities at different wavelengths are crucial for understanding the processes and mechanisms at work in the sources of our interest (see Cherenkov Telescope Array Consortium et al. 2019 for a detailed review). Coordination, response to real-time alerts and target-of-opportunity (ToOs) are key in time domain astrophysics when observing transient events. In the case of Galactic transients, external alerts can trigger ToO observations by CTA of new Galactic events or renewed activity of known sources. The trigger criteria is dependent on the type of source observed, with different time urgency and duration varying in terms of the evolution of the specific phenomena. We recommend CTA Observatory to participate in networks (such as the Astrophysical Multi-messenger Observatory Network, AMON⁹ or Simultaneous Multiwavelength Astronomy Research in Transients NETwork, SMARTNet Middleton et al. 2017) to increase the chances of coordination and follow-up in a multi-wavelength and multi-messenger context.

The radio band is of general interest for providing information of the non-thermal processes, and radio facilities are key for locating acceleration sites and shocks. Among other discoveries, the recent association of a magnetar and a FRB has proven that magnetars are the engines of at least some FRBs. FRB-like events triggered in radio will be key to search for (short-timescale) VHE counterparts of, at least, some magnetar engines. For that purpose, CTA will need an external trigger from a radio observatory sensitive to millisecond bursts and capable of issuing prompt alerts. Current generation of telescopes like CHIME, with a large field of view and collecting area, have proven to be excellent detectors for FRB events. Similarly, MeerKat (and future SKA), with its MeerTRAP project to continuously search and detect this type of millisecond-duration events, will provide the needed trigger. Other facilities such ALMA will share important synergies with CTA.

In the optical and infrared domain prompt reaction would be facilitated by coordinating with external observatories within time zones close to those of CTA sites. In the case of CTA North, it should be pursuing synergies mainly with La Palma (and CAHA) telescopes in Spain, while in the CTA South the most appropriate choice would be the different ESO telescopes and other large facilities in Chile, such as the Rubin Observatory Legacy Survey of Space and Time (LSST), which will be key for time-domain astronomy (see Hambleton et al. 2022). The telescope array BlackGEM¹⁰ and the he Gravitational-wave Optical Transient Observer (GOTO)¹¹ will perform optical counterpart identification of gravitational wave events, providing wide field transient discovery in the GW era. In both hemispheres the availability of imaging and spectroscopic instrumentation does largely fulfill the observational needs required for coordinated campaigns. Specific target of opportunity proposals could be eventually placed by the CTA community. In parallel, small optical telescopes either on-site or operated by nearby CTA institutions could also play a key role in this effort if the targets are bright enough as in the case of novae or gamma-ray binaries. This could serve to mitigate the often high time pressure on large telescopes. Additionally, support optical telescopes would ensure a fast follow-up on transients and would provide sufficient coverage in the case of bright sources.

Future space missions will allow to study the X-ray domain with

⁹ <https://www.amon.psu.edu/>

¹⁰ <https://astro.ru.nl/blackgem/>

¹¹ <https://goto-observatory.org/>

improved capabilities. The Space Variable Objects Monitor (SVOM) is expected to be launched in mid 2024 to study GRBs in the 4 - 150 keV range. Although its science is focused in GRB detection, it is likely that it will also detect outbursts or GRB-like events of Galactic origin, i.e., magnetar giant flares. The Advanced Telescope for High-ENergy Astrophysics (Athena) is scheduled for launch in mid 2030s. It will operate in the energy range of 0.2–12 keV. These and other future observatories will be key in Galactic transient detection. As an example, it was seen that changes in the hardness of the X-ray emission of magnetars could be an indicator of an incoming FRB-like event (Mereghetti et al. 2020), which might allow to trigger observations by CTA if confirmed.

The high-energy band ($E > 100$ MeV) is currently explored by the *Fermi*-LAT satellite. Triggers from *Fermi*-LAT have been important for the detection of AGNs and novae in the VHE domain, among others. MeV-GeV information provided with simultaneous observations with *Fermi* is also important to disentangle between hadronic and leptonic processes. If *Fermi* lifetime extends through (at least partially) CTA lifetime, it will provide the needed coverage and alerts to certain observations/triggers. Just recently, the AGILE satellite, that also operated in this energy range, ceased its operations and re-entered the atmosphere (Tavani et al. 2024). For the moment, there is no obvious successor to *Fermi* or AGILE in the same energy domain, although some missions could take over. A successor will be crucial to fully exploit the full potential of gamma-ray astronomy. The High Energy cosmic-Radiation Detection facility (HERD) is expected to be operational from 2026 on board of the Chinese Space Station, detecting gamma rays above 0.5 GeV.

Finally, in a multi-messenger context, CTA will be able to search for the electromagnetic counterpart of GWs generated in the Milky Way, such as white dwarf binary mergers. The Laser Interferometer Space Antenna (LISA) mission will be the first GW observatory on space (scheduled launch on 2030) and will key to study white dwarf mergers (Lamberts et al. 2019; Georgousi et al. 2023). CTA could potentially follow-up transient alerts to search for a putative counterpart. Finally, neutrino alerts will also be crucial in the case some events such as e.g. Galactic core-collapse supernovae.

6 SUMMARY AND CONCLUSIONS

We have studied the capabilities of the forthcoming CTA Observatory to detect transient and variable emission from Galactic sources of different nature. CTA will be able to discover new transients with not significant degradation in the sensitivity, with a maximum of 15% in the crowded inner regions of the Galaxy when overlapping with strong emitters. Similarly, in order to detect variability from dim systems, our simulations have shown that sources with a photon flux $< 1 \times 10^{-13}$ ph cm $^{-2}$ s $^{-1}$ will require > 10 h of observations to detect this variability. For sources with fluxes above this threshold, only 5 – 10 h are required. In the case of strong sources ($\geq 3 \times 10^{-12}$ ph cm $^{-2}$ s $^{-1}$), short exposures 0.5 – 1.0 h are required, implying that low variations in the flux can be detectable from bright sources.

For the case of generic transient sources with the fluxes $< 10^{-13}$ ph cm $^{-2}$ s $^{-1}$ TeV $^{-1}$ CTA will not detect any source in about one hour observation time, while for those with fluxes $< 10^{-9}$ ph cm $^{-2}$ s $^{-1}$ TeV $^{-1}$ in an uncrowded region, CTA will be able to detect $\geq 65\%$ of sources within just 1 hour of observation for both arrays for the different zenith angles and configurations of the geomagnetic field used in this study.

The unique sensitivity at short timescales together with the fast slewing capabilities of the LSTs and the aforementioned capacities

of CTA will allow the detection and discovery of a variety of sources of different nature, according to our simulations:

- (i) CTA will detect VHE from microquasars and from the interaction between their jets and the surrounding environment. Our simulations show that CTA will likely detect both transient and persistent emission from the massive microquasars Cyg X-1 and Cyg X-3. CTA will also significantly detect SS 433, both the interaction regions between the jet and the surrounding nebula and possibly the central source. In the case of LMXBs, CTA will detect outbursts within few tens of minutes from a nearby source (< 4 kpc) with relatively small inclination angle ($< 30^\circ$). Longer exposure times are required for LMXBs with larger angles.
- (ii) We tested the case of tMSPs, concluding that CTA will need long integration times (> 50 h) to be able to detect the possible emission of tMSPs when they are in the LMXB state. These systems could be detected during a transition from RSMP to LMXB if an additional VHE component is present, which could provide crucial information on particle interaction.
- (iii) Flaring emission from the Crab Nebula will be best detected by CTA (or LST sub-array) at low energies ($E < 200$ GeV) in less than 1 h. In the TeV regime, integration times of < 10 h will be needed, specially for the detection of dimmer flares.
- (iv) In the case of novae, CTA will be able to detect close-by novae of both classical and symbiotic nature. As an example of the only VHE novae known to date, our simulations reveal that CTA will detect the symbiotic recurrent nova RS Oph with high significance in only 30 min, allowing for a detailed measurement, and therefore detailed modeling, of its SED from energies as low as 20 GeV. Combined with multi-wavelength observations, the temporal and spectral analyses of CTA observation would improve our understanding of the acceleration processes in novae.

Regarding sources of different nature from the aforementioned, we can expect CTA to detect emission from magnetars during a giant flare and even likely during intermediate flares associated with an FRB. Other possible transient events are flares from SFXTs, for which a detection would definitely identify SFXTs as VHE emitters. Other variable VHE candidates are runaway stars and young stellar objects. Serendipitous discoveries are also likely while performing, i.e., surveys.

Simultaneous multi-wavelength observations will be crucial to maximize the scientific output of the CTA observatory. Synergies with the next generation of astronomical facilities will play a key role both for triggering observations with CTA and to perform follow-ups. In a multi-messenger context, we also expect CTA to be able to follow-up GW events of Galactic origin, with prospects for detecting a TeV counterpart.

ACKNOWLEDGEMENTS

We gratefully acknowledge financial support from the following agencies and organizations:

State Committee of Science of Armenia, Armenia; The Australian Research Council, Astronomy Australia Ltd, The University of Adelaide, Australian National University, Monash University, The University of New South Wales, The University of Sydney, Western Sydney University, Australia; Federal Ministry of Education, Science and Research, and Innsbruck University, Austria; Conselho Nacional de Desenvolvimento Científico e Tecnológico (CNPq), Fundação de Amparo à Pesquisa do Estado do Rio de Janeiro (FAPERJ),

Fundação de Amparo à Pesquisa do Estado de São Paulo (FAPESP), Fundação de Apoio à Ciência, Tecnologia e Inovação do Paraná - Fundação Araucária, Ministry of Science, Technology, Innovations and Communications (MCTIC), Brasil; Ministry of Education and Science, National RI Roadmap Project DOI-153/28.08.2018, Bulgaria; The Natural Sciences and Engineering Research Council of Canada and the Canadian Space Agency, Canada; ANID PIA/APOYO AFB230003, ANID-Chile Basal grant FB 210003, Núcleo Milenio TITANs (NCN19-058), FONDECYT-Chile grants 1201582, 1210131, 1230345, and 1240904; Croatian Science Foundation, Rudjer Boskovic Institute, University of Osijek, University of Rijeka, University of Split, Faculty of Electrical Engineering, Mechanical Engineering and Naval Architecture, University of Zagreb, Faculty of Electrical Engineering and Computing, Croatia; Ministry of Education, Youth and Sports, MEYS LM2018105, LM2023047, EU/MEYS CZ.02.1.01/0.0/0.0/16_013/0001403, CZ.02.1.01/0.0/0.0/18_046/0016007, CZ.02.1.01/0.0/0.0/16_019/0000754 and CZ.02.01.01/00/22_008/0004632, Czech Republic; Academy of Finland (grant nr.317636 and 320045), Finland; Ministry of Higher Education and Research, CNRS-INSU and CNRS-IN2P3, CEA-Irfu, ANR, Regional Council Ile de France, Labex ENIGMASS, OCEVU, OSUG2020 and P2IO, France; The German Ministry for Education and Research (BMBF), the Max Planck Society, the German Research Foundation (DFG, with Collaborative Research Centres 876 & 1491), and the Helmholtz Association, Germany; Department of Atomic Energy, Department of Science and Technology, India; Istituto Nazionale di Astrofisica (INAF), Istituto Nazionale di Fisica Nucleare (INFN), MIUR, Istituto Nazionale di Astrofisica (INAF-OABRERA) Grant Fondazione Cariplo/Regione Lombardia ID 2014-1980/RST_ERC, Italy; ICRR, University of Tokyo, JSPS, MEXT, Japan; Netherlands Research School for Astronomy (NOVA), Netherlands Organization for Scientific Research (NWO), Netherlands; University of Oslo, Norway; Ministry of Science and Higher Education, DIR/WK/2017/12, the National Centre for Research and Development and the National Science Centre, UMO-2016/22/M/ST9/00583, Poland; Slovenian Research Agency, grants P1-0031, P1-0385, I0-0033, J1-9146, J1-1700, N1-0111, and the Young Researcher program, Slovenia; South African Department of Science and Technology and National Research Foundation through the South African Gamma-Ray Astronomy Programme, South Africa; The Spanish groups acknowledge funds from "ERDF A way of making Europe" and the Spanish Ministry of Science and Innovation and the Spanish Research State Agency (AEI) via MCIN/AEI/10.13039/501100011033 through government budget lines PGE2021/28.06.000X.411.01, PGE2022/28.06.000X.411.01, PGE2022/28.06.000X.711.04, and grants PID2022-137810NB-C22, PID2022-136828NB-C42, PID2022-139117NB-C42, PID2022-139117NB-C41, PID2022-136828NB-C41, PID2022-138172NB-C43, PID2022-138172NB-C42, PID2022-139117NB-C44, PID2021-124581OB-I00, PID2021-125331NB-I00, PID2019-104114RB-C31, PID2019-107847RB-C44, PID2019-104114RB-C32, PID2019-105510GB-C31, PID2019-104114RB-C33, PID2019-107847RB-C41, PID2019-107847RB-C43, PID2019-107847RB-C42; the "Centro de Excelencia Severo Ochoa" program through grants no. CEX2019-000920-S, CEX2020-001007-S, CEX2021-001131-S; the "Unidad de Excelencia María de Maeztu" program through grants no. CEX2019-000918-M, CEX2020-001058-M; the "Ramón y Cajal" program through grants RYC2021-032552-I, RYC2021-032991-I, RYC2020-028639-I and RYC-2017-22665; and the "Juan de la Cierva" program through grants no. IJC2019-040315-I and JDC2022-049705-I.

La Caixa Banking Foundation is also acknowledged, grant no. LCF/BQ/PI21/11830030. They also acknowledge the project "Tecnologías avanzadas para la exploración del universo y sus componentes" (PR47/21 TAU), funded by Comunidad de Madrid regional government. Funds were also granted by the Junta de Andalucía regional government under the "Plan Complementario de I+D+I" (Ref. AST22_00001) and "Plan Andaluz de Investigación, Desarrollo e Innovación" (Ref. FQM-322); by the "Programa Operativo de Crecimiento Inteligente" FEDER 2014-2020 (Ref. ESFRI-2017-IAC-12) and Spanish Ministry of Science and Innovation, 15% co-financed by "Consejería de Economía, Industria, Comercio y Conocimiento" of the Gobierno de Canarias regional government. The Generalitat de Catalunya regional government is also gratefully acknowledged via its "CERCA" program and grants 2021SGR00426 and 2021SGR00679. Spanish groups were also kindly supported by European Union funds via the "Horizon 2020" program, grant no. GA:824064, and NextGenerationEU, grants no. PRTR-C17.I1, CT19/23-INVM-109, and "María Zambrano" program, BDNS: 572725. This research used computing and storage resources provided by the Port d'Informació Científica (PIC) data center; Swedish Research Council, Royal Physiographic Society of Lund, Royal Swedish Academy of Sciences, The Swedish National Infrastructure for Computing (SNIC) at Lunarc (Lund), Sweden; State Secretariat for Education, Research and Innovation (SERI) and Swiss National Science Foundation (SNSF), Switzerland; Durham University, Leverhulme Trust, Liverpool University, University of Leicester, University of Oxford, Royal Society, Science and Technology Facilities Council, UK; U.S. National Science Foundation, U.S. Department of Energy, Argonne National Laboratory, Barnard College, University of California, University of Chicago, Columbia University, Georgia Institute of Technology, Institute for Nuclear and Particle Astrophysics (INPAC-MRPI program), Iowa State University, the Smithsonian Institution, V.V.D. is funded by NSF grant AST-1911061, Washington University McDonnell Center for the Space Sciences, The University of Wisconsin and the Wisconsin Alumni Research Foundation, USA.

The research leading to these results has received funding from the European Union's Seventh Framework Programme (FP7/2007-2013) under grant agreements No 262053 and No 317446. This project is receiving funding from the European Union's Horizon 2020 research and innovation programs under agreement No 676134.

ALO acknowledges the programa Ramón y Cajal for which this publication is part through the Project RYC2021-032991-I, funded by MICIU/AEI/10.13039/501100011033, and the European Union "NextGenerationEU"/PRTR. ALO also acknowledges past support from the JSPS Fellowship for Overseas Researchers of the Japan Society for the Promotion of Science. AJR acknowledges support from an ARC fellowship through award number FT170100243. Part of this research was undertaken with the assistance of resources and services from the National Computational Infrastructure (NCI), which is supported by the Australian Government, through the UNSW HPC Resource Allocation Scheme. DdM acknowledges financial support from INAF AstroFund2022 FANS project. AP acknowledges financial support from the National Institute for Astrophysics (INAF) Research Grant "Uncovering the optical beat of the fastest magnetised neutron stars (FANS)" and from the Italian Ministry of University and Research (MUR), PRIN 2020 (prot. 2020BRP57Z) "Gravitational and Electromagnetic-wave Sources in the Universe with current and next-generation detectors (GEMS)".

This research made use of *ctools*, a community-developed

gamma-ray astronomy science analysis software. `ctools` is based on `GammaLib`, a community-developed toolbox for the scientific analysis of astronomical gamma-ray data. This research made use of `gammapy`,¹² a community-developed core Python package for TeV gamma-ray astronomy.

DATA AVAILABILITY

The official CTA observatory IRFs (Maier et al. 2023) used in this manuscript are available in: `prod3b-v2` <https://zenodo.org/record/5163273> and `prod5-v0.1` <https://zenodo.org/record/5499840>. The `ctools` (ascl:1601.005) DOI is: [10.5281/zenodo.4727876](https://doi.org/10.5281/zenodo.4727876). The `gammapy` DOI is [10.5281/zenodo.4701488](https://doi.org/10.5281/zenodo.4701488). The simulations of the Galactic Plane Survey used in Section 2 were retrieved from <https://zenodo.org/doi/10.5281/zenodo.8402519>.

AUTHOR CONTRIBUTIONS

The main individual authors that contributed to this manuscript are, in alphabetical order:

A. Aguasca-Cabot, simulations and drafting of the novae subsection; M. Chernyakova, simulations and drafting of the SS 433 and microquasars subsections; D. Kantzas, simulations and drafting of the LMXBs subsection and modeling of Cygnus X-1 microquasar; A. López-Oramas, coordinator and editor of the manuscript, general drafting; P. L. Luque-Escamilla, drafting of optical and infrared synergies and other expected variable gamma-ray sources at TeV subsections; S. Markoff, simulations and drafting of the LMXBs subsection and modeling of Cygnus X-1 microquasar; J. Martí, drafting of optical and infrared synergies and other expected variable gamma-ray sources at TeV subsections; D. de Martino, internal review of the manuscript; S. McKeague, simulations and drafting of the SS 433 and microquasars subsections; S. Mereghetti, drafting of the magnetar subsection; E. Mestre, simulations and drafting of the Crab Nebula flares subsection; A. Mitchell, simulations and drafting of the novae subsection; E. de Oña-Wilhelmi, simulations and drafting of the Crab Nebula flares and the novae subsections; G. Piano, simulations and drafting of the Cygnus X-3, Cygnus X-1, V404 Cyg and microquasars subsections; P. Romano, early perspectives with CTA, SFXT discussion and internal review of the manuscript; A. J. Ruiter, simulations and drafting of the nova subsection; I. Sadeh, simulations and drafting of the capabilities of CTA for transient detection section; O. Sergijenko, simulations and drafting of the detectability of transients of unknown origin section; L. Sidoli, drafting of the SFXT subsection; A. Spolon, simulations and drafting of the tMSPs subsection; L. Zampieri, simulations of the tMSPs subsection.

AFFILIATIONS

- ¹ Department of Physics, Tokai University, 4-1-1, Kita-Kaname, Hiratsuka, Kanagawa 259-1292, Japan
- ² Institute for Cosmic Ray Research, University of Tokyo, 5-1-5, Kashiwa-no-ha, Kashiwa, Chiba 277-8582, Japan
- ³ ETH Zürich, Institute for Particle Physics and Astrophysics, Otto-Stern-Weg 5, 8093 Zürich, Switzerland

- ⁴ INFN and Università degli Studi di Siena, Dipartimento di Scienze Fisiche, della Terra e dell’Ambiente (DSFTA), Sezione di Fisica, Via Roma 56, 53100 Siena, Italy
- ⁵ Université Paris-Saclay, Université Paris Cité, CEA, CNRS, AIM, F-91191 Gif-sur-Yvette Cedex, France
- ⁶ FSLAC IRL 2009, CNRS/IAC, La Laguna, Tenerife, Spain
- ⁷ University of Alabama, Tuscaloosa, Department of Physics and Astronomy, Gallalee Hall, Box 870324 Tuscaloosa, AL 35487-0324, USA
- ⁸ Université Côte d’Azur, Observatoire de la Côte d’Azur, CNRS, Laboratoire Lagrange, France
- ⁹ Laboratoire Leprince-Ringuet, CNRS/IN2P3, École polytechnique, Institut Polytechnique de Paris, 91120 Palaiseau, France
- ¹⁰ Departament de Física Quàntica i Astrofísica, Institut de Ciències del Cosmos, Universitat de Barcelona, IEEC-UB, Martí i Franquès, 1, 08028, Barcelona, Spain
- ¹¹ Instituto de Astrofísica de Andalucía-CSIC, Glorieta de la Astronomía s/n, 18008, Granada, Spain
- ¹² Institute for Computational Cosmology and Department of Physics, Durham University, South Road, Durham DH1 3LE, United Kingdom
- ¹³ Pontificia Universidad Católica de Chile, Av. Libertador Bernardo O’Higgins 340, Santiago, Chile
- ¹⁴ Universidad Nacional Autónoma de México, Delegación Coyoacán, 04510 Ciudad de México, Mexico
- ¹⁵ IPARCOS-UCM, Instituto de Física de Partículas y del Cosmos, and EMFTel Department, Universidad Complutense de Madrid, E-28040 Madrid, Spain
- ¹⁶ Instituto de Física Teórica UAM/CSIC and Departamento de Física Teórica, Universidad Autónoma de Madrid, c/ Nicolás Cabrera 13-15, Campus de Cantoblanco UAM, 28049 Madrid, Spain
- ¹⁷ LUTH, GEPI and LERMA, Observatoire de Paris, Université PSL, Université Paris Cité, CNRS, 5 place Jules Janssen, 92190, Meudon, France
- ¹⁸ INFN - Osservatorio Astrofisico di Arcetri, Largo E. Fermi, 5 - 50125 Firenze, Italy
- ¹⁹ INFN Sezione di Perugia and Università degli Studi di Perugia, Via A. Pascoli, 06123 Perugia, Italy
- ²⁰ INFN - Osservatorio Astronomico di Roma, Via di Frascati 33, 00078, Monteporzio Catone, Italy
- ²¹ TÜBİTAK Research Institute for Fundamental Sciences, 41470 Gebze, Kocaeli, Turkey
- ²² INFN Sezione di Napoli, Via Cintia, ed. G, 80126 Napoli, Italy
- ²³ INFN Sezione di Padova, Via Marzolo 8, 35131 Padova, Italy
- ²⁴ Instituto de Astrofísica de Canarias and Departamento de Astrofísica, Universidad de La Laguna, La Laguna, Tenerife, Spain
- ²⁵ Kapteyn Astronomical Institute, University of Groningen, Landleven 12, 9747 AD, Groningen, The Netherlands
- ²⁶ Instituto de Física de São Carlos, Universidade de São Paulo, Av. Trabalhador São-carlense, 400 - CEP 13566-590, São Carlos, SP, Brazil
- ²⁷ Astroparticle Physics, Department of Physics, TU Dortmund University, Otto-Hahn-Str. 4a, 44227 Dortmund, Germany
- ²⁸ Department of Physics, Chemistry & Material Science, University of Namibia, Private Bag 13301, Windhoek, Namibia
- ²⁹ Centre for Space Research, North-West University, Potchefstroom, 2520, South Africa
- ³⁰ School of Physics and Astronomy, Monash University, Melbourne, Victoria 3800, Australia
- ³¹ Département de physique nucléaire et corpusculaire, University of Genève, Faculté de Sciences, 1205 Genève, Switzerland

¹² <https://www.gammapy.org>

- ³² Faculty of Science and Technology, Universidad del Azuay, Cuenca, Ecuador.
- ³³ Deutsches Elektronen-Synchrotron, Platanenallee 6, 15738 Zeuthen, Germany
- ³⁴ Centro Brasileiro de Pesquisas Físicas, Rua Xavier Sigaud 150, RJ 22290-180, Rio de Janeiro, Brazil
- ³⁵ Instituto de Astronomia, Geofísica e Ciências Atmosféricas - Universidade de São Paulo, Cidade Universitária, R. do Matão, 1226, CEP 05508-090, São Paulo, SP, Brazil
- ³⁶ INFN Sezione di Padova and Università degli Studi di Padova, Via Marzolo 8, 35131 Padova, Italy
- ³⁷ Institut für Physik & Astronomie, Universität Potsdam, Karl-Liebknecht-Strasse 24/25, 14476 Potsdam, Germany
- ³⁸ Institut für Theoretische Physik, Lehrstuhl IV: Plasma-Astroteilchenphysik, Ruhr-Universität Bochum, Universitätsstraße 150, 44801 Bochum, Germany
- ³⁹ Université Paris Cité, Université Paris-Saclay, CEA, CNRS, AIM, F-91191 Gif-sur-Yvette, France
- ⁴⁰ Center for Astrophysics | Harvard & Smithsonian, 60 Garden St, Cambridge, MA 02138, USA
- ⁴¹ CIEMAT, Avda. Complutense 40, 28040 Madrid, Spain
- ⁴² Max-Planck-Institut für Kernphysik, Saupfercheckweg 1, 69117 Heidelberg, Germany
- ⁴³ Max-Planck-Institut für Physik, Boltzmannstr. 8, 85748 Garching, Germany
- ⁴⁴ Pidstryhach Institute for Applied Problems in Mechanics and Mathematics NASU, 3B Naukova Street, Lviv, 79060, Ukraine
- ⁴⁵ Univ. Savoie Mont Blanc, CNRS, Laboratoire d'Annecy de Physique des Particules - IN2P3, 74000 Annecy, France
- ⁴⁶ Center for Astrophysics and Cosmology (CAC), University of Nova Gorica, Nova Gorica, Slovenia
- ⁴⁷ Politecnico di Bari, via Orabona 4, 70124 Bari, Italy
- ⁴⁸ INFN Sezione di Bari, via Orabona 4, 70126 Bari, Italy
- ⁴⁹ Institut de Física d'Altes Energies (IFAE), The Barcelona Institute of Science and Technology, Campus UAB, 08193 Bellaterra (Barcelona), Spain
- ⁵⁰ FZU - Institute of Physics of the Czech Academy of Sciences, Na Slovance 1999/2, 182 00 Praha 8, Czech Republic
- ⁵¹ INAF - Osservatorio Astronomico di Palermo "G.S. Vaiana", Piazza del Parlamento 1, 90134 Palermo, Italy
- ⁵² Sorbonne Université, CNRS/IN2P3, Laboratoire de Physique Nucléaire et de Hautes Energies, LPNHE, 4 place Jussieu, 75005 Paris, France
- ⁵³ INAF - Osservatorio Astronomico di Brera, Via Brera 28, 20121 Milano, Italy
- ⁵⁴ INFN Sezione di Pisa, Edificio C – Polo Fibonacci, Largo Bruno Pontecorvo 3, 56127 Pisa
- ⁵⁵ University School for Advanced Studies IUSS Pavia, Palazzo del Broletto, Piazza della Vittoria 15, 27100 Pavia, Italy
- ⁵⁶ Università degli Studi di Trento, Via Calepina, 14, 38122 Trento, Italy
- ⁵⁷ University of Zagreb, Faculty of electrical engineering and computing, Unska 3, 10000 Zagreb, Croatia
- ⁵⁸ IRFU, CEA, Université Paris-Saclay, Bât 141, 91191 Gif-sur-Yvette, France
- ⁵⁹ INAF - Osservatorio di Astrofisica e Scienza dello spazio di Bologna, Via Piero Gobetti 93/3, 40129 Bologna, Italy
- ⁶⁰ Centre for Advanced Instrumentation, Department of Physics, Durham University, South Road, Durham, DH1 3LE, United Kingdom
- ⁶¹ INFN Sezione di Trieste and Università degli Studi di Udine, Via delle Scienze 208, 33100 Udine, Italy
- ⁶² Dublin Institute for Advanced Studies, 31 Fitzwilliam Place, Dublin 2, Ireland
- ⁶³ Armagh Observatory and Planetarium, College Hill, Armagh BT61 9DB, United Kingdom
- ⁶⁴ School of Physics, University of New South Wales, Sydney NSW 2052, Australia
- ⁶⁵ INFN Sezione di Catania, Via S. Sofia 64, 95123 Catania, Italy
- ⁶⁶ Unitat de Física de les Radiacions, Departament de Física, and CERES-IEEC, Universitat Autònoma de Barcelona, Edifici C3, Campus UAB, 08193 Bellaterra, Spain
- ⁶⁷ Department of Physics, Faculty of Science, Kasetsart University, 50 Ngam Wong Wan Rd., Lat Yao, Chatuchak, Bangkok, 10900, Thailand
- ⁶⁸ National Astronomical Research Institute of Thailand, 191 Huay Kaew Rd., Suthep, Muang, Chiang Mai, 50200, Thailand
- ⁶⁹ INAF - Osservatorio Astronomico di Capodimonte, Via Salita Moiarillo 16, 80131 Napoli, Italy
- ⁷⁰ Universidade Cidade de São Paulo, Núcleo de Astrofísica, R. Galvão Bueno 868, Liberdade, São Paulo, SP, 01506-000, Brazil
- ⁷¹ Dep. of Physics, Sapienza, University of Roma, Piazzale A. Moro 5, 00185, Roma, Italy
- ⁷² INAF - Istituto di Astrofisica Spaziale e Fisica Cosmica di Milano, Via A. Corti 12, 20133 Milano, Italy
- ⁷³ CCTVal, Universidad Técnica Federico Santa María, Avenida España 1680, Valparaíso, Chile
- ⁷⁴ Aix Marseille Univ, CNRS/IN2P3, CPPM, Marseille, France
- ⁷⁵ Universidad de Alcalá - Space & Astroparticle group, Facultad de Ciencias, Campus Universitario Ctra. Madrid-Barcelona, Km. 33.600 28871 Alcalá de Henares (Madrid), Spain
- ⁷⁶ INFN Sezione di Bari and Università degli Studi di Bari, via Orabona 4, 70124 Bari, Italy
- ⁷⁷ Université Paris Cité, CNRS, Astroparticule et Cosmologie, F-75013 Paris, France
- ⁷⁸ University of the Witwatersrand, 1 Jan Smuts Avenue, Braamfontein, 2000 Johannesburg, South Africa
- ⁷⁹ Dublin City University, Glasnevin, Dublin 9, Ireland
- ⁸⁰ INFN Sezione di Torino, Via P. Giuria 1, 10125 Torino, Italy
- ⁸¹ Dipartimento di Fisica - Università degli Studi di Torino, Via Pietro Giuria 1 - 10125 Torino, Italy
- ⁸² Dipartimento di Fisica e Chimica "E. Segrè", Università degli Studi di Palermo, Via Archirafi 36, 90123, Palermo, Italy
- ⁸³ Universidade Federal Do Paraná - Setor Palotina, Departamento de Engenharias e Exatas, Rua Pioneiro, 2153, Jardim Dallas, CEP: 85950-000 Palotina, Paraná, Brazil
- ⁸⁴ INAF - Osservatorio Astrofisico di Catania, Via S. Sofia, 78, 95123 Catania, Italy
- ⁸⁵ University of Oxford, Department of Physics, Clarendon Laboratory, Parks Road, Oxford, OX1 3PU, United Kingdom
- ⁸⁶ Universidad de Valparaíso, Blanco 951, Valparaíso, Chile
- ⁸⁷ University of Wisconsin, Madison, 500 Lincoln Drive, Madison, WI, 53706, USA
- ⁸⁸ INAF - Istituto di Astrofisica Spaziale e Fisica Cosmica di Palermo, Via U. La Malfa 153, 90146 Palermo, Italy
- ⁸⁹ Department of Physics and Technology, University of Bergen, Museplass 1, 5007 Bergen, Norway
- ⁹⁰ INAF - Istituto di Radioastronomia, Via Gobetti 101, 40129 Bologna, Italy
- ⁹¹ Western Sydney University, Locked Bag 1797, Penrith, NSW 2751, Australia
- ⁹² INAF - Istituto Nazionale di Astrofisica, Viale del Parco Mellini 84, 00136 Rome, Italy
- ⁹³ Laboratoire Univers et Particules de Montpellier, Université de

- Montpellier, CNRS/IN2P3, CC 72, Place Eugène Bataillon, F-34095 Montpellier Cedex 5, France
- ⁹⁴ Università degli Studi di Napoli “Federico II” - Dipartimento di Fisica “E. Pancini”, Complesso Universitario di Monte Sant’Angelo, Via Cintia - 80126 Napoli, Italy
- ⁹⁵ Università degli Studi di Modena e Reggio Emilia, Dipartimento di Ingegneria “Enzo Ferrari”, via Pietro Vivarelli 10, 41125, Modena, Italy
- ⁹⁶ Institut für Astronomie und Astrophysik, Universität Tübingen, Sand 1, 72076 Tübingen, Germany
- ⁹⁷ University of Rijeka, Faculty of Physics, Radmile Matejčić 2, 51000 Rijeka, Croatia
- ⁹⁸ Institute for Theoretical Physics and Astrophysics, Universität Würzburg, Campus Hubland Nord, Emil-Fischer-Str. 31, 97074 Würzburg, Germany
- ⁹⁹ Université Paris-Saclay, CNRS/IN2P3, IJCLab, 91405 Orsay, France
- ¹⁰⁰ Department of Astronomy and Astrophysics, University of Chicago, 5640 S Ellis Ave, Chicago, Illinois, 60637, USA
- ¹⁰¹ LAPTh, CNRS, USMB, F-74940 Annecy, France
- ¹⁰² School of Physics, Chemistry and Earth Sciences, University of Adelaide, Adelaide SA 5005, Australia
- ¹⁰³ Department of Physics, Washington University, St. Louis, MO 63130, USA
- ¹⁰⁴ Escuela de Ingeniería Eléctrica, Facultad de Ingeniería, Pontificia Universidad Católica de Valparaíso, Avenida Brasil 2147, Valparaíso, Chile
- ¹⁰⁵ Santa Cruz Institute for Particle Physics and Department of Physics, University of California, Santa Cruz, 1156 High Street, Santa Cruz, CA 95064, USA
- ¹⁰⁶ Escola de Artes, Ciências e Humanidades, Universidade de São Paulo, Rua Arlindo Bettio, CEP 03828-000, 1000 São Paulo, Brazil
- ¹⁰⁷ Department of Physics and Astronomy, University of Utah, Salt Lake City, UT 84112-0830, USA
- ¹⁰⁸ The University of Manitoba, Dept of Physics and Astronomy, Winnipeg, Manitoba R3T 2N2, Canada
- ¹⁰⁹ RIKEN, Institute of Physical and Chemical Research, 2-1 Hirosawa, Wako, Saitama, 351-0198, Japan
- ¹¹⁰ INFN Sezione di Roma La Sapienza, P.le Aldo Moro, 2 - 00185 Roma, Italy
- ¹¹¹ INAF - Osservatorio Astronomico di Padova, Vicolo dell’Osservatorio 5, 35122 Padova, Italy
- ¹¹² INAF - Istituto di Astrofisica e Planetologia Spaziali (IAPS), Via del Fosso del Cavaliere 100, 00133 Roma, Italy
- ¹¹³ Ruhr University Bochum, Faculty of Physics and Astronomy, Astronomical Institute (AIRUB), Universitätsstraße 150, 44801 Bochum, Germany
- ¹¹⁴ Physics Program, Graduate School of Advanced Science and Engineering, Hiroshima University, 739-8526 Hiroshima, Japan
- ¹¹⁵ Department of Physics, Nagoya University, Chikusa-ku, Nagoya, 464-8602, Japan
- ¹¹⁶ Friedrich-Alexander-Universität Erlangen-Nürnberg, Erlangen Centre for Astroparticle Physics, Nikolaus-Fiebiger-Str. 2, 91058 Erlangen, Germany
- ¹¹⁷ Department of Information Technology, Escuela Politécnica Superior, Universidad San Pablo-CEU, CEU Universities, Campus Montepríncipe, Boadilla del Monte, Madrid 28668, Spain
- ¹¹⁸ INFN Sezione di Roma Tor Vergata, Via della Ricerca Scientifica 1, 00133 Rome, Italy
- ¹¹⁹ Alikhanyan National Science Laboratory, Yerevan Physics Institute, 2 Alikhanyan Brothers St., 0036, Yerevan, Armenia
- ¹²⁰ Université Paris Cité, CNRS, CEA, Astroparticule et Cosmologie, F-75013 Paris, France
- ¹²¹ Universidad Andrés Bello, Av. Fernández Concha 700, Las Condes, Santiago, Chile
- ¹²² Núcleo de Astrofísica e Cosmologia (Cosmo-ufes) & Departamento de Física, Universidade Federal do Espírito Santo (UFES), Av. Fernando Ferrari, 514. 29065-910. Vitória-ES, Brazil
- ¹²³ Astrophysics Research Center of the Open University (ARCO), The Open University of Israel, P.O. Box 808, Ra’anana 4353701, Israel
- ¹²⁴ Department of Physics, The George Washington University, Washington, DC 20052, USA
- ¹²⁵ University of Liverpool, Oliver Lodge Laboratory, Liverpool L69 7ZE, United Kingdom
- ¹²⁶ King’s College London, Strand, London, WC2R 2LS, United Kingdom
- ¹²⁷ Cherenkov Telescope Array Observatory gGmbH, Via Gobetti, Bologna, Italy
- ¹²⁸ General Education Center, Yamanashi-Gakuin University, Kofu, Yamanashi 400-8575, Japan
- ¹²⁹ Sendai College, National Institute of Technology, Natori, Miyagi 981-1239, Japan
- ¹³⁰ Universität Innsbruck, Institut für Astro- und Teilchenphysik, Technikerstr. 25/8, 6020 Innsbruck, Austria
- ¹³¹ Department of Physics, Faculty of Engineering Science, Yokohama National University, Yokohama 240–8501, Japan
- ¹³² Astronomical Observatory of Taras Shevchenko National University of Kyiv, 3 Observatorna Street, Kyiv, 04053, Ukraine
- ¹³³ Palacký University Olomouc, Faculty of Science, Joint Laboratory of Optics of Palacký University and Institute of Physics of the Czech Academy of Sciences, 17. listopadu 1192/12, 779 00 Olomouc, Czech Republic
- ¹³⁴ Finnish Centre for Astronomy with ESO, University of Turku, Finland, FI-20014 University of Turku, Finland
- ¹³⁵ Aalto University, Metsähovi Radio Observatory, Metsähovintie 114, FI-02540 Kylmäla, Finland
- ¹³⁶ Josip Juraj Strossmayer University of Osijek, Trg Ljudevita Gaja 6, 31000 Osijek, Croatia
- ¹³⁷ CETEMPS Dipartimento di Scienze Fisiche e Chimiche, Università degli Studi dell’Aquila and GSGC-LNGS-INFN, Via Vetoio 1, L’Aquila, 67100, Italy
- ¹³⁸ Chiba University, 1-33, Yayoicho, Inage-ku, Chiba-shi, Chiba, 263-8522 Japan
- ¹³⁹ Department of Earth and Space Science, Graduate School of Science, Osaka University, Toyonaka 560-0043, Japan
- ¹⁴⁰ Astronomical Observatory, Jagiellonian University, ul. Orła 171, 30-244 Cracow, Poland
- ¹⁴¹ Landessternwarte, Zentrum für Astronomie der Universität Heidelberg, Königstuhl 12, 69117 Heidelberg, Germany
- ¹⁴² IRAP, Université de Toulouse, CNRS, CNES, UPS, 9 avenue Colonel Roche, 31028 Toulouse, Cedex 4, France
- ¹⁴³ Department of Physics and Astronomy, University of California, Los Angeles, CA 90095, USA
- ¹⁴⁴ Astronomical Institute of the Czech Academy of Sciences, Bocni II 1401 - 14100 Prague, Czech Republic
- ¹⁴⁵ Faculty of Science, Ibaraki University, Mito, Ibaraki, 310-8512, Japan
- ¹⁴⁶ Faculty of Science and Engineering, Waseda University, Shinjuku, Tokyo 169-8555, Japan
- ¹⁴⁷ University of Oslo, Department of Physics, Sem Saelandsvei 24 - PO Box 1048 Blindern, N-0316 Oslo, Norway

- 148 Nicolaus Copernicus Astronomical Center, Polish Academy of Sciences, ul. Bartycka 18, 00-716 Warsaw, Poland
- 149 National Astronomical Observatory of Japan (NAOJ), Division of Science, 2-21-1, Osawa, Mitaka, Tokyo 181-8588, Japan
- 150 Institute of Particle and Nuclear Studies, KEK (High Energy Accelerator Research Organization), 1-1 Oho, Tsukuba, 305-0801, Japan
- 151 School of Physics and Astronomy, University of Leicester, Leicester, LE1 7RH, United Kingdom
- 152 Université Bordeaux, CNRS, LP2I Bordeaux, UMR 5797, 19 Chemin du Solarium, F-33170 Gradignan, France
- 153 Università degli studi di Catania, Dipartimento di Fisica e Astronomia “Ettore Majorana”, Via S. Sofia 64, 95123 Catania, Italy
- 154 Department of Physics and Astronomy, University of Turku, Finland, FI-20014 University of Turku, Finland
- 155 ASI - Space Science Data Center, Via del Politecnico s.n.c., 00133, Rome, Italy
- 156 INFN Sezione di Trieste and Università degli Studi di Trieste, Via Valerio 2 I, 34127 Trieste, Italy
- 157 Escuela Politécnica Superior de Jaén, Universidad de Jaén, Campus Las Lagunillas s/n, Edif. A3, 23071 Jaén, Spain
- 158 Department of Astronomy, University of Geneva, Chemin d’Ecogia 16, CH-1290 Versoix, Switzerland
- 159 Anton Pannekoek Institute/GRAPPA, University of Amsterdam, Science Park 904 1098 XH Amsterdam, The Netherlands
- 160 Saha Institute of Nuclear Physics, A CI of Homi Bhabha National Institute, Kolkata 700064, West Bengal, India
- 161 Institute for Nuclear Research and Nuclear Energy, Bulgarian Academy of Sciences, 72 boul. Tsarigradsko chaussee, 1784 Sofia, Bulgaria
- 162 Kavli Institute for Particle Astrophysics and Cosmology, Stanford University, Stanford, CA 94305, USA
- 163 UCM-ELEC group, EMFTEL Department, University Complutense of Madrid, 28040 Madrid, Spain
- 164 Departamento de Ingeniería Eléctrica, Universidad Pontificia Comillas - ICAI, 28015 Madrid
- 165 Institute of Space Sciences (ICE, CSIC), and Institut d’Estudis Espacials de Catalunya (IEEC), and Institució Catalana de Recerca i Estudis Avançats (ICREA), Campus UAB, Carrer de Can Magrans, s/n 08193 Cerdanyola del Vallés, Spain
- 166 The Henryk Niewodniczański Institute of Nuclear Physics, Polish Academy of Sciences, ul. Radzikowskiego 152, 31-342 Cracow, Poland
- 167 IPARCOS Institute, Faculty of Physics (UCM), 28040 Madrid, Spain
- 168 Department of Physics, Konan University, Kobe, Hyogo, 658-8501, Japan
- 169 Hiroshima Astrophysical Science Center, Hiroshima University, Higashi-Hiroshima, Hiroshima 739-8526, Japan
- 170 Joseph-von-Fraunhofer-Str. 25, 44227 Dortmund, Germany
- 171 School of Allied Health Sciences, Kitasato University, Sagami-hara, Kanagawa 228-8555, Japan
- 172 Department of Physics, Yamagata University, Yamagata, Yamagata 990-8560, Japan
- 173 Departamento de Física, Universidade Federal do Rio Grande do Norte, 59078-970, Natal, RN, Brasil
- 174 International Institute of Physics, Universidade Federal do Rio Grande do Norte, 59078-970, Natal, RN, Brasil
- 175 University of Białystok, Faculty of Physics, ul. K. Ciołkowskiego 1L, 15-245 Białystok, Poland
- 176 Charles University, Institute of Particle & Nuclear Physics, V Holešovičkách 2, 180 00 Prague 8, Czech Republic
- 177 Institute for Space—Earth Environmental Research, Nagoya University, Furo-cho, Chikusa-ku, Nagoya 464-8601, Japan
- 178 Kobayashi—Maskawa Institute for the Origin of Particles and the Universe, Nagoya University, Furo-cho, Chikusa-ku, Nagoya 464-8602, Japan
- 179 Graduate School of Technology, Industrial and Social Sciences, Tokushima University, Tokushima 770-8506, Japan
- 180 Cherenkov Telescope Array Observatory, Saupfercheckweg 1, 69117 Heidelberg, Germany
- 181 University of Pisa, Largo B. Pontecorvo 3, 56127 Pisa, Italy
- 182 Rudjer Boskovic Institute, Bijenicka 54, 10 000 Zagreb, Croatia
- 183 INFN - Osservatorio Astronomico di Padova and INFN Sezione di Trieste, gr. coll. Udine, Via delle Scienze 208 I-33100 Udine, Italy
- 184 Univ. Grenoble Alpes, CNRS, IPAG, 38000 Grenoble, France
- 185 Dipartimento di Scienze Fisiche e Chimiche, Università degli Studi dell’Aquila and GSGC-LNGS-INFN, Via Vetoio 1, L’Aquila, 67100, Italy
- 186 Centre for Astro-Particle Physics (CAPP) and Department of Physics, University of Johannesburg, PO Box 524, Auckland Park 2006, South Africa
- 187 Departamento de Física, Facultad de Ciencias Básicas, Universidad Metropolitana de Ciencias de la Educación, Avenida José Pedro Alessandri 774, Ñuñoa, Santiago, Chile
- 188 School of Physics and Astronomy, University of Minnesota, 116 Church Street S.E. Minneapolis, Minnesota 55455-0112, USA
- 189 Instituto de Estudios Astrofísicos, Facultad de Ingeniería y Ciencias, Universidad Diego Portales, Av. Ejército Libertador 441, 8370191 Santiago, Chile
- 190 Departamento de Astronomía, Universidad de Concepción, Barrio Universitario S/N, Concepción, Chile
- 191 Instituto de Física - Universidade de São Paulo, Rua do Matão Travessa R Nr.187 CEP 05508-090 Cidade Universitária, São Paulo, Brazil
- 192 University of New South Wales, School of Science, Australian Defence Force Academy, Canberra, ACT 2600, Australia
- 193 Gifu University, Faculty of Engineering, 1-1 Yanagido, Gifu 501-1193, Japan
- 194 University of Split - FESB, R. Boskovicica 32, 21 000 Split, Croatia
- 195 Departamento de Física, Universidad de Santiago de Chile (US-ACH), Av. Victor Jara 3493, Estación Central, Santiago, Chile
- 196 Main Astronomical Observatory of the National Academy of Sciences of Ukraine, Zabolotnoho str., 27, 03143, Kyiv, Ukraine
- 197 Space Technology Centre, AGH University of Krakow, Aleja Mickiewicza 30, Kraków 30-059, Poland
- 198 Academic Computer Centre CYFRONET AGH, ul. Nawojki 11, 30-950, Kraków, Poland
- 199 Institute of Astronomy, Faculty of Physics, Astronomy and Informatics, Nicolaus Copernicus University in Toruń, ul. Grudziądzka 5, 87-100 Toruń, Poland
- 200 Warsaw University of Technology, Faculty of Electronics and Information Technology, Institute of Electronic Systems, Nowowiejska 15/19, 00-665 Warsaw, Poland
- 201 Department of Physical Sciences, Aoyama Gakuin University, Fuchinobe, Sagami-hara, Kanagawa, 252-5258, Japan
- 202 Division of Physics and Astronomy, Graduate School of Science, Kyoto University, Sakyo-ku, Kyoto, 606-8502, Japan
- 203 INFN - Osservatorio Astronomico di Cagliari, Via della Scienza 5, I-09047 Selargius (CA), Italy

- ²⁰⁴ INAF - Osservatorio Astrofisico di Torino, Strada Osservatorio 20, 10025 Pino Torinese (TO), Italy
- ²⁰⁵ Departamento de Física, Universidad Técnica Federico Santa María, Avenida España, 1680 Valparaíso, Chile
- ²⁰⁶ School of Physics and Astronomy, Sun Yat-sen University, Zhuhai, China

REFERENCES

- Abdalla H., et al., 2019, *Nature*, **575**, 464
- Abdalla H., et al., 2021, *ApJ*, **919**, 106
- Abdo A. A., et al., 2010a, *Science*, **329**, 817
- Abdo A. A., et al., 2010b, *ApJ*, **725**, L73
- Abdo A. A., et al., 2011, *Science*, **331**, 739
- Abdollahi S., et al., 2020, *ApJS*, **247**, 33
- Abe H., et al., 2022, *MNRAS*, **517**, 4736
- Abe H., et al., 2023, *PoS, Gamma2022*, 055
- Abeyssekara A. U., et al., 2017, *Science*, **358**, 911
- Abeyssekara A. U., et al., 2018a, *Nature*, **562**, 82
- Abeyssekara A. U., et al., 2018b, *ApJ*, **861**, 134
- Abeyssekara A. U., et al., 2018c, *ApJ*, **867**, L19
- Acciari V. A., et al., 2022, *Nature Astronomy*, **6**, 689
- Ackermann M., et al., 2014, *Science*, **345**, 554
- Ackermann M., et al., 2017, *ApJ*, **843**, 139
- Aguasca-Cabot A., et al., 2023, Gammapy: Python toolbox for gamma-ray astronomy, <https://zenodo.org/records/8033275>
- Ahnen M. L., et al., 2015, *A&A*, **582**, A67
- Ahnen M. L., et al., 2017a, *MNRAS*, **471**, 1688
- Ahnen M. L., et al., 2017b, *MNRAS*, **472**, 3474
- Albert J., et al., 2007, *ApJ*, **665**, L51
- Aleksić J., et al., 2010, *ApJ*, **721**, 843
- Aleksić J., et al., 2011, *ApJ*, **735**, L5
- Aleksić J., et al., 2013, *A&A*, **549**, A23
- Aliu E., et al., 2012, *ApJ*, **754**, 77
- Aliu E., et al., 2014a, *ApJ*, **781**, L11
- Aliu E., et al., 2014b, *ApJ*, **788**, 78
- Aliu E., et al., 2016, *ApJ*, **831**, 193
- Ansoldi S., et al., 2016, *A&A*, **585**, A133
- Antokhin I. I., Cherepashchuk A. M., Antokhina E. A., Tatarnikov A. M., 2022, *ApJ*, **926**, 123
- Anupama G. C., Mikołajewska J., 1999, *A&A*, **344**, 177
- Arakawa M., Hayashida M., Khangulyan D., Uchiyama Y., 2020, *ApJ*, **897**, 33
- Araudo A. T., Padovani M., Marcowith A., 2021, *MNRAS*, **504**, 2405
- Araya M., HAWC Collaboration 2019, in 36th International Cosmic Ray Conference (ICRC2019). p. 619 ([arXiv:1907.10197](https://arxiv.org/abs/1907.10197))
- Archibald A. M., et al., 2009a, *Science*, **324**, 1411
- Archibald A. M., et al., 2009b, *Science*, **324**, 1411
- Barry R., Mukai K., Sokoloski J., Danchi W., Hachisu I., Evans A., Gehrz R., Mikołajewska J., 2008, in RS Ophiuchi (2006) and the Recurrent Nova Phenomenon. p. 52
- Bassa C. G., et al., 2014, *MNRAS*, **441**, 1825
- Bell A. R., 2004, *MNRAS*, **353**, 550
- Bochenek C. D., Ravi V., Belov K. V., Hallinan G., Kocz J., Kulkarni S. R., McKenna D. L., 2020, *Nature*, **587**, 59
- Bode M. F., Kahn F. D., 1985, *MNRAS*, **217**, 205
- Bogdanov S., et al., 2015, *ApJ*, **806**, 148
- Bond H. E., White R. L., Becker R. H., O'Brien M. S., 2002, *PASP*, **114**, 1359
- Bordas P., Yang R., Kafexhiu E., Aharonian F., 2015, *ApJ*, **807**, L8
- Brinkmann W., Pratt G. W., Rohr S., Kawai N., Burwitz V., 2007, *A&A*, **463**, 611
- Buehler R., et al., 2012, *ApJ*, **749**, 26
- Bulgarelli A., et al., 2010, The Astronomer's Telegram, **2512**, 1
- CHIME/FRB Collaboration et al., 2020, *Nature*, **587**, 54
- CTA Consortium 2023, [arXiv e-prints](https://arxiv.org/abs/2310.02828), p. [arXiv:2310.02828](https://arxiv.org/abs/2310.02828)
- CTA-LST Project et al., 2023, [arXiv e-prints](https://arxiv.org/abs/2306.12960), p. [arXiv:2306.12960](https://arxiv.org/abs/2306.12960)
- Cangemi F., et al., 2021, *A&A*, **650**, A93
- Cao Z., et al., 2021, *Nature*, **594**, 33
- Cao Z., et al., 2023a, [arXiv e-prints](https://arxiv.org/abs/2305.17030), p. [arXiv:2305.17030](https://arxiv.org/abs/2305.17030)
- Cao Z., et al., 2023b, [arXiv e-prints](https://arxiv.org/abs/2305.17030), p. [arXiv:2305.17030](https://arxiv.org/abs/2305.17030)
- Casares J., Charles P. A., Naylor T., 1992, *Nature*, **355**, 614
- Chaty S., 2022, Accreting Binaries; Nature, formation, and evolution, [doi:10.1088/2514-3433/ac595f](https://doi.org/10.1088/2514-3433/ac595f).
- Cherenkov Telescope Array Consortium et al., 2019, Science with the Cherenkov Telescope Array, [doi:10.1142/10986](https://doi.org/10.1142/10986).
- Cheung C. C., et al., 2022, *ApJ*, **935**, 44
- Chomiuk L., Metzger B. D., Shen K. J., 2021, *ARA&A*, **59**, 391
- Coppi P. S., 1999, The Physics of Hybrid Thermal/Non-Thermal Plasmas. p. 375
- Corral-Santana J. M., Casares J., Muñoz-Darias T., Bauer F. E., Martínez-Pais I. G., Russell D. M., 2016, *A&A*, **587**, A61
- Davidson K., Fesen R. A., 1985, *ARA&A*, **23**, 119
- De K., et al., 2021, *ApJ*, **912**, 19
- Donath A., et al., 2023, *A&A*, **678**, A157
- Dubus G., Cerutti B., Henri G., 2010, *MNRAS*, **404**, L55
- Duncan R. C., Thompson C., 1992, *ApJ*, **392**, L9
- Fabrika S., 2004, Astrophysics and Space Physics Reviews, **12**, 1
- Falcke H., Körding E., Markoff S., 2004, *A&A*, **414**, 895
- Fermi LAT Collaboration et al., 2009, *Science*, **326**, 1512
- Fermi-LAT Collaboration et al., 2021, *Nature Astronomy*,
- Fioretti V., Ribeiro D., Humensky T. B., Bulgarelli A., Maier G., Moralejo A., Nigro C., 2019, in 36th International Cosmic Ray Conference (ICRC2019). p. 673 ([arXiv:1907.08018](https://arxiv.org/abs/1907.08018)), [doi:10.22323/1.358.0673](https://doi.org/10.22323/1.358.0673)
- Franckowiak A., Jean P., Wood M., Cheung C. C., Buson S., 2018, *A&A*, **609**, A120
- Frederiks D. D., Palshin V. D., Aptekar R. L., Golenetskii S. V., Cline T. L., Mazets E. P., 2007, *Astronomy Letters*, **33**, 19
- Funk S., Hinton J. A., CTA Consortium 2013, *Astroparticle Physics*, **43**, 348
- Gaia Collaboration 2020, VizieR Online Data Catalog, p. I/350
- Gallagher J. S., Starrfield S., 1978, *ARA&A*, **16**, 171
- Gallo E., Plotkin R. M., Jonker P. G., 2014, *MNRAS*, **438**, L41
- Gavriil F. P., Gonzalez M. E., Gotthelf E. V., Kaspi V. M., Livingstone M. A., Woods P. M., 2008, *Science*, **319**, 1802
- Geldzahler B. J., Pauls T., Salter C. J., 1980, *A&A*, **84**, 237
- Georgousi M., Karnesis N., Korol V., Pieroni M., Stergioulas N., 2023, *MNRAS*, **519**, 2552
- Gomez-Gomar J., Hernanz M., Jose J., Isern J., 1998, *MNRAS*, **296**, 913
- Good D., CHIME/FRB Collaboration 2020, The Astronomer's Telegram, **14074**, 1
- Göğüş E., et al., 2016, *ApJ*, **829**, L25
- H. E. S. S. Collaboration et al., 2014, *A&A*, **562**, L4
- H. E. S. S. Collaboration et al., 2018, *A&A*, **612**, A10
- H. E. S. S. Collaboration et al., 2022, *Science*, **376**, 77
- H. E. S. S. Collaboration Olivera-Nieto L., Reville B., Hinton J., Tsiros M., 2024, *Science*, **383**, 402
- Hachisu I., Kato M., 2022, *ApJ*, **939**, 1
- Hambleton K. M., et al., 2022, [arXiv e-prints](https://arxiv.org/abs/2208.04499), p. [arXiv:2208.04499](https://arxiv.org/abs/2208.04499)
- Hernanz M., Tatischeff V., 2012, *Baltic Astronomy*, **21**, 62
- Hillas A. M., 1984, *ARA&A*, **22**, 425
- Iben I. J., 1982, *ApJ*, **259**, 244
- IceCube Collaboration et al., 2018, *Science*, **361**, eaat1378
- Jourdain E., Roques J. P., Chauvin M., Clark D. J., 2012, *ApJ*, **761**, 27
- Kafexhiu E., Aharonian F., Taylor A. M., Vila G. S., 2014, *Phys. Rev. D*, **90**, 123014
- Kantzas D., et al., 2021, *MNRAS*, **500**, 2112
- Kantzas D., Markoff S., Lucchini M., Ceccobello C., Grinberg V., Connors R. M. T., Uttley P., 2022, *MNRAS*, **510**, 5187
- Kaspi V. M., Beloborodov A. M., 2017, *ARA&A*, **55**, 261
- Kemp A. J., Karakas A. I., Casey A. R., Izzard R. G., Ruitter A. J., Agrawal P., Broekgaarden F. S., Temmink K. D., 2021, *MNRAS*, **504**, 6117
- Kemp A. J., Karakas A. I., Casey A. R., Kobayashi C., Izzard R. G., 2022, *MNRAS*, **509**, 1175
- Kimura S. S., Murase K., Mészáros P., 2020, *ApJ*, **904**, 188

- Knödseder J., et al., 2016, *A&A*, **593**, A1
- Koljonen K. I. I., Hannikainen D. C., McCollough M. L., Pooley G. G., Trushkin S. A., 2010, *MNRAS*, **406**, 307
- Lamberts A., Blunt S., Littenberg T. B., Garrison-Kimmel S., Kupfer T., Sanderson R. E., 2019, *MNRAS*, **490**, 5888
- Laurent P., Rodríguez J., Wilms J., Cadolle Bel M., Pottschmidt K., Grinberg V., 2011, *Science*, **332**, 438
- Lhaaso Collaboration et al., 2021, *Science*, **373**, 425
- Li T. P., Ma Y. Q., 1983, *The Astrophysical Journal*, **272**, 317
- Li J., Rea N., Torres D. F., de Oña-Wilhelmi E., 2017, *ApJ*, **835**, 30
- Li J., Torres D. F., Liu R.-Y., Kerr M., de Oña Wilhelmi E., Su Y., 2020, *Nature Astronomy*, **4**, 1177
- Loh A., et al., 2016, *MNRAS*, **462**, L111
- López-Oramas A., et al., 2021, *PoS*, ICRC2021, 783
- Lyubarsky Y., 2014, *MNRAS*, **442**, L9
- MAGIC Collaboration et al., 2019, *Nature*, **575**, 455
- MAGIC Collaboration et al., 2020, *A&A*, **635**, A158
- Maier G., Gueta O., Zanin R., 2023, CTAO Instrument Response Functions: Comparison of prod5 and prod3b releases, doi:10.5281/zenodo.8050921, <https://doi.org/10.5281/zenodo.8050921>
- Malyshev D., Zdziarski A. A., Chernyakova M., 2013, *MNRAS*, **434**, 2380
- Margon B., 1984, *ARA&A*, **22**, 507
- Mariotti M., 2010, The Astronomer's Telegram, **2967**, 1
- Martin P., Dubus G., Jean P., Tatischeff V., Dosne C., 2018, *A&A*, **612**, A38
- Masetti N., et al., 2006, *A&A*, **459**, 21
- Mayer M., Buehler R., Hays E., Cheung C. C., Dutka M. S., Grove J. E., Kerr M., Ojha R., 2013, *ApJ*, **775**, L37
- Mazets E. P., et al., 2008, *ApJ*, **680**, L230
- Mereghetti S., 2008, *A&ARv*, **15**, 225
- Mereghetti S., Pons J. A., Melatos A., 2015, *Space Sci. Rev.*, **191**, 315
- Mereghetti S., et al., 2020, *ApJ*, **898**, L29
- Mestre E., de Oña Wilhelmi E., Zanin R., Torres D. F., Tibaldo L., 2020, *MNRAS*, **492**, 708
- Mestre E., de Oña Wilhelmi E., Khangulyan D., Zanin R., Acero F., Torres D. F., 2021, *MNRAS*, **501**, 337
- Metzger B. D., Caprioli D., Vurm I., Beloborodov A. M., Bartos I., Vlasov A., 2016, *MNRAS*, **457**, 1786
- Metzger B. D., Fang K., Margalit B., 2020, *ApJ*, **902**, L22
- Middleton M. J., et al., 2017, *New Astron. Rev.*, **79**, 26
- Miller-Jones J. C. A., Jonker P. G., Dhawan V., Briskin W., Rupen M. P., Nelemans G., Gallo E., 2009, *ApJ*, **706**, L230
- Miller-Jones J. C. A., et al., 2021, *Science*, **371**, 1046
- Mirabel I. F., Rodríguez L. F., 1998, *Nature*, **392**, 673
- Munari U., Giroletti M., Marcote B., O'Brien T. J., Veres P., Yang J., Williams D. R. A., Woudt P., 2022, *A&A*, **666**, L6
- Murase K., Kashiyama K., Mészáros P., 2016, *MNRAS*, **461**, 1498
- Observatory C. T. A., Consortium C. T. A., 2021, CTAO Instrument Response Functions - prod5 version v0.1, doi:10.5281/zenodo.5499840, <https://doi.org/10.5281/zenodo.5499840>
- Olmi B., 2023, *Universe*, **9**, 402
- Ong R. A., 2010, The Astronomer's Telegram, **2968**, 1
- Paczynski B., 1992, *Acta Astron.*, **42**, 145
- Page K. L., et al., 2022, *MNRAS*, **514**, 1557
- Papitto A., Torres D. F., 2015, *ApJ*, **807**, 33
- Papitto A., de Martino D., 2022, in Bhattacharyya S., Papitto A., Bhattacharya D., eds, *Astrophysics and Space Science Library* Vol. 465, *Astrophysics and Space Science Library*. pp 157–200 (arXiv:2010.09060), doi:10.1007/978-3-030-85198-9_6
- Papitto A., et al., 2013, The Astronomer's Telegram, **5069**, 1
- Paredes J. M., et al., 2013, *Astroparticle Physics*, **43**, 301
- Patruo A., et al., 2014a, *ApJ*, **781**, L3
- Patruo A., et al., 2014b, *ApJ*, **781**, L3
- Piano G., et al., 2012, *A&A*, **545**, A110
- Piano G., Munar-Adrover P., Verrecchia F., Tavani M., Trushkin S. A., 2017, *ApJ*, **839**, 84
- Rasul K., Chadwick P. M., Graham J. A., Brown A. M., 2019, *MNRAS*, **485**, 2970
- Reid M. J., Miller-Jones J. C. A., 2023, *ApJ*, **959**, 85
- Roberts O. J., et al., 2021, *Nature*, **589**, 207
- Romano P., et al., 2015, *A&A*, **576**, L4
- Romero G. E., Vieyro F. L., Chaty S., 2014, *A&A*, **562**, L7
- Roy J., et al., 2015, *ApJ*, **800**, L12
- Rudak B., Dyks J., 1998, *MNRAS*, **295**, 337
- Russell T. D., Soria R., Motch C., Pakull M. W., Torres M. A. P., Curran P. A., Jonker P. G., Miller-Jones J. C. A., 2014, *MNRAS*, **439**, 1381
- Sabatini S., et al., 2010, *ApJ*, **712**, L10
- Sabatini S., et al., 2013, *ApJ*, **766**, 83
- Schaefer B. E., 2023, *MNRAS*, **524**, 3146
- Schaefer B. E., Kloppenborg B., Waagen E. O., Observers T. A., 2023, The Astronomer's Telegram, **16107**, 1
- Sguera V., 2009, in Proc. of the 7th INTEGRAL Workshop September 8-11 2008 Copenhagen, Denmark (arXiv:0902.0245),
- Sguera V., 2013, *Nuclear Physics B Proceedings Supplements*, **239**, 76
- Sguera V., Romero G. E., Bazzano A., Masetti N., Bird A. J., Bassani L., 2009, *ApJ*, **697**, 1194
- Sidoli L., 2017, in XII Multifrequency Behaviour of High Energy Cosmic Sources Workshop (MULTIF2017). p. 52 (arXiv:1710.03943), doi:10.22323/1.306.0052
- Sidoli L., Paizis A., 2018, *MNRAS*, **481**, 2779
- Siegert T., et al., 2016, *Nature*, **531**, 341
- Stappers B. W., et al., 2013, The Astronomer's Telegram, **5513**, 1
- Striani E., et al., 2013, *ApJ*, **765**, 52
- Sun X.-N., Yang R.-Z., Liu B., Xi S.-Q., Wang X.-Y., 2019, *A&A*, **626**, A113
- Svinkin D., et al., 2021, *Nature*, **589**, 211
- Takata J., et al., 2014, *ApJ*, **785**, 131
- Tatischeff V., Hernanz M., 2007, *ApJ*, **663**, L101
- Tavani M., et al., 2009, *Nature*, **462**, 620
- Tavani M., et al., 2011, *Science*, **331**, 736
- Tavani M., et al., 2021, *Nature Astronomy*, **5**, 401
- Tavani M., F. Addis A., Argan A., 2024, The Astronomer's Telegram, **16450**
- Tetarenko B. E., Sivakoff G. R., Heinke C. O., Gladstone J. C., 2016, *ApJ Supplement Series*, **222**, 15
- Thorstensen J. R., Armstrong E., 2005, *AJ*, **130**, 759
- Tibolla O., 2023, in Journal of Physics Conference Series. p. 012017, doi:10.1088/1742-6596/2429/1/012017
- Torres D. F., Rea N., Esposito P., Li J., Chen Y., Zhang S., 2012, *ApJ*, **744**, 106
- Torres D. F., Ji L., Li J., Papitto A., Rea N., de Oña Wilhelmi E., Zhang S., 2017, *ApJ*, **836**, 68
- Trimble V., 1973, *PASP*, **85**, 579
- Walter R., 2007, *Ap&SS*, **309**, 5
- Weisskopf M. C., et al., 2013, *ApJ*, **765**, 56
- Weng S.-S., et al., 2022, *Nature Astronomy*, **6**, 698
- Xing Y., Wang Z., 2015, *The Astrophysical Journal*, **808**, 17
- Xing Y., Wang Z., Zhang X., Chen Y., Jithesh V., 2019, *ApJ*, **872**, 25
- Yaron O., Prialnik D., Shara M. M., Kovetz A., 2005, *ApJ*, **623**, 398
- Yusifov I., Küçük I., 2004, *A&A*, **422**, 545
- Zabalza V., 2015, in 34th International Cosmic Ray Conference (ICRC2015). p. 922 (arXiv:1509.03319), doi:10.22323/1.236.0922
- Zanin R., Fernández-Barral A., de Oña Wilhelmi E., Aharonian F., Blanch O., Bosch-Ramon V., Galindo D., 2016, *A&A*, **596**, A55
- Zdziarski A. A., Mikolajewska J., Belczynski K., 2013, *MNRAS*, **429**, L104
- Zdziarski A. A., Pjanka P., Sikora M., Stawarz L., 2014, *MNRAS*, **442**, 3243
- Zdziarski A. A., Malyshev D., Chernyakova M., Pooley G. G., 2017, *MNRAS*, **471**, 3657
- Zdziarski A. A., et al., 2018, *MNRAS*, **479**, 4399
- Zheng J.-H., Huang Y.-Y., Zhang Z.-L., Zhang H.-M., Liu R.-Y., Wang X.-Y., 2022, *Phys. Rev. D*, **106**, 103011
- Zhu W., Wang B., Zhou D., et al., 2020, The Astronomer's Telegram, **14084**, 1
- de Martino D., et al., 2010, *A&A*, **515**, A25
- de Oña Wilhelmi E., López-Coto R., Su Y., 2023, *MNRAS*, **523**, 105
- del Valle M. V., Romero G. E., 2014, *A&A*, **563**, A96
- del Valle M. V., Romero G. E., Luque-Escamilla P. L., Martí J., Ramón Sánchez-Sutil J., 2011, *ApJ*, **738**, 115
- van Scherpenberg J., Mirzoyan R., Vovk I., Peresano M., Zaric D., Temnikov

P., Godinović N., Besenrieder J., 2019, in 36th International Cosmic Ray Conference (ICRC2019). p. 812 ([arXiv:1909.04356](https://arxiv.org/abs/1909.04356))

This paper has been typeset from a $\text{\TeX}/\text{\LaTeX}$ file prepared by the author.